ABSTRACT

Title of dissertation: WAVELENGTH DEPENDENCE IN OPTICAL TWEEZERS

Brooke Hester, Doctor of Philosophy, 2010

Dissertation directed by: Wolfgang Losert
University of Maryland

Optical trapping forces are dependent upon the difference between the trap wavelength and the extinction (scattering plus absorption) resonances of a trapped particle. This leads to a wavelength-dependent trapping force, which should allow for the optimization of optical tweezers systems, simply by choosing the best trapping wavelength for a given experiment.

Although optical forces due to a near-resonant laser beam have been extensively studied for atoms, the situation for larger particles has not been explored experimentally. The ability to selectively trap certain particles with a given extinction peak may have many practical applications. Here, resonance-based trapping is investigated using nanoshells, particles with a dielectric core and metallic coating that exhibit tunable plasmon resonances, and with silica and polystyrene beads. A measure of the trap strength was realized for single particles trapped in three dimensions, and near-resonant trapping was investigated by measuring the trap strength as a function of trap wavelength. Since the resulting trapping is highly temperature-dependent, this necessitated temperature measurements of single optically trapped

particles.

To make these measurements a new optical tweezer apparatus was designed and constructed, the apparatus has wavelength tunability and was used to study these resonance effects. Optical trap stiffness, which is analogous to the spring constant of a stable trap, is measured for trapped particles that exhibit either single or multiple extinction resonances. The applications of this apparatus are not limited to force spectroscopy. Other measurement systems and techniques could be easily implemented into the custom-built apparatus, allowing for the measurement of various properties of single optically trapped particles as a function of wavelength.

WAVELENGTH DEPENDENCE IN OPTICAL TWEEZERS

by

Brooke Cranswick Hester

Dissertation submitted to the Faculty of the Graduate School of the
University of Maryland, College Park in partial fulfillment
of the requirements for the degree of
Doctor of Philosophy
2010

Advisory Committee:
Professor Wolfgang Losert, Chair
Dr. Kristian Helmerson
Dr. Gretchen Campbell
Professor Steven Rolston
Professor Chris Monroe

Acknowledgments

I owe a sea of gratitude to the many people who made this thesis possible.

First I would like to thank my advisor, Dr. Kris Helmerson, for the opportunity to be included as a member of the Optical Tweezers Laboratory and the Laser Cooling and Trapping Group at the National Institute of Standards and Technology. Because of him, I was I was able to work on many intriguing projects and learn more than I ever dreamed possible. There has never been a time when I have knocked on his door for help and was turned away. I very much appreciate his advice, support, and mentorship.

I would also like to thank the chair of my thesis committee, Professor Wolfgang Losert. He offered crucial guidance throughout the evolution of the project. I must acknowledge the seemingly infinite support from Dr. Gretchen Campbell as well. She was an ever-present mentor and was always willing to go the extra mile to help with even the smallest detail. Perhaps most importantly, when times were tough, she was there to listen and offer suggestions or sympathy. I am forever grateful. Thanks are also due to Professor Steve Rolston and Professor Chris Monroe for spending the time to serve on my thesis committee and review the dissertation manuscript.

My colleagues at the Optical Tweezers Laboratory no doubt helped to shape my graduate career and will always be the recipients of my undying gratitude. Rani Kishore possesses a mountain of knowledge that she is constantly willing to share and I will always appreciate her calming presence. Alice Crawford helped me start-off by assisting with the construction of the first iteration of my optical tweezer

apparatus. Ana Jofre is a great friend and will serve as a future collaborator if I am fortunate enough. Jianyong Tang inspired me with his fascination for learning and understanding science and was ever-curious to ponder any unanswered question. Carlos Lopez Mariscal would stop his important work to help, even when he absolutely should not have, and facilitated my increased understanding of optics and instrumentation. He also introduced me to the importance of networking and career service, for which I am forever grateful.

I would also like to acknowledge help and support from members of the Laser Cooling and Trapping Group. Gail Griffin-Ferris and Kim Emswiler both went overboard to help me with anything and because of them I have retained my sanity. Dr. Bill Phillips and Dr. Trey Porto both flattered me with their interest in this research project and offered helpful advice and suggestions and for those I am truly thankful. Anand Ramanathan was a great office-mate and was always available for lively and interesting discussion. Kevin Wright offered much needed assistance with optics software and was always willing to lend a helping hand.

I owe my deepest thanks to my family. My husband endured the many difficult years that a Ph.D. program entails and supported me in very tough times. Words cannot express my love and gratitude for him. I thank my parents who have always stood by me and guided me through life. I would also like to thank Catherine and Brooks Hooper who are like family to me, and who kept me well nourished and in the best of spirits. Lastly, I thank my daughter, Josephine, for being the inspiration for the completion of this thesis.

Table of Contents

List of Tables

List of Figures

List of Abbreviations

BFP	Back focal plane
PSD	Position sensing diode
KK	Kramers-Kronig
NA	Numerical aperture
CEO	Classical electron oscillator
SPP	Surface plasmon polariton
WGM	Whispering gallery mode
SEM	Scanning electron microscope
CW	Continuous Wave
YAG	Nd:YAG
PBS	Polarizing beamsplitter
LD	Laser diode
W	Waveplate
L	Lens
D	Dichroic mirror
OL	Objective lens
PD	Photodiode
CL	Condensor lens
CCD	Charge coupled device
C	Camera
BS	Beam sampler
FL	Focusing lens
MO	Microscope objective
GNP	Gold nanoparticle
FWHM	Full width half maximum

Chapter 1

Introduction

1.1 What are Optical Tweezers?

Optical tweezers, also known as a single-beam gradient force trap, is a well-known scientific tool used to confine small objects with highly-focused, coherent light. The trapping of such objects is made possible by an attractive "gradient" force that arises from the extreme gradient of light intensity at the laser beam focus. A repulsive "scattering" force in the direction of light propagation is also present, due to radiation pressure on the particle, and tends to push a particle out of the optical trap. For stable optical trapping to occur, the gradient force must exceed the scattering force.

The first report of observations of these optical forces on microscopic objects was by Bell Labs scientist Arthur Ashkin in 1970 [1]. This preliminary study evolved into what we know today as optical tweezers; Ashkin and his colleagues were also the first to demonstrate the use of a laser for the three-dimensional trapping of dielectric particles [2].

Optical tweezers have been shown to be a flexible and useful tool for the manipulation of small objects from the nanometer to the micrometer scale [2, 3, 4], and have been used to study biological systems including those at the single molecule level [5], properties of fluids [6], systems of colloids [7], and are also used as tools

for many manipulation techniques [8].

1.2 Motivations

While many experiments have examined the physics of the trapping forces in optical tweezers systems, the effects of the trapping wavelength and optical properties of the trapped particle have not been analyzed previously with a focus on optical forces.

Although optical forces due to a near-resonant laser beam have been studied extensively for atoms, the situation for larger particles has only been studied numerically [9] and, until recently, remained experimentally unverified. A particle that is much smaller than the wavelength of the light incident upon it, which is known as the "Rayleigh size regime," is expected to behave much like an atom in an optical trap. The small size of the particle compared to the large uniform electric field results in a dipole response. In such a case, the optical forces are dominated by the complex polarizability of the particle, which is inherently linked to the extinction (scattering plus absorption) resonance of the particle. The total trapping force is a sum of the gradient and scattering forces. The gradient force, which is mostly responsible for trapping, should increase as the trapping wavelength approaches the resonance from the longer wavelengths, should come to a maximum close to the resonance wavelength, and should drop sharply at the extinction resonance [10]. An example resonance is shown in Figure 1.1.

For larger particles whose size is on the order of the wavelength, predictions

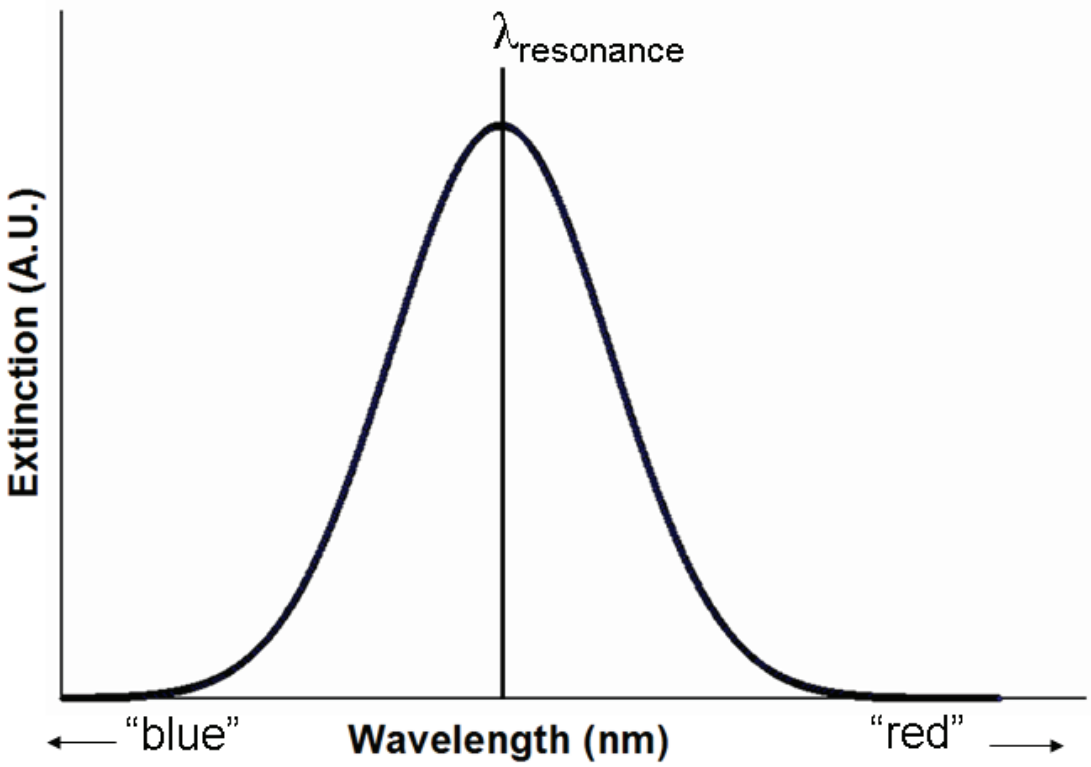

Figure 1.1: Example extinction resonance for a Rayleigh particle. The resonance peak is labeled $\lambda_{resonance}$. "Red" wavelengths are higher than the resonance wavelength and "blue" wavelengths are lower than the resonance wavelengths.

require rigorous numerical calculations (based on solving Maxwell's equations for specific conditions) and cannot be viewed with such a simple picture, yet the forces are still resonance-dependent. For some trapping schemes with dielectric particles, wavelength dependence has been calculated, and maximal trapping forces are predicted to exist when the ratio of particle radius to trap wavelength is in the range of one half to three-quarters [11]. Particles whose diameter are much larger than the trap wavelength are not expected to exhibit resonant behavior when considering optical forces, because the trap size is very small compared to any large sphere [12]. Hence, enhanced optical forces due to a resonance are only expected for Rayleigh particles and for particles whose size is comparable to the trap wavelength.

Previously, optical forces and their dependence on optical resonances have been studied experimentally in an optical levitation scheme over short laser wavelength ranges [13] and for dye-loaded dielectric particles [14]. In the first case, since the particles are not actually optically trapped, only the scattering force and not the gradient force is considered. In the second case, the trap strength measurements are normalized for beads lacking dye, meaning that only the absorption resonance, and not the total extinction resonance is considered. We believe that a consideration of the total extinction resonance of a trapped particle over an optimized trapping wavelength range should give rise to a significant increase in the trapping force.

Studies have also explored the trapping of metallic Rayleigh particles at a single wavelength and have shown that metal particles can trap up to seven times stronger than dielectric beads of the same size, due to their plasmon resonance [4]. In the case of the investigation of the effects of optical trapping and extinc-

tion resonance for Rayleigh particles, a definitive experimental conclusion has not been reached, but theories exist predicting enhanced trapping in the vicinity of the extinction resonance [10].

In order to study wavelength-dependent effects in optical trapping, a new experimental apparatus was designed and constructed. In addition to resonance effects, a number of other experiments are also possible with this apparatus. It is expected that the trap laser wavelength dependence should play a strong role in optimizing the optical forces of a tweezer system [10]. Therefore, our apparatus - optical tweezers with wavelength tunability - can be used for determining the optimal trapping wavelengths for a number of applications such as optical sorting and binding, low-optical-power tweezing and prevention of thermal damage to delicate biological systems, the selective exertion of strong forces on small objects in a crowded environment, as well as for improvements to cost-efficient optical tweezers experiments. It is true that experimentalists are typically able to trap a particle regardless of its resonance, but they generally lack the ability to experimentally determine an optimal trapping wavelength. This would be important for applications where minimal heating and/or maximal forces are desired. Properties of micron-scale objects, such as the complex refractive index, can also be measured as a function of wavelength. Furthermore, the instrument is useful for wavelength-dependent measurements of single nanoparticles. The bulk properties of a material can differ greatly from those on the nano-scale. The apparatus will provide a means for the measurement of those smaller-scale properties for single particles surrounded by a uniform fluid, preventing the need for a motion-locking substrate.

1.3 Outline of Thesis

In Chapter 2, I present the basic physics of how optical tweezers function and show how they are used to measure miniscule forces. Two basic regimes of particles that can be trapped by optical tweezers are Rayleigh particles, those much smaller than the light wavelength, and Mie particles, whose size is on the order of or is much larger than the light wavelength. Predictions of optical forces are separated into these two particle regimes, and are explained in detail in this chapter.

Chapter 3 is focused on the types of objects optically trapped for this thesis. Gold nanoshells, the Rayleigh particles utilized for this study, are thoroughly discussed, including the theory behind their design and fabrication details. Polystyrene and silica beads, the Mie particles investigated here, are also introduced. Explanations of the resonance profiles for both particle types are included.

The main theme of Chapter 4 is the experimental apparatus designed, constructed, and utilized for studying resonance effects in optical trapping. The first iteration of this apparatus failed to successfully produce accurate measurements, so both are presented with details. The second apparatus is discussed in most detail.

In Chapter 5, the techniques required for accurate measurements are listed in detail. Multiple overlapping beams used for optical trapping require a special alignment technique, described in this chapter. It is crucial to know the optical power of the trapping beam, and keep it constant throughout measurements. A calibration of displacement at the trap location must be performed, and distances of the devices controlling motion there must also be known. This is discussed in detail.

With a change in wavelength comes inherent changes in several other properties. Methods, explained here, were developed in order to prevent the changes in these properties from affecting the outcome of the experiment. Finally, an explanation of the scheme used to ensure the optical trapping of single particles is presented.

In Chapter 6, calculations and measurements of temperature and viscosity of the fluid at the particle-water interface are presented. This is begun with an explanation of how an incorrect assumption of constant temperature and viscosity can affect the outcome of an optical tweezers measurement. Next, former studies of temperature and viscosity measurements are briefly explained. Calculations of metallic particles are the subsequent focus, followed by the experimental results of temperature measurements of gold nanoshells and dielectric particles.

In Chapter 7, the results of the studies of resonance effects in optical tweezers are presented for each particle regime: for Rayleigh particles, for Mie particles whose size is on the order of the trapping wavelength, and for Mie particles whose size is orders of magnitude larger than the trapping wavelength.

In Chapter 8, results from experiments trapping multiple nanoshells are presented. First, changes in experimental signals with respect to the number of nanoshells in the optical trap are explained. Next, the outcome of temperature measurements for multiply trapped nanoshells are shown. Lastly, a brief discussion of optical binding is included.

In Chapter 9, conclusions to the thesis are provided. Heating of trapped particles is reviewed, followed by a discussion of the results of resonance effects in optical tweezers.

In Chapter 10, suggestions for future experiments are mentioned.

Chapter 2

Physics of Optical Tweezers

2.1 Optical Trapping Basics

Optical tweezers can trap dielectric particles when their index of refraction is higher than that of the surrounding medium. In simple terms, Snell's law dictates that a light ray will bend as it enters the particle, causing a change in momentum, which gives rise to a force. For a highly focused laser beam, the total force for many light rays acting in unison will serve to hold the particle in place at an equilibrium position near the beam focus.

To be more general, one can say that the reflection, refraction, or absorption of light by an object gives rise to a momentum transfer from the light to the object. If considering the photon description of light, each light particle propagates according to the geometrical optics picture, and transfers linear momentum to the object by means of collisions of the photons with the atoms [12].

For a truly accurate description of the system, this simplified picture is not quite right. A paraxial approximation to the light beam must be applied with high order corrections in order to correctly depict beam focusing. Additionally, properties of the trapped particle must also be considered, including size, material, and complex index of refraction, among others. An in-depth discussion of the forces responsible for optical trapping, which includes these factors, is given later in this

chapter in Section 2.3.

A fundamental principle shared by the optical tweezers community is that this system may be considered a highly overdamped simple harmonic oscillator. A harmonic potential well is created by the interaction of the particle with the focused light beam. Optical tweezers typically trap single micro- or nanoparticles in fluid[1], and so the Einstein-Ornstein-Uhlenbeck theory [16] of Brownian motion describes the motion of the particle in the harmonic trapping potential. A Langevin equation, which describes a set of equations of motion containing a random force, is used for the equation of motion of an optical tweezers system (Equation 2.1), shown here in one dimension.

$$m\ddot{x}(t) + \gamma_0\dot{x}(t) + \kappa x(t) = \eta(t)\sqrt{2k_bT\gamma_0} \tag{2.1}$$

Here, $x(t)$ is the displacement of the particle from its equilibrium position, m is the mass of the particle, κ is the spring constant or trap stiffness, k_b is Boltzmann's constant, and T is absolute temperature, where $\eta(t)$ is a random process in time associated with the force due to thermal fluctuations, $\langle\eta(t)\rangle = 0$, and $\langle\eta(t)\eta(t')\rangle = \delta(t-t')$ for all t and t' [17]. The drag coefficient, γ_0, is found using Stokes' law, which describes the frictional force exerted on a spherical object with very small Reynolds number in a continuous viscous fluid, and leads to the definition of Stokes' drag coefficient:

$$\gamma_0 = 6\pi\rho\nu R. \tag{2.2}$$

[1]Researchers, with great difficulty, have succeeded in levitating and trapping particles in air with a laser trap[3, 15].

R is the radius of the sphere, $\mu = \rho\nu$ is the shear viscosity of the fluid, ρ is the fluid density, and ν is the kinematic viscosity of the fluid.

The first term of Equation 2.1 represents the inertial force component for a particle with mass m, the second term represents the viscous damping force, and the third term represents the harmonic force from the optical potential. The right hand side is a random Gaussian process representing Brownian forces. Under normal conditions, where water or a buffer is used as the fluid surrounding a dielectric particle, viscous forces dominate inertial forces, and it is said that the system is in the low Reynolds number regime. Reynolds number, Re, (Equation 2.3) is defined as the ratio of the inertial force density, $f_i \sim \rho v^2/L_0$ to the viscous force density $f_v \sim \mu v/L_0^2$

$$Re \equiv \frac{f_i}{f_v} = \frac{\rho v L_0}{\mu} \tag{2.3}$$

where v is the fluid velocity and L_0 is the characteristic length scale for the system in question. For optical tweezers, typical velocities range from 1 μm/s to 1 cm/s and microscope chamber sizes are in the range of 100 μm, giving a Reynolds number ranging from $\mathscr{O}(6)$ to $\mathscr{O}(10)$ [18]. Because Re is so small, viscous forces overwhelm inertial forces and the dynamics of a particle in water solution can be described as that of an overdamped harmonic oscillator system, allowing us to drop the inertial term in Equation 2.1. This leaves the following equation (2.4) for an optical tweezer system.

$$\dot{x}(t) + 2\pi f_c x(t) = \eta(t)\sqrt{\frac{2k_bT}{\gamma_0}} \tag{2.4}$$

Here the corner frequency $f_c \equiv \kappa/2\pi\gamma_0$ is introduced, which will be explained in

detail later in this work. For substantially small $x(t)$, the particle will experience a restoring force that is proportional to $x(t)$. Hence, the trapped object is said to obey Hooke's law and behaves as a microscopic spring. Incidentally, these small displacements from the equilibrium position are typically orders of magnitude smaller than the light wavelength, allowing the trapped object to be utilized as a measurement tool for tiny displacements and forces exhibited by biological systems or molecules. Typically the trap stiffness κ, analogous to the spring constant of the system, is measured in optical tweezers experiments.

2.2 Optical Tweezers and Force Spectroscopy

Consider the Fourier transform of Equation 2.4 for some $x(t)$, where $x(t)$ is a measurement of the position of the trapped particle in one dimension as a function of time, collected for time t_{meas}. With $f_k \equiv k/t_{meas}$, $k \in$ integers:

$$\tilde{x_k} = \int_{-t_{meas}/2}^{t_{meas}/2} dt e^{2i\pi f_k t} x(t) = \frac{\tilde{\eta_k}\sqrt{2k_B T/\gamma_0}}{2\pi(f_c - if_k)} \tag{2.5}$$

From the definition of $\eta(t)$, the following is true: $\langle\tilde{\eta_k}\rangle = 0$, $\langle\tilde{\eta_k}^*\tilde{\eta_l}\rangle = T_{meas}\delta_{k,l}$, and $\langle|\tilde{\eta_k}|^4\rangle = 2t_{meas}^2$. Because $\eta(t)$ has the properties of an uncorrelated Gaussian, $(|\tilde{\eta_k}|^2)_{k=0,1,...}$ are similarly uncorrelated positive random variables with an exponential distribution [17]. The power spectrum of a signal $x(t)$ as shown in Figure 2.1. describes the frequency distribution of the power of a time series. Also known as the power spectral density, it is a positive real function of the variation of frequencies in a stochastic process, with units of V^2/Hz [19]. It is defined as the modulus

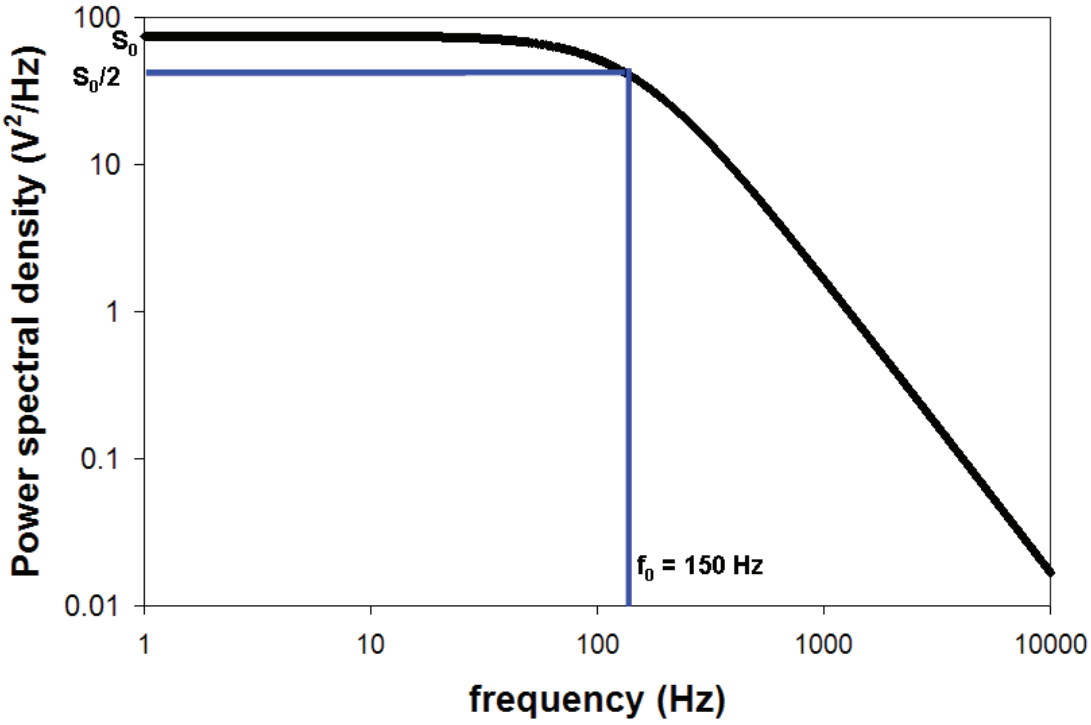

Figure 2.1: Example Lorentzian-shaped power spectrum. The corner frequency is defined as the frequency at which the amplitude falls to half its maximum. Here the corner frequency is 150 Hz.

squared of the Fourier transform of the time signal, divided by the total time of measurement. In the case of optical tweezers, the experimental power spectrum is:

$$P_k^{(exp)} \equiv |\tilde{x}_k|^2/t_{meas} = \frac{k_B T|\tilde{\eta}_k|^2}{2\pi^2\gamma_0(f_c^2 + f_k^2)t_{meas}} \tag{2.6}$$

The expected value in time is Lorentzian in shape (Equation 2.7).

$$P_k \equiv \langle P_k^{(exp)} \rangle = \frac{k_B T}{2\pi^2\gamma_0(f_c^2 + f_k^2)} \tag{2.7}$$

This gives the optical trapping experimentalist a simple means for a determination of the corner frequency, and therefore the stiffness, of an optically trapped particle. A signal of the position of the trapped particle as a function of time is recorded and Fourier transformed, and a Lorentzian function is fit to the power spectrum via a least-squares fitting method. Of course, experimentally, the time series is an array of values sampled at a regular rate, and so a discrete Fourier transform must be carried out to replace the continuous one in Equation 2.5. The discrete Fourier transform is a good approximation to the continuous Fourier transform for frequencies $|f_k| \ll f_{sample}$, and the resulting power spectra obey the same statistics. The fit is achieved by minimizing the parameter χ^2.

$$\chi^2 = \sum_k \left(\frac{P_k^{(exp)} - P_k}{P_k/\sqrt{n_b}} \right)^2 = n_b n_w \sum_k \left(\frac{P_k^{(exp)}}{P_k} - 1 \right)^2 \tag{2.8}$$

The parameters n_b and n_w are numbers of consecutive data points that are averaged in a block or window, respectively, so that one data point replaces several for data compression. What is called a "window of points" compresses in an equidistant manner on the frequency axis, while a block of points compresses in a logarithmic manner. Once fitting is achieved, the corner frequency (the frequency at which the maximum spectral amplitude is halved) of the Lorentzian is determined. The trap stiffness may then be calculated using

$$f_c = \kappa/2\pi\gamma_0 \tag{2.9}$$

where f_c was introduced in Equation 2.4. This is known as the power spectrum method or the corner frequency method. It requires an accurate knowledge of the Stokes' drag γ_0 (Equation 2.2), which is dependent on fluid viscosity and particle size, and is easily described for distances far from the coverslip surface. A discussion of fluid viscosity is included in Chapter 6 of this work.

Another method of determining trap stiffness utilizes the equipartition theorem. For a particle in a harmonic potential with spring constant or trap stiffness κ, the theorem is stated as follows:

$$\frac{1}{2}k_B T = \frac{1}{2}\kappa\langle x^2\rangle, \tag{2.10}$$

where x is the displacement of the trapped particle from the equilibrium position. In addition to the power spectrum method, this method provides another means of finding the trap stiffness by recording the position of the trapped particle. If the absolute temperature is known, the stiffness can be found by a determination of the variance of the position of the object. While the power spectrum method requires knowledge of the local viscosity and particle size, besides an assumption of temperature, the equipartition method only requires position information. However, a calibrated detector, for which distance versus volts is known, is a requirement for the equipartition method but not the power spectrum method. Position detection calibration is explained in detail in Chapter 5.

Both the power spectrum method and the equipartition method require position detection. The back focal plane (BFP) detection technique allows for three-

dimensional tracking of the displacement of the particle from the optical axis. It relies on the signal interference between unscattered light and forward scattered light from the trapped particle. This interference is detected with a position-sensing photodiode placed at an optical plane conjugate to the back-focal plane of the signal-collecting lens. When the intensity of the interference signal occurring at the back focal plane is imaged onto a position sensing detector (PSD), its voltage outputs, $V_x(t)$, $V_y(t)$, $V_{sum}(t)$, are proportional to the displacement of the particle from the optical axis. $V_{sum}(t)$ is the total intensity signal and is used for normalizing the lateral position voltages. The other two outputs are proportional to the lateral (x and y) particle displacements from the beam waist, and these voltages are directly proportional to distances via the voltage/distance detector calibration factor. By collecting these three signals in time for a trapped particle, one can determine the trap stiffness with either the power spectrum method or the equipartition method. Details of the position detection scheme utilized in this work are included in Chapters 4 and 5.

2.3 Optical Forces in Optical Trapping

Newton's second law states that the net force on a particle is equal to the rate of change of its momentum in time. Light carries momentum, and so the origin of optical forces lies in the exchange of momentum between photons and objects. Light will interact with an object via scattering (reflection and refraction) or absorption. Consequently, the direction and magnitude of the propagating light ray will change

and so will the photon momentum flux. One lone photon will not exert much force on an micrometer-sized object, but many photons, such as those which come from a laser beam, can wield a significant amount of force in that size regime.

If the particle in question is a micrometer-sized object with a refractive index that is higher than the surrounding medium, and it is irradiated with a focused Gaussian-profile laser beam, two main behaviors will occur. First, due to the radiation pressure of the photons incident on the particle, it will experience a force in the direction of light propagation. Second, the particle will undergo a force pushing it toward the center of the beam, or the area of highest light intensity, due to light refraction and redistribution of momentum in the particle.

In a very general sense, the total optical trapping force is defined as:

$$F_{OT} = \frac{n_m P Q}{c}, \tag{2.11}$$

where n_m is the index of refraction of the surrounding medium, c is the speed of light, P is the optical power, and Q is the trapping efficiency which depends on characteristics of the particle and the trapping beam.

The two components of the total force associated with optical trapping are the dissipative scattering force in the direction of light propagation and the conservative gradient force of a focused beam in the direction of the gradient of light intensity. For stable trapping, the gradient force must exceed the scattering force by enough to create a potential well deeper than the thermal energy of the particle. The understanding of these forces is separated into three main regimes: one for particles

much smaller than the light wavelength, one for particles whose size is on the order of light wavelength, and one for particles much larger than light wavelength.

2.3.1 Rayleigh particles

When the particle is much smaller than the radiation wavelength, it is known as a Rayleigh particle. Many definitions exist for describing exactly the size regime of a Rayleigh particle, but the most accepted is a particle whose radius a satisfies $a \leq \lambda/20$, where λ is the wavelength of the light incident on the particle. Another view is the the "Rayleigh condition", $ka << 1$, where k is the wavenumber and a is the particle radius. While these are widely accepted definitions, larger particles will frequently exhibit Rayleigh-like behavior [20].

For a neutral Rayleigh particle, the instantaneous field can be approximated as uniform and the particle is treated as an induced dipole oscillating in a time varying field, which is the same as for an atomic dipole. The induced dipole will follow $\vec{p} = \varepsilon_0 \alpha \vec{E}$ where $\vec{p}$ is the dipole moment, ε_0 is the vacuum electric permittivity, and $\vec{E}$ is the applied electric field [21]. The complex polarizability, $\alpha = \alpha' + i\alpha''$, arises from the lag between the phase of the applied electric field and the induced dipole. Because the particle is small compared to the wavelength, it is approximated as a perfect dipole that feels a Lorentz force due to field gradients. Continuous-wave lasers are normally used for optical trapping experiments and are used in this

experiment, such that $\frac{\partial}{\partial t}(\vec{E} \times \vec{B}) = 0$. In this case, the time-averaged forces are

$$\langle F_g \rangle = \frac{\varepsilon_0}{2} Re\left(\hat{x_j}\alpha' E_k^* \frac{\partial E_k}{\partial x_j}\right) \tag{2.12}$$

$$\langle F_s \rangle = \frac{\varepsilon_0}{2} Im\left(\hat{x_j}\alpha'' E_k^* \frac{\partial E_k}{\partial x_j}\right) \tag{2.13}$$

where $\hat{x_j}$ are the Cartesian unit vectors, E_k are the components of the electric field magnitude, F_g is the gradient force, and F_s is the scattering force [22, 23]. To predict these forces, the polarizability and electric field must be known. The spatial variation of the electric field can be described as a paraxial (zeroth-order) Gaussian beam focused by a lens. This field is described in equation 2.14: [24]

$$\vec{E} = \vec{E}_0 \sqrt{\frac{2}{\pi}} \frac{\sigma_0}{\sigma(z)} e^{\left(\frac{-r^2}{\sigma^2(z)}\right)} e^{\left(\frac{ik_m r^2}{2R(z)}\right)} e^{(ik_m z + i\eta(z))}, \tag{2.14}$$

with

$$\sigma^2(z) = \sigma_0^2 \left[1 + \left(\frac{z}{z_0}\right)^2\right], \tag{2.15}$$

$$R(z) = z \left[1 + \left(\frac{z_0}{z}\right)^2\right], \tag{2.16}$$

$$\eta(z) = tan^{-1}\left(\frac{z_0}{z}\right), \tag{2.17}$$

$z_0 = \pi\sigma_0^2/\lambda_m$, $k_m = 2\pi/\lambda_m$, where σ_0 is the beam waist radius, and λ_m is the wavelength of light in a medium with refractive index n_m. The scattering and

gradient forces that result for this electric field are

$$\hat{z} \cdot \langle \vec{F}_g \rangle = -\frac{\varepsilon_0}{\pi} \alpha' |E_0|^2 z \frac{\sigma_0^4}{z_0^2} \left[\frac{1}{\sigma^4(z)} - \frac{2r^2}{\sigma^6(z)} \right] e^{\left(\frac{-2r^2}{\sigma^2(z)} \right)} \tag{2.18}$$

and

$$\hat{r} \cdot \langle \vec{F}_g \rangle = -\frac{2\varepsilon_0}{\pi} \alpha' |E_0|^2 r \frac{\sigma_0^2}{\sigma^4(z)} e^{\left(\frac{-2r^2}{\sigma^2(z)} \right)} \tag{2.19}$$

for the gradient force and

$$\hat{z} \cdot \langle \vec{F}_s \rangle = \frac{\varepsilon_0}{\pi} \alpha'' |E_0|^2 \frac{\sigma_0^2}{\sigma^2(z)} \left[k_m \left(1 - \frac{r^2}{2} \frac{(z^2 - z_0^2)}{(z^2 + z_0^2)^2} \right) - \frac{\sigma_0^2}{z_0 \sigma^2(z)} \right] e^{\left(\frac{-2r^2}{\sigma^2(z)} \right)} \tag{2.20}$$

and

$$\hat{r} \cdot \langle \vec{F}_s \rangle = \frac{\varepsilon_0}{\pi} \alpha'' |E_0|^2 \frac{\sigma_0^2}{\sigma^2(z)} \frac{k_m r}{R(z)} e^{\left(\frac{-2r^2}{\sigma^2(z)} \right)} \tag{2.21}$$

for the scattering force. From Equations 2.18 to 2.21, it is clear that the gradient and scattering forces scale with the real (α') and imaginary (α'') parts of the complex electric polarizability, respectively. So the extrema of the real and imaginary parts of the electric polarizability will also correspond to the extrema of the gradient and scattering forces, respectively.

The complex electric polarizability for an oscillating dipole with a single resonance frequency can be determined using the classical electron oscillator (CEO) model [25]. In this model, a dipole with resonance frequency ω_0 is induced by an AC electric field at frequency ω. The equation of motion for the dipole with mass m and dipole moment $\vec{p} = q\vec{x}$ is found using the Lorentz force law and dipole

approximation, along with $\vec{B}_0 = \frac{c}{i\omega}\vec{\nabla} \times \vec{E}_0$, and is

$$\frac{\partial^2 \vec{x}}{\partial t^2} + 2\gamma \frac{\partial x}{\partial t} + \omega_0^2 \vec{x} = \frac{q\vec{E}}{m}. \tag{2.22}$$

This is true assuming a harmonic restoring force and a damping force that takes into account the radiation of power. The damping rate, γ, includes damping due to radiative decay, nonradiative decay, and decay due to dephasing collisions. This, with $\vec{p} = \varepsilon_0 \alpha \vec{E}$, gives the polarizability [10]

$$\alpha(\omega) = \alpha' + i\alpha'' = \frac{q^2}{m\varepsilon_0} \frac{\omega_0^2 - \omega^2 + 2i\gamma\omega}{\left(\omega_0^2 - \omega^2\right)^2 + 4\gamma^2\omega^2}. \tag{2.23}$$

For weak damping $\omega_0 \gg \gamma$, Equation 2.23 becomes

$$\alpha(\omega) = \alpha' + i\alpha'' = \frac{q^2}{2m\varepsilon_0\omega_0\gamma} \left[\frac{(\omega_0 - \omega)\gamma}{(\omega_0 - \omega)^2 + \gamma^2} + i \frac{\gamma^2}{(\omega_0 - \omega)^2 + \gamma^2} \right]. \tag{2.24}$$

Equation 2.24 is plotted in Figure 2.2.

The curves in Figure 2.2 may be used to predict maxima and minima locations of the optical forces for a classical electron oscillator. The scattering force, proportional to α'', is maximized at the resonance frequency. The gradient force, proportional to α', is maximized at a frequency red-shifted from resonance. The origin of the resonance is discussed in Chapter 3.

An atom in an electromagnetic field is modeled with this system. For an atom interacting with focused light, the gradient or reactive force is associated with the redistribution of energy from a cyclical and coherent transfer from the atom to

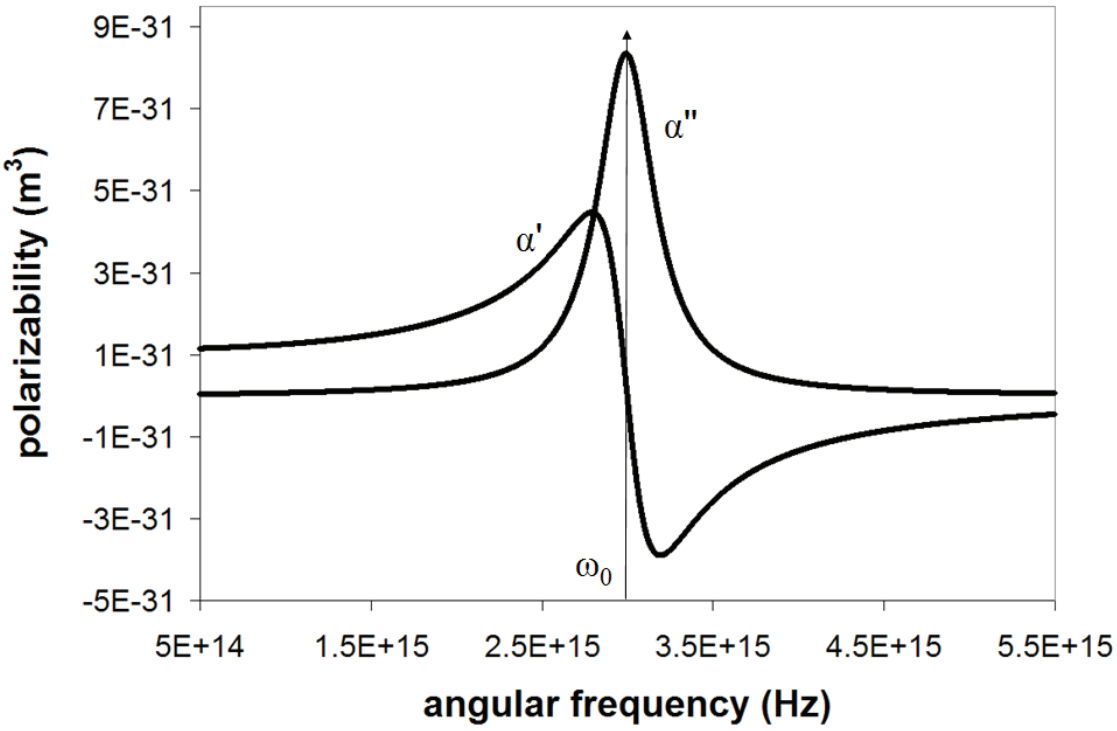

Figure 2.2: The real and imaginary parts of the electric polarizability, α' and α'' respectively, are plotted for a classical electron oscillator with resonance frequency $\omega_0 = 3$ x 10^{15} rad/sec and damping rate constant $\gamma = 0.2$ x 10^{15} rad/sec, using Equation 2.24.

the field and back, while the dissipative force is associated with radiation pressure. For a laser trapping frequency that is less than the dipole resonance frequency $\omega_{trap} < \omega_{resonance}$ (red detuning) the gradient force attracts the atom towards the region of highest intensity. This arises from the direction of the force on the red side of the resonance frequency. When $\omega_{trap} < \omega_{resonance}$, the force is positive since α' is positive. For $\omega_{trap} > \omega_{resonance}$ (blue detuning) the gradient force repels the atom away from the high intensity region due to the negative sign of α' [26].

Groups of oscillators are expected to behave similarly. Like a single oscillator, a group with a homogeneously broadened resonance will also have a Lorentzian lineshape for α''. If the oscillators in the group differ in their resonance frequencies, then inhomogeneous broadening will be present in the curve for α'', which may then be Gaussian. In either case, the collection will have a single resonance peak and the system will behave similarly to that of a single oscillator. That is true provided that the response is linear in power (as it should be for relatively low intensities). Then the real and imaginary parts of the polarizability of the system of oscillators are linked through the KK relations to those of a single oscillator [21].

The simplest system of oscillators is a dilute cloud of neutral atoms which do not interact. The new polarizability of the system is Equation 2.24 multiplied by NV, where N is the number density of oscillators, and V is the volume. The electric field interacts with the system to create a polarization density, altering $\vec{p} = \varepsilon_0 \alpha \vec{E}$ to

$$\vec{P} = N(\vec{p}) = \varepsilon_0 \chi \vec{E}, \tag{2.25}$$

where $\chi = (\chi_p - \chi_m)/(1+\chi_m)$ is the relative susceptibility of the sample with respect to the medium, χ_p is the susceptibility of the particle, and χ_m is the susceptibility of the medium. χ can then be thought of as the macroscopic polarizability, and it is related to α by

$$\chi = N\alpha. \tag{2.26}$$

For more complicated and realistic systems like amorphous solids, the relation is not achieved by a simple proportionality. Instead, the Clausius-Mossotti equation is employed.

$$\alpha = \frac{3}{N}\left(\frac{\varepsilon_p/\varepsilon_m - 1}{\varepsilon_p/\varepsilon_m + 2}\right), \tag{2.27}$$

where $\varepsilon_{p,m} = 1 + \chi_{p,m}$ are the complex dielectric constants of the particle and the medium, respectively [25]. The complex indices of refraction for the particle and the medium are obtained from the complex dielectric constants $n_{p,m} = \sqrt{\varepsilon_{p,m}}$ and for each, the real and imaginary parts are connected through the Kramers-Kronig (KK) relations [27]. With a Beer's law dependence of intensity loss on axis, $I(z) = I_0 e^{-2k''z} = I_0 e^{-az}$, and knowing $k = k' + ik'' = n\omega/c$, the imaginary part n'' of the complex index of refraction $n = n' + in''$ is related to the absorption coefficient a by $a = 2n''\omega/c = 4\pi n''/\lambda$ [28]. The absorption coefficient is a measurable quantity, and so for these kinds of systems if the absorption spectrum is known, then the scattering and gradient forces can be calculated and compared. Such a calculation was carried out by Agayan *et al* [10] for a dielectric Rayleigh particle composed of pink ruby with a single absorption spectrum peak. The imaginary part of the polarizability of the particle is modeled as a CEO, with both a Lorentzian and

Gaussian curve, and the real part of the polarizability for each is obtained using the KK relations. The scattering and gradient forces are calculated for several numerical aperture (NA) lenses across a very wide wavelength spectrum and the trap stiffness is found by

$$\kappa_j = -\left[\frac{\partial}{\partial x_j}\left(\hat{x}_j \cdot \langle \vec{F}_g + \vec{F}_s \rangle\right)\right] \tag{2.28}$$

evaluated at a minimum. The trap strength should increase with increasing laser frequency since the trapping potential scales with wavelength [10], as for the Gaussian intensity profile used here, $\kappa \propto 1/\lambda^2$, so trap stiffness is plotted as $\kappa\lambda^2$ as shown in Figure 2.3.

Note that for all convergence angles the trap stiffness increases as the trapping wavelength approaches from the red side of the resonance wavelength of the particle, then comes to a maximum somewhere near the resonance wavelength, and afterwards falls dramatically. The steep drop is due to the properties of the optical forces - the scattering force approached a maximum while the gradient force goes to zero at the resonance wavelength, so no trapping should occur in this wavelength region. Also note that the trap stiffness increases with numerical aperture, as expected since the gradient increases as the convergence angle increases. With these calculations, the axial trap stiffness is increased by a factor of up to 53 (Figure 2.3(a), $\theta = 50°$) and the radial trap stiffness is increased by a factor of up to 56 (Figure 2.3(b), $\theta = 50°$) when comparing trapping near resonance and trapping far from it. In a true system, higher numerical apertures are typically used for optical trapping, and so the stiffness and perhaps the factor increase are both larger.

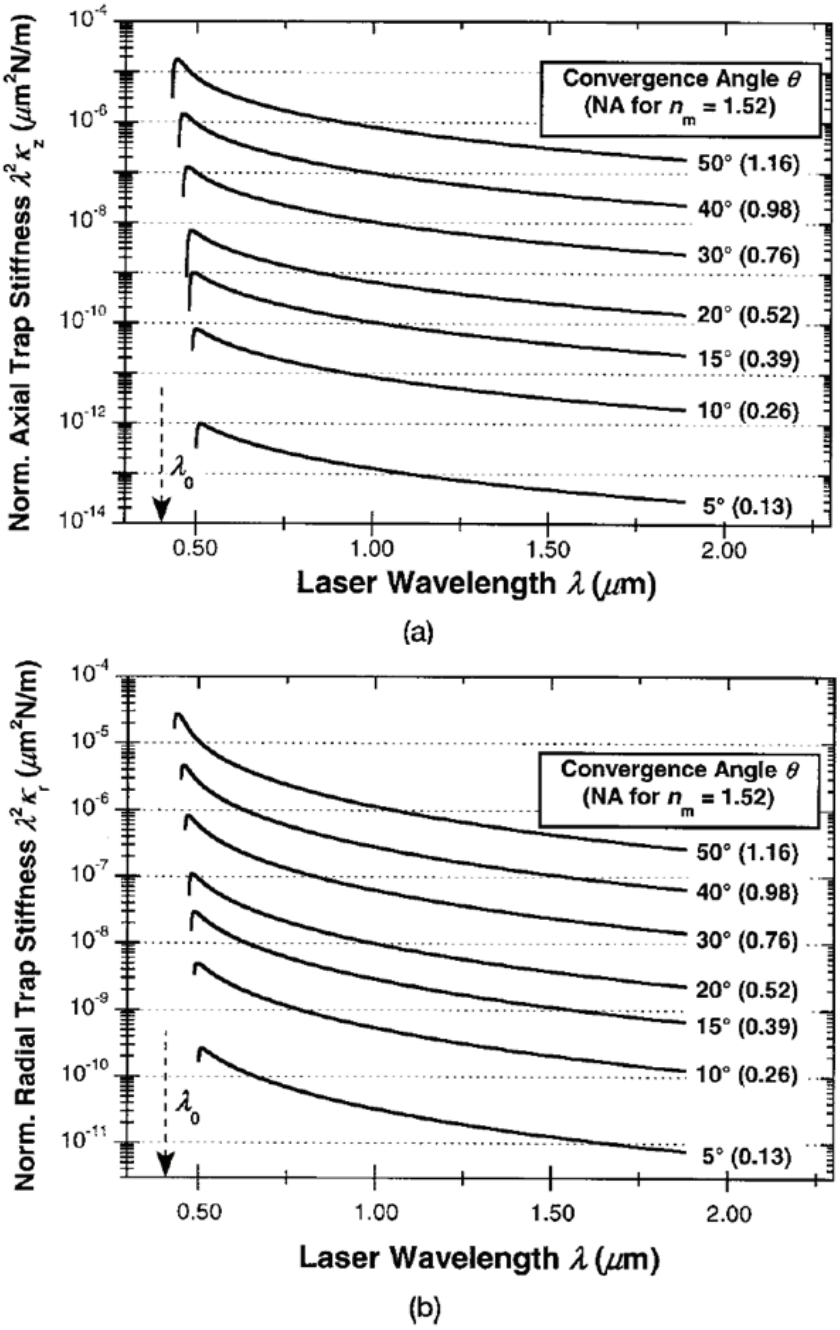

Figure 2.3: Trap stiffness for the axial direction (a) and radial direction (b) of a pink ruby particle in an optical trap are plotted as a function of trapping wavelength for many numerical aperture lenses. Above $\theta = 50°$, the paraxial approximation for the focused Gaussian intensity profile incident beam breaks down. The imaginary part of the polarizability has been modeled with a Gaussian. Plots are shown for different numerical apertures to show that higher NA results in higher overall stiffness. Plots taken from Agayan *et al* [10].

The previous section describes trapping for dielectrics. For a modeled system of an optically trapped Rayleigh metallic particle whose resonance absorption is a plasmonic effect, enhanced forces are expected for trapping near resonance as well [29]. In addition, experimental results show that trapping forces for a metallic particle, when compared to those for an equivalent system with a dielectric particle, are increased by a factor of up to seven, which is also equal to the ratio of the polarizabilities of the particles [4, 30].

For stable optical trapping of a particle, the gradient force must overcome the scattering force. For trapped particles whose absorption spectrum exhibits a resonance peak (Rayleigh particles), the trap strength will depend on the shape and location of the absorption curve. It is predicted that no trapping will occur when the trapping beam wavelength is the same as the absorption curve peak wavelength, where the scattering force is a maximum and the gradient force is zero (Figure 2.3(a)). There should be an onset of trapping as the beam wavelength is red detuned from the resonance absorption peak of the trapped particle, and this will most likely occur close to the absorption peak. Trapping should be strongest at the onset wavelength and should diminish as the trapping wavelength increases (Figure 2.3(b)). If the trapping wavelength is blue-detuned from the resonance wavelength, we expect no enhanced trapping since the gradient force points away from the most intense region of the beam (Figure 2.3(c)).

It should be noted that the terminology describing the interaction of light and matter used here was specific for an atom or ensemble of atom-like particles. Therefore, only absorption is spoken of as a mode of interaction. For larger particles,

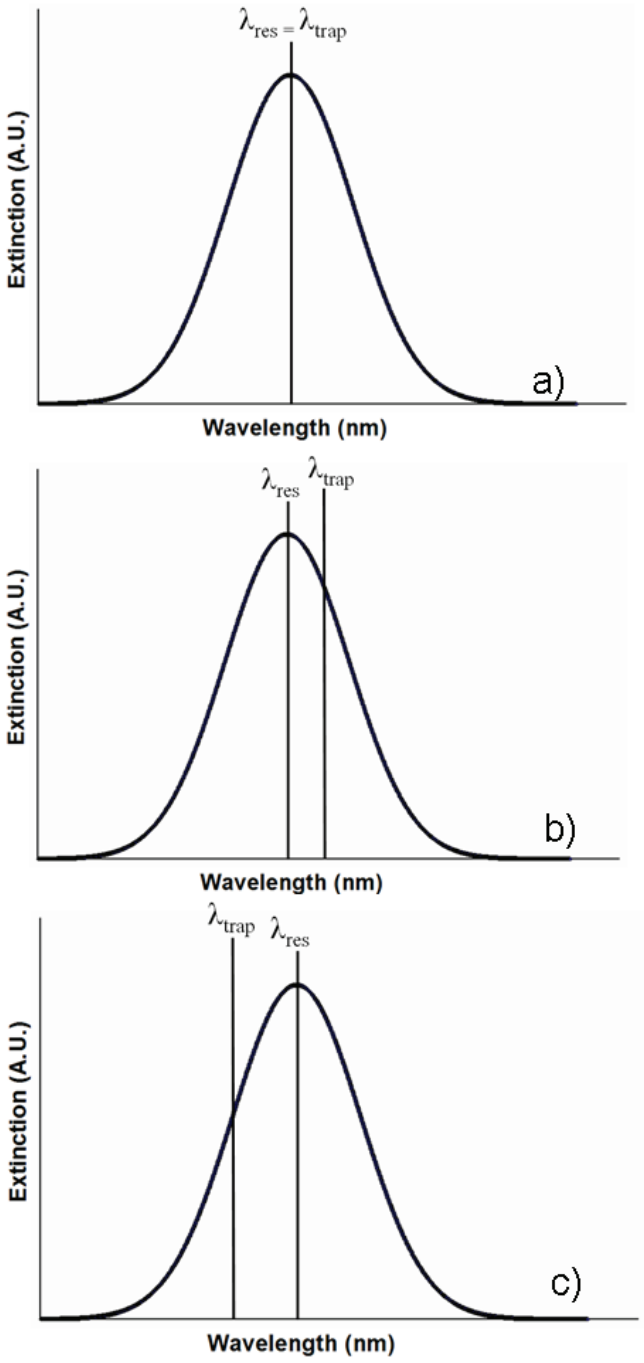

Figure 2.4: Three regimes of resonance absorption and trapping wavelength are shown. In (a), the trapping wavelength is the same as the resonance wavelength. In (b), the trapping wavelength is red-shifted from the resonance wavelength. In (c), the trapping wavelength is blue-shifted from resonance. Enhanced trapping is expected only for situations depicted by Figure (a).

light may also reflect from a surface or refract within the particle medium. Either interaction is regarded as light scattering. Therefore, for the ensembles of dipoles and for larger particles (discussed in the next section), as is common in the optics community, what was known here as absorption will be called "extinction", which is the sum of light scattering (where light is diverted) and light absorption (where light is absorbed and its energy converted to heat).

2.3.2 Mie Particles

While Rayleigh particles are those much smaller than the wavelength of light incident upon them, those whose size is on the order of the light wavelength or much larger are known as Mie particles. Most optical tweezer experiments employ Mie (dielectric) particles with diameters ranging from several hundred nanometers to 2 μm. Even though most of the carefully measured data offered by optical tweezers experiments is from within this size regime, it is the least understood, theoretically. The theory describing optical tweezers systems in this regime is still under development, but a basic understanding for Rayleigh particles and very large Mie particles does exist. A Rayleigh particle in a uniform field is described as an oscillating dipole and a very large illuminated Mie particle can be described with geometrical optics. It is this region in-between, when the particle size is on the order of the trapping wavelength, that requires a much more in-depth and rigorous description of the interaction of light and matter.

As the size of a particle increases, its interaction with certain light wavelengths

will become more complicated so that an oscillating dipole in a homogeneous field no longer satisfies as a true description of the system. Multipole effects in particular will become important and neither the Rayleigh theory nor the geometrical optical theory will offer a correct description. However, Lorenz-Mie scattering theory offers an analytical solution to the scattering of light from an arbitrarily sized sphere, and therefore offers a solution to the optical trapping of arbitrarily sized spheres.

Lorenz-Mie theory achieves the characterization of scattering by decomposing an incident plane wave (Lorenz-Mie theory) or arbitrary beam (generalized Lorenz-Mie theory) into vector spherical harmonics [21]. Classic boundary conditions requiring the continuity of tangential fields across interfaces allow for the definition of Mie coefficients for whole spheres or multi-layered structures [31, 32, 33]. With the Mie coefficients, optical force calculations are achieved by evaluating the integral of the Maxwell stress tensor over an arbitrary closed surface enclosing the object in question. Then the momentum transferred to the particle in the scattering process can be found.

The field describing the incident beam is a solution to Maxwell's equations decomposed onto the incoming spherical harmonics and, with higher order corrections to Gaussian beams, can describe realistic beams with a tight focus [34]. The decomposition into spherical harmonics requires a very slow convergence, so many alternatives exist, including the localized beam model[35, 36], partial waves [37], or s-expansion methods [38]. One popular method is the use of a least-squares fit to produce a Helmholtz beam with far-field matching that results from the high degree of focusing of the incident beam by the objective lens [39]. The incoming field can

be written as a discrete set of basis functions $\Psi_i^{(inc)}$, where i is the mode index label. Each function is a solution of the Helmholtz equation.

$$\nabla^2\Psi + k^2\Psi = 0 \tag{2.29}$$

Hence the incident field is:

$$U_{inc} = \sum_i^{\infty} a_i \Psi_i^{(inc)}, \tag{2.30}$$

where a_i are the expansion coefficients for the incident wave. The scattered wave is described similarly:

$$U_{scatt} = \sum_j^{\infty} p_j \Psi_j^{(scatt)}, \tag{2.31}$$

where p_j are the expansion coefficients for the scattered wave. While the interaction of the particle and the wave is linear, the relationship between the incoming and outgoing fields is also linear, and can be expressed as

$$p_j = \sum_i^{\infty} T_{ij} a_i, \tag{2.32}$$

where T_{ij} are the elements of the stress tensor, which for non-spherical particles is also known as the T-matrix.

The best choice for the set of basis functions for a finite spherical particle are the vector spherical wavefunctions as follows [40, 41, 42, 39].

$$\mathbf{E}_{in} = \sum_{n=1}^{\infty} \sum_{m=-n}^{n} a_{nm}\mathbf{M}_{nm}^{(2)}(k\mathbf{r}) + b_{nm}\mathbf{N}_{nm}^{(2)}(k\mathbf{r}), \tag{2.33}$$

$$\mathbf{E}_{out} = \sum_{n=1}^{\infty} \sum_{m=-n}^{n} p_{nm} \mathbf{M}_{nm}^{(1)}(k\mathbf{r}) + q_{nm} \mathbf{N}_{nm}^{(1)}(k\mathbf{r}), \tag{2.34}$$

with $\mathbf{M}_{nm}^{(1)}$ and $\mathbf{N}_{nm}^{(1)}$ as the outward propagating TE and TM multipole fields and $\mathbf{M}_{nm}^{(2)}$ and $\mathbf{N}_{nm}^{(2)}$ as the inward propagating multipole fields:

$$\mathbf{M}_{nm}^{(1,2)}(k\mathbf{r}) = N_n h_n^{(1,2)}(kr) \mathbf{C}_{nm}(\theta, \phi), \tag{2.35}$$

$$\mathbf{N}_{nm}^{(1,2)}(k\mathbf{r}) = \frac{h_n^{(1,2)}(kr)}{krN_n} \mathbf{P}_{nm}(\theta, \phi) + N_n \left(h_{n-1}^{(1,2)}(kr) - \frac{n h_n^{(1,2)}(kr)}{kr} \right) \mathbf{B}_{nm}(\theta, \phi), \tag{2.36}$$

where $h_n^{(1,2)}(kr)$ are spherical Hankel functions of the first and second kind, $N_n = [n(n+1)]^{-1/2}$ are normalized constants, and $\mathbf{B}_{nm}(\theta, \phi) = \mathbf{r} \nabla Y_n^m(\theta, \phi)$, $\mathbf{C}_{nm}(\theta, \phi) = \nabla \times (\mathbf{r} Y_n^m(\theta, \phi))$, and $\mathbf{P}_{nm}(\theta, \phi) = \hat{\mathbf{r}} Y_n^m(\theta, \phi)$ are the vector spherical harmonics [40, 41, 39, 42], and $Y_n^m(\theta, \phi)$ are the normalized scalar spherical harmonics with the common polar spherical coordinates θ and ϕ.

The stress tensor components are as follows:

$$T_{ij}^M = \epsilon \vec{E}_i \vec{E}_j + \mu \vec{H}_i \vec{H}_j - \frac{1}{2} \left(\epsilon \vec{E}^2 + \mu \vec{H}^2 \right) \delta_{ij} \tag{2.37}$$

where ϵ and μ are the permittivity and the permeability of the medium surrounding the object, respectively, and the vectors $\vec{E}, \vec{H}$ are the final electric and magnetic fields outside the object. The Maxwell stress tensor is used to find the optical force acting on the object, which for steady state conditions considers the time-averaged values only. This force is

$$\langle F_i \rangle = \langle \oint_s \sum_j T_{ij}^M n_j dS \rangle \tag{2.38}$$

where T_{ij}^{M} are the components of the Maxwell stress tensor and n_j are the components of the unit normal vector pointing outwards from the integration surface S [20].

The stress tensor is dependent only on the properties of the scatterer, so for any one particle, the stress tensor is calculated once, and then an incoming field is applied to find optical forces and torques [43]. This makes the choice a simple one for those who wish to calculate optical forces for optical tweezers; using the T-matrix approach allows for one calculation to describe the particle, to which many differing incoming fields may be applied.

Mie particles also exhibit optical extinction resonances, which are explained in Chapter 3 of this work. Like Rayleigh particles, the optical forces governing their interactions in an optical trap are dependent on resonant behavior, but this interaction is not easily predicted or understood like the Rayleigh particle system. The methods described above were utilized to predict how optical stiffness might change according to extinction resonance for dielectric particles whose size is on the order of the trapping wavelength, trapped over a wide wavelength range. Stilgoe *et al* calculated the trap stiffness for single optically trapped particles as a function of radius over trapping wavelength in the medium, as shown in Figure 2.4 [9]. This calculation was repeated for several relative refractive indices of particle and medium, so in order to learn how the stiffness will change with wavelength for a particular particle in a particular medium, one must draw a horizontal line across the plot in Figure 2.5, corresponding to the relative refractive index. Typically, polystyrene (n=1.55) or silica (n=1.45) particles are trapped in water (n=1.33) in

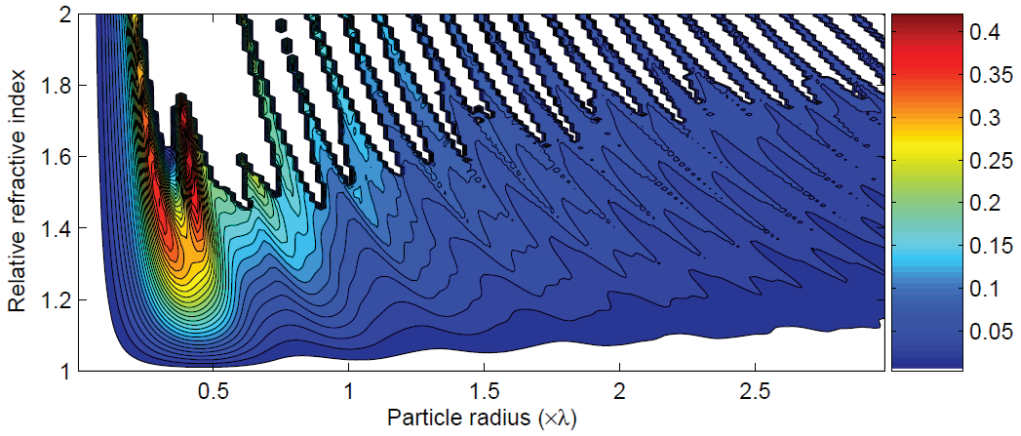

Figure 2.5: Radial spring constants for particles trapped with an NA = 1.3 lens. Trap stiffness is shown only for particles which are also axially trapped. Taken from Reference [9].

optical tweezers experiments, corresponding to a relative refractive index of 1.17 for polystyrene in water or 1.09 for silica in water. For such a system, the highest stiffness will occur for particles whose radius is roughly two-fifths the trapping wavelength in water. Over a relatively small scale, where the radius divided by the trapping wavelength in water ranges from 0.65 to 0.4, the trap stiffness is increased by a factor of roughly 3.5 times. This increase is achieved simply by varying the trap wavelength for a given particle radius. This enhancement would increase for particles with higher indices of refraction, but such beads are not readily available for optical trapping experiments.

When the particle size is significantly larger than the trap wavelength, as it is when the ratio of particle radius to trap wavelength is higher than 1.5, it appears from Figure 2.4 that resonance no longer plays a major role in the enhancement of trap stiffness. Instead, from one small wavelength interval to the next, small

variations (ripples) in trap stiffness are visible, but large increases and decreases are not. This is consistent with the commonly accepted view that, for this size regime, resonance (or particle size with respect to trap wavelength) should not play a part in the optical forces of a tweezer system. In a general sense, within this geometrical optics regime, the beam waist is vanishingly small compared to the diameter of the particle, and so for all particles in this regime, the ratio of diameter to trap size is constant [12].

Observations of Mie resonances in optical experiments are not new; Arthur Ashkin demonstrated the effect of Mie resonances on optical radiation pressure forces, using large spherical particles (4 - 30 μm in diameter) with a tunable dye laser (565-625 nm) [44]. This places Ashkin's experiment in the region of Figure 2.4 mentioned above: where a ripple structure exists for trap stiffness versus trap wavelength, but where greatly enhanced forces are not expected. Silicone oil liquid drops were levitated at a constant height with the laser, and the required laser power was recorded for various laser wavelengths. Over the wavelength range, a ripple structure was observed, and the required laser power for constant levitation height underwent a maximal change of 25%. This is hardly a significant enhancement in trap strength. However, the interest of the experimenters was very precise measurements of particle size, as the location of the peaks in the ripple structure is very highly dependent on the size of the levitated particle [44]. While this experiment did not focus on enhanced trapping with respect to trap wavelength and resonance, it also utilized only the scattering force and not the gradient force, since particles were levitated and stabilized using the opposing force due to gravity.

2.4 Discussion

Enhanced forces should exist for particles exhibiting an extinction resonance when they are trapped at certain wavelengths. In the Rayleigh approximation, the optical forces are decomposed into an easily understood gradient and scattering force. We expect that the overall trap strength will increase as the trap wavelength approaches the resonance from the red side. At the resonance, it should drop sharply as the scattering force comes to a maximum. On the blue side of resonance, we expect no stable trapping, as the gradient force is repulsive there. Theory predicts that the trapping force exerted on a Rayleigh particle is enhanced and may be three to fifty times larger for frequencies near resonance than for frequencies far from resonance [10].

As the size of the particle increases, the Rayleigh approximation is no longer valid and one must consider higher order corrections. The Lorenz-Mie scattering theory allow for these necessary corrections. A direct numerical calculation of optical forces is made possible by using finite elements methods and integrating Maxwell's stress tensor over the particle volume. With this technique, calculations can be completed for particles ranging from those in the Rayleigh regime to the large Mie regime. Based on these calculations, enhanced trapping should occur for particles spanning the entire range with the proper tunable laser. Furthermore we can measure these trapped methods using either the power spectrum method or the equipartition method.

Chapter 3

Rayleigh and Mie particles

3.1 Particles used for Trapping

The two particle types utilized for this study were gold nanoshells and dielectric (polystyrene or silica) microspheres. A gold nanoshell is a small silica sphere coated with a thin, uniform layer of gold. Based on the overall size and the gold thickness, its extinction resonance can be tuned from the visible to the infrared. The gold nanoshells used here were fabricated by our colleagues at Rice University. We optically trapped several species of nanoshells with diameters ranging from 100 nm to 200 nm, with extinction resonances centered at wavelengths ranging from 650 to 950 nm. Gold nanoshells serve as the Rayleigh particles for this experiment. We also optically trapped uncoated polystyrene and silica spheres ranging in diameter from 390 nm to 5.5 μm (Bangs Laboratories, Fishers, IN), serving as the Mie particles for the experiment.

3.2 Gold Nanoshells

3.2.1 Nanoshells as Rayleigh particles

Nanoparticles have become the subject of intense scientific research owing to their wide range of applications in biomedical, electronic, optical, and other arenas.

As the bridge between molecular units and bulk materials, they provide a venue for the study of substances whose properties change with size. Of noteworthy significance are the optical properties of nanoparticles. In particular, the metal nanoshell, due to its predictable interaction with light, has shown great promise for several applications [45, 46, 47, 48]. Since nanoshells have substantial and controllable optical scattering and absorption, they can be designed to interact with light primarily at wavelengths that are minimally invasive to biological tissue. Therefore they can produce localized internal heating and can be used as selective photo-tumor ablation tools. For example, gold nanoshells have been used to destroy cancerous tumors in mice [47].

The outer layer of a gold nanoshell is chemically equivalent to that of a typical gold nanoparticle commonly used for biological imaging techniques. Small gold nanoparticles can be used to easily tag molecules like proteins for identification by electron and optical microscopy. Several protocols for attaching gold colloids to biological molecules are already in practice. Gold nanoshells have been utilized in imaging techniques as contrast agents for optical coherence tomography (OCT) to image carcinoma cells [48].

Heating and imaging are not the only mechanisms to be exploited from nanoshells exposed to light. As discussed in Chapter 3, theory suggests that if a Rayleigh particle has an extinction resonance peak, then ehnanced optical trapping can occur by using a trapping beam wavelength slightly red shifted from that resonance [10]. By controlling the overall radius and depth of the gold layer, gold nanoshells can be tuned for maximal extinction within a broad wavelength range including the

visible to the infrared region, making it possible to exploit this effect for several applications. With such tunable trapping, these nanoparticles could be used for optical sorting by selectively trapping particles of a distinct resonance. In future cancer therapy research studies, localized delivery of nanoshells with optical tweezers would be possible for determining ideal cell sites. Additionally, nanoshells could be used as probes for optical tweezer bio-force measurement studies. In this case, it would be advantageous to choose a trap wavelength exhibiting maximal trapping forces and minimal heating effects. Perhaps most useful would be to enhance the overall understanding of optical trapping of nanoparticles that exhibit a single extinction resonance.

3.2.2 Predicting Nanoshell Resonance

Small spherical particles composed entirely of metal are known to possess strong optical resonances and fast nonlinear optical polarizabilities, both linked to the plasmon frequency [49, 50]. These effects are well described by classical electrodynamic Lorenz-Mie (Mie Scattering) theory [51]. A sphere with a core of one medium and a uniform coating composed of a second medium also exhibits an optical resonance, and the Lorenz-Mie solution to this system is also well-known [52]. For our system, where the sphere has a dielectric core and a metal coating, the resulting optical resonance arises from the plasmon frequency but also exhibits tunability across a wide spectrum, from the ultraviolet to the infrared, depending on the cladding thickness parameter r1/r2, where r1 is the radius of the dielectric

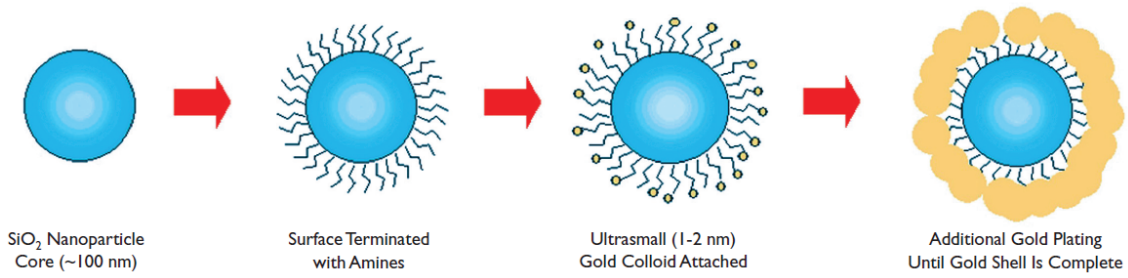

Figure 3.1: Nanoshell fabrication technique, taken from [53]

core and r2 is the overall radius of the sphere [45].

Such spheres, named nanoshells, are synthesized by combining molecular self-assembly techniques with those of metal colloid synthesis [46]. The particles are fabricated using the following method, as shown in Figure 3.1.

Silica cores are grown using the Stöber method [54]. Organosilane molecules are then bound to the surface of the silica sphere, with amine groups oriented away from the center of the core, creating a new outer surface. A solution of gold colloid whose nanoparticles have a diameter of one to two nanometers is then added, and the gold bonds to the amine groups. Chemical methods are used next to continue the attachment of the gold colloid onto the sparsely populated gold surface. This is achieved by adding an aged mixture of chloroauric acid and potassium carbonate, reduced by a solution of sodium borohydride. The few initial gold particles attached to the amines serve as nucleation sites for a reduction reaction, and after some time gold evenly covers the surface [46]. Experimental evidence agrees with Lorenz-Mie theory calculations in predicting the locations of extinction peaks in the electromagnetic spectrum for synthesized nanoshells [55, 46].

The extinction resonance of a nanoshell is mostly dependent on its plasmon resonance, defined here. A plasmon will occur in a bulk metal when the conduction electrons undergo a collective oscillation. The rigid displacement of the electrons induces a dipole moment and an opposing electric field. The electron cloud will oscillate with the applied field and behave somewhat like a harmonic oscillator. The bulk plasmon frequency, ω_B, can be determined via traditional methods and is found to be dependent on the electron density. When light is incident upon a conductor/dielectric interface, an excitation of longitudinal surface electromagnetic waves may occur, as in Figure 3.2. These excitations, called surface plasmon polaritons (SPPs), propagate parallel to the metal/dielectric interface, and result from the collective behavior of the free-electron cloud or conduction electrons. For a curved metallic nanostructure in a dielectric medium, the excitations are non-propagating, and are known as localized surface plasmons or localized plasmons. The curvature exerts an effective restoring force on the electron cloud, resulting in a resonance. It also allows the excitation of localized plasmons by direct illumination, rather than with phase-matching (momentum-matching) techniques required for SPPs [56].

The plasmon resonance behavior of a metal nanoparticle in the quasi-static approximation is dominated by the dipolar behavior of the particle. The effectively static applied electric field induces a dipole moment inside the sphere, proportional to the applied field amplitude. The proportionality is defined by the polarizability, α, where the dipole moment is $\vec{p} = \varepsilon_0 \varepsilon_m \alpha \vec{E}_0$ and $\alpha = 4\pi a^3 \frac{\varepsilon - \varepsilon_m}{\varepsilon + 2\varepsilon_m}$. $\vec{E}_0$ is the applied electric field (a monochromatic plane wave), $\vec{p}$ is the dipole moment, ε is the dielectric function of the sphere, ε_m is the dielectric function of the medium,

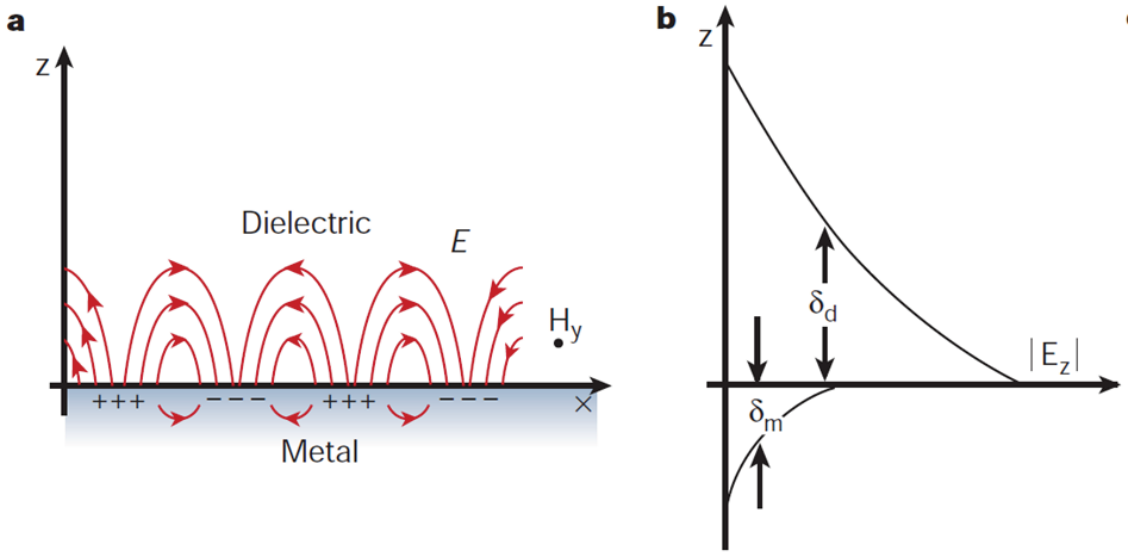

Figure 3.2: (a) The electric field lines for an instantaneous surface plasmon at a metal-dielectric interface. Pluses indicate regions of low electron density and minuses indicate regions of high electron density. (b) For the picture in (a), the electric field amplitude decreases exponentially from the interface with characteristic dielectric decay length δ_d determined by the light wavelength and characteristic metal decay length δm determined by the skin depth. Taken from Ref [57]

$\varepsilon_0 = \varepsilon(\omega)$ is the dielectric function of the metal, and a is the radius of the particle. When the polarizability is at a maximum, then the induced dipole moment is at a maximum, and this is called a resonance. This occurs at $Re[\varepsilon(\omega)] = -2\varepsilon_m$, called the Fröhlich condition, and the resulting mode is the dipole surface plasmon of the metal nanoparticle. The dipole oscillates following the applied field, and the radiation of this dipole leads to scattering of the plane wave by the particle, and can be interpreted as radiation by a point dipole [58]. Some phase retardation will occur for particles large enough to see amplitude changes in the electric field. This allows higher order modes (quadrupole, etc.) to interact with the light, although their effects are overshadowed by the dipole interaction [59].

Plasmon resonance frequencies occur for metal nanoshells and the strong factor for extinction spectrum location and shape is the geometry of the particle. The plasmon resonance depends on the relative size of the core and the shell, and gives rise to an extinction resonance. This is most easily understood by considering the nanoshell plasmon hybridization model, which is based on the interaction between the separate response of both a metal nanosphere and a metal nanocavity, as shown in Figure 3.3. For each, the metal is in contact with a dielectric, and when light is incident upon either system, plasmons will appear and will induce surface charges at the inner interface for the cavity and the outer interface for the nanosphere. For a nanoshell, both will occur, and the sphere and cavity plasmons will form an interaction whose strength is controlled by the distance between them, or the shell thickness. The combination of the two plasmons will form a mode that is either "bonding", low-energy, and symmetric or "antibonding," high energy, and

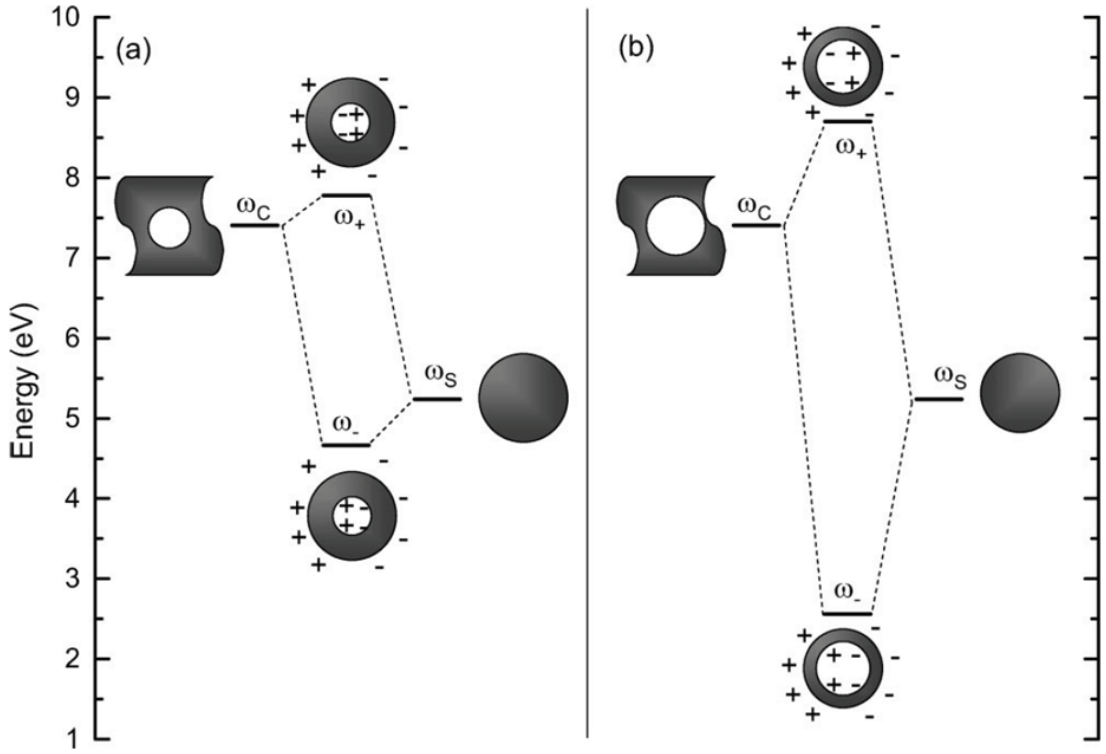

Figure 3.3: (a) Nanoshell energy for a symmetric (low energy) and antisymmetric (high energy) hybridization of a dielectric cavity (left) and metal sphere (right). (b) A nanoshell with the same overall size but thicker core and thinner shell will have a higher energy (more blue) antisymmetric configuration and lower energy (more red) symmetric configuration. Taken from Ref [60]

.

antisymmetric.

Intuitively, a thinner shell will result in a stronger hybridization interaction [61], giving rise to a strongly red-shifted resonance for the "bonding" plasmon whose central wavelength is determined by the shell thickness and overall size [62]. Figure 3.4 shows the normalized electric field intensity for nanoshells excited by light of their resonance wavelength. The symmetric configurations have a field enhancement outside of the nanoshell because the charges on the inner and outer surfaces are in phase. The antisymmetric configurations have a large dipole moment only inside the shell, concentrating the field there. The dipole resonance corresponds to a larger dipole moment and contributes more to scattering. The quadrupole configuration has dipoles across the gold coating, not across the entire particle, and therefore contributes more to absorption. For a constant core size, as the shell thickness decreases, this resonance shifts more and more towards the red. When holding the cladding thickness parameter constant, the overall particle size determines whether the particle will be more prone to absorb or scatter light with respect to incident wavelength. Smaller particles will behave as absorbing dipoles and larger particles will behave as scatterers with multiple modes and resonances [53].

Shown in Figure 3.5 are calculated Lorenz-Mie theory extinction curves for nanoshells with varied cladding thickness parameters. As the cladding thickness parameter decreases, the resonance peak location increases in wavelength. This allows for extinction-resonance-tuning from the ultraviolet to the infrared. The resonance curves in Figure 3.5 are calculated using the Lorenz-Mie theory solution for a spherical core with a spherical shell [21]. The material properties of the core

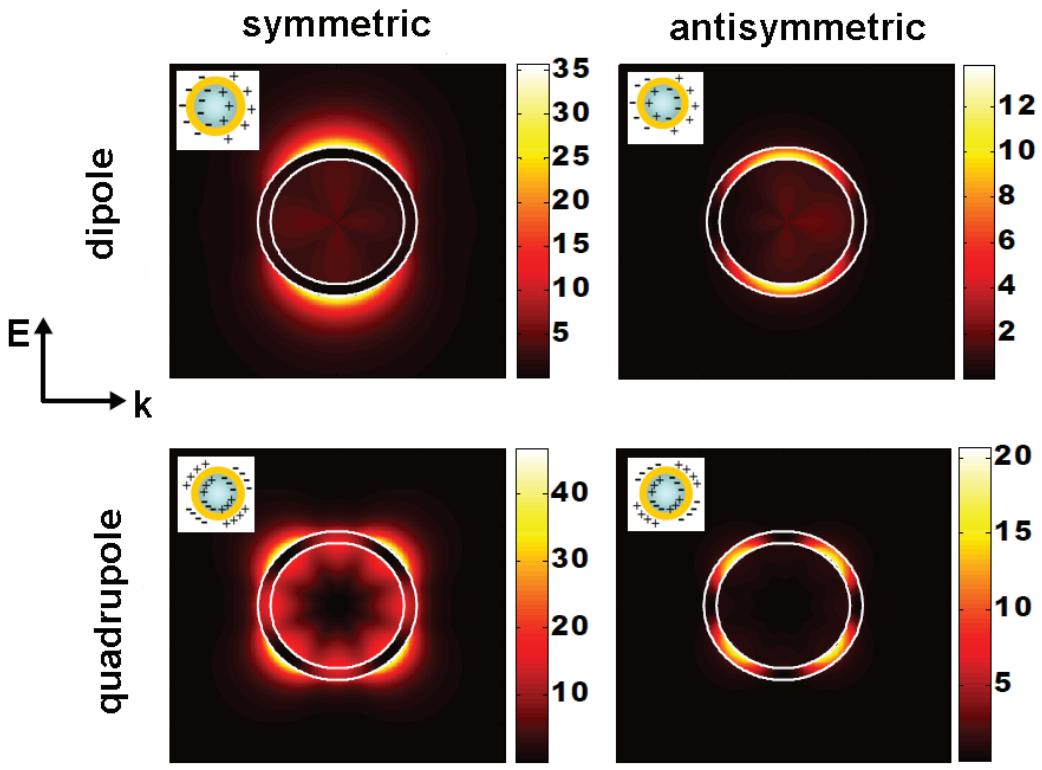

Figure 3.4: The normalized instantaneous electric field intensity is shown for a region of 200 by 200 nm surrounding a nanoshell with $r_1 = 80$ nm and $r_2 = 95$ nm. Light polarization is indicated to the left. For the left (symmetric) column, the nanoshell is excited with the resonance wavelength 742 nm. For the right (antisymmetric) column, the nanoshell is excited with the resonance wavelength 438 nm. The top row shows a dipole configuration and the bottom row shows a quadrupole configuration. Insets show the charge configuration for each. Taken from Ref [59]

.

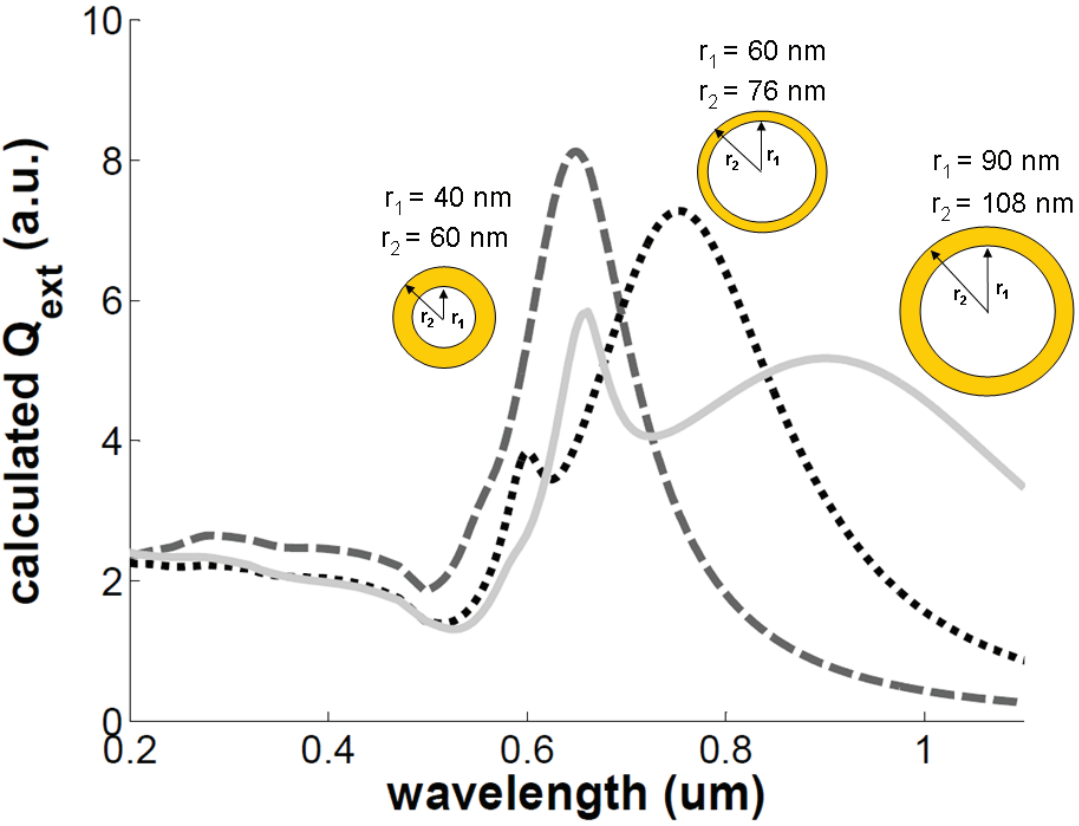

Figure 3.5: Calculated extinction spectra for three species of nanoshells. Calculations are performed for a single nanoshell in water. Species A has the extinction resonance peak centered at 650 nm. Species B has the extinction resonance peak centered at 770 nm. Species C has the scattering (dipole) resonance peak centered at 950 nm. A schematic of the cross section of each nanoshell is shown close to its extinction curve.

are the same as those for fused silica, and the properties of the shell are those of gold. The dielectric function of gold is based on interpolated results from Johnson and Christy and the Drude [63] model for free electron response. The plasma frequency of gold is calculated assuming that like all noble metals, gold has one conduction electron per atom, corresponding to a filled d band and one free s electron. The dispersion for fused silica is determined using Sellmeier's formula [64], although the spectra are unchanged when a constant parameter is used. The index of refraction of water is taken to be n = 1.33041 and independent of wavelength. The nanoshells featured in Figure 3.5 are the Rayleigh-particle subjects of this experiment.

Figure 3.6 shows the experimental bulk extinction spectra of the nanoshell species presented in Figure 3.5 above. The spectra are measured with a Spectronic Genesys 5 Spectrophotometer. The VisualBasic code necessary for operation and communication with the Spectrophotometer is included in the appendix of this work. Measurements are performed for bulk particles in water. Some differences between the calculated and measured spectra are evident. We see peak broadening due to particle inhomogeneity. Additionally, the nanoshell geometries are not exactly what was intended and are perhaps a nanometer larger or smaller for the inner or outer radius, which will cause significant differences in the peak locations of the measured spectra.

Scanning electron micrograph images of the three nanoshell species are shown in Figures 3.7 to 3.9. The smallest species of the three, species A, has the most particle-to-particle diversity, although it is quite minimal.

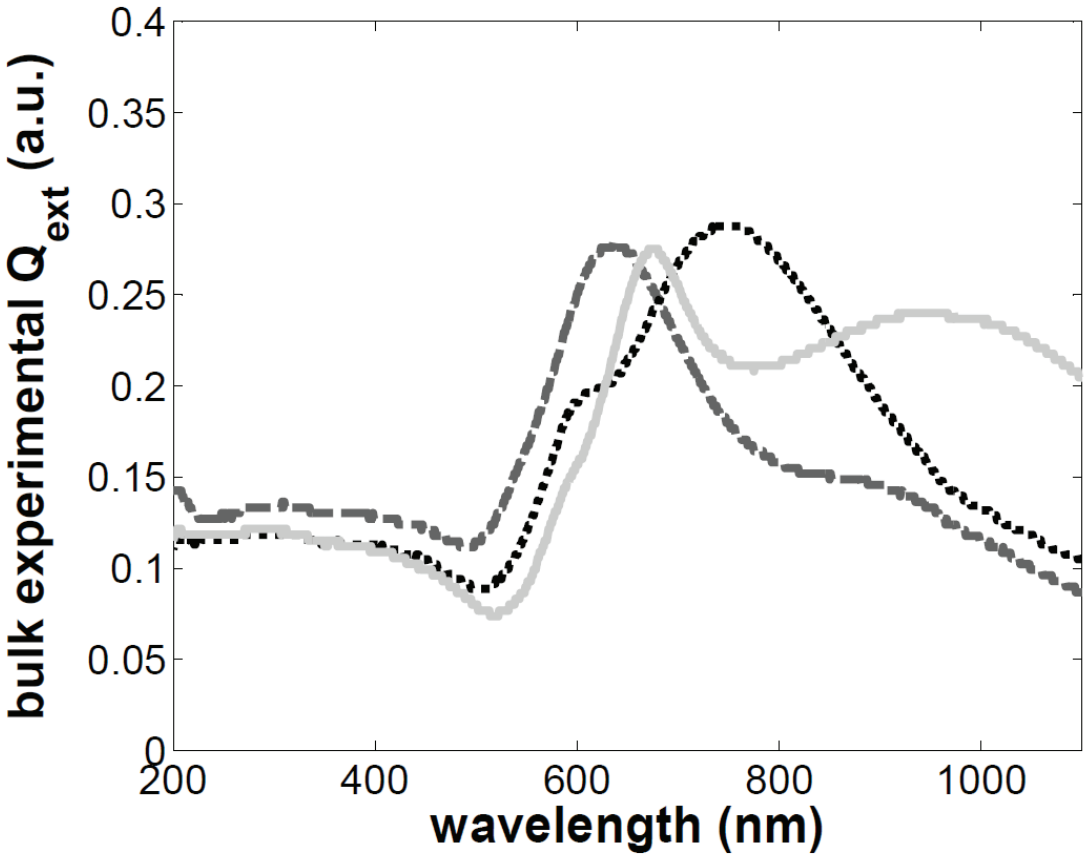

Figure 3.6: Experimental bulk extinction spectra for the three species of nanoshells described in Figure 3.5. Species A (gray dashed line) has the resonance peak centered at 636 nm. Species B (black dotted line) has the extinction resonance peak centered at 768 nm. Species C (light gray line) has the scattering resonance peak centered at 940 nm.

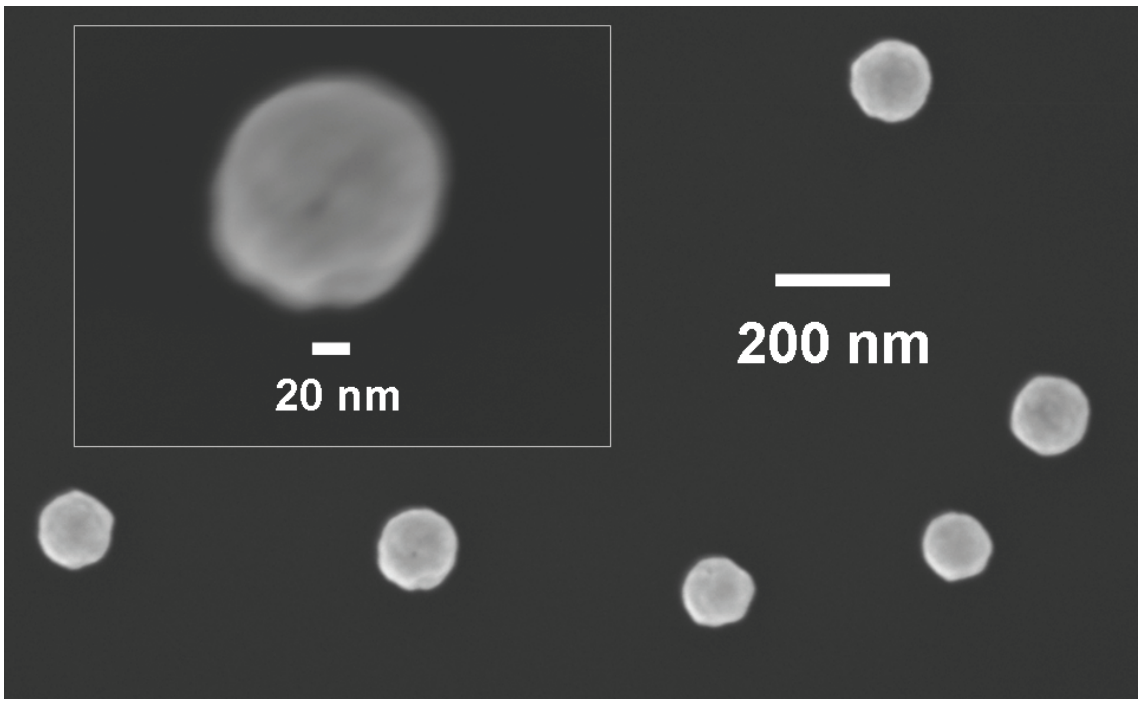

Figure 3.7: SEM micrograph of species A nanoshells.

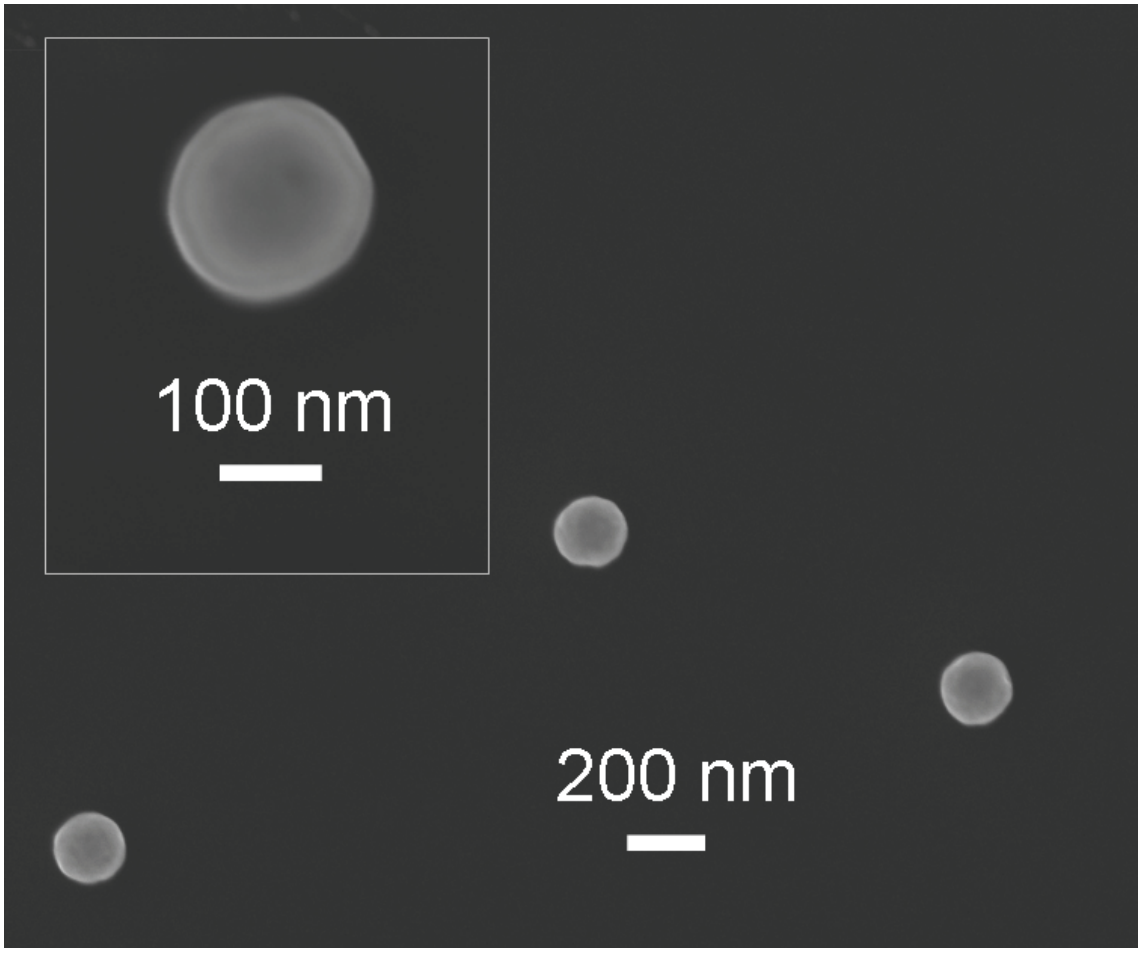

Figure 3.8: SEM micrograph of species B nanoshells.

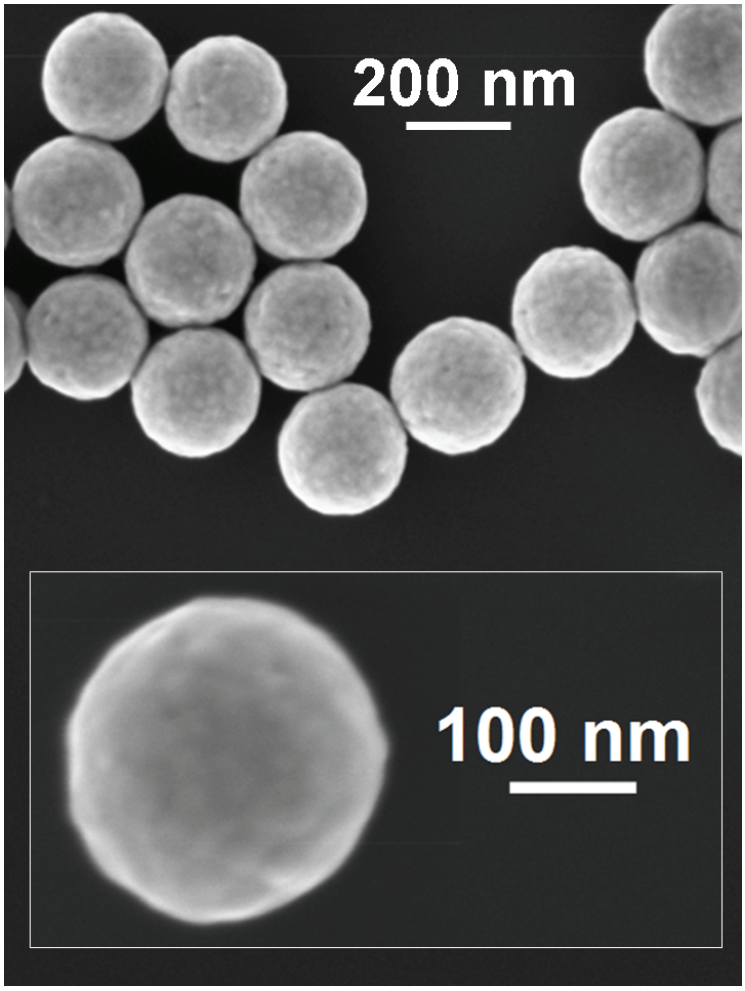

Figure 3.9: SEM micrograph of species C nanoshells.

3.3 Mie Particles and Resonance

While the interaction of light with a nanoparticle is somewhat easily understood as a simple dipole oscillating in an electric field, the situation for Mie particles is more complex. For a general system with a nonabsorbing particle, forces in the axial direction result firstly from backscattering (pushing the particle in the direction of light propagation) and secondly from a change in the convergence or divergence of the beam (increased convergence increases the axial momentum flux, leading to reverse restoring forces). Additionally, gradient forces result from the strong beam focusing, and they point in the direction opposite to light propagation and toward the beam center. When the diameter of the particle is on the order of the wavelength, or larger, more effects can occur, particularly at the surface and at the edges of the particle.

A plane wave is incident from infinity and strikes the sphere at certain angles with respect to its edges. Two things can happen: one, a distribution of fields and currents near the edges occurs, contributing to a percentage of the forward scattered light, and two, a wave motion continues along the surface of the particle and depending on its size, may reach to the other side. This second phenomenon was first identified by van de Hulst, and so the waves therefore are designated as "van de Hulst" waves [65]. Both effects can be seen in the extinction cross section of a Mie particle. Slow oscillations of the extinction cross section, Q_{ext}, manifest as periodic maxima and minima, whose amplitudes decrease as the size parameter $x = 2\pi r/\lambda$ increases, where r is the radius of the sphere and λ is the wavelength

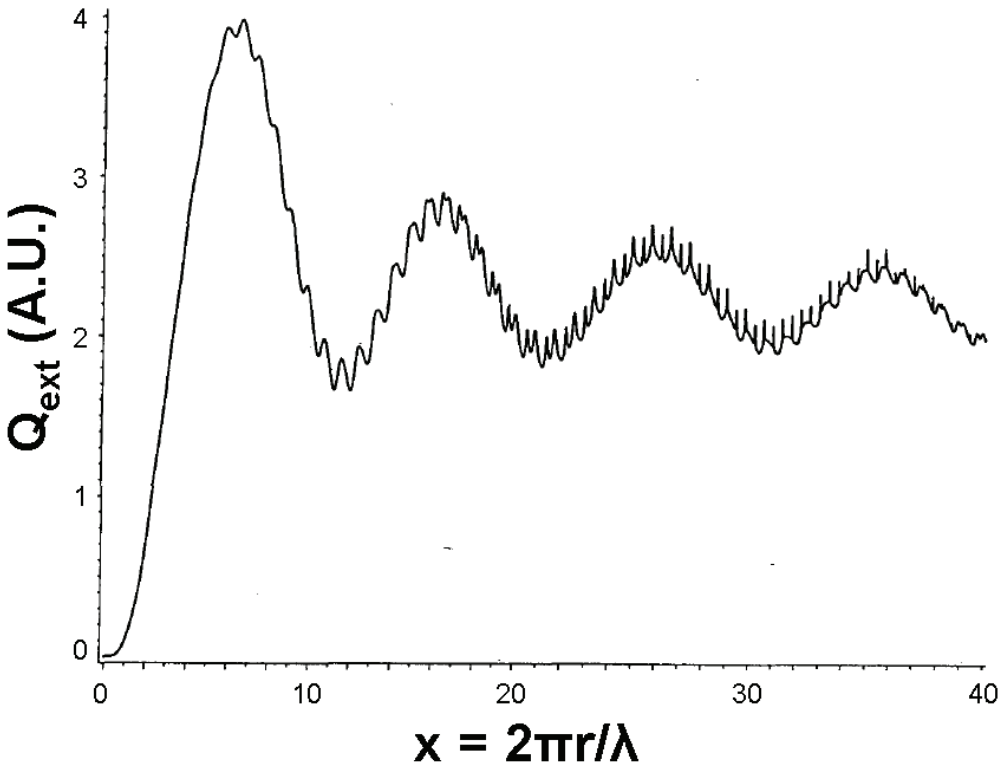

Figure 3.10: Normalized calculated extinction cross section for a dielectric sphere with refractive index 1.33. Taken from [66].

of light in vacuum. This is also known as the interference structure of the Mie particle since van de Hulst reasoned that the sequence of maxima and minima could be explained as an interference effect between the diffracted and transmitted waves [65]. Also evident in the extinction spectrum is a ripple structure superimposed on the interference structure due to resonances in the partial wave scattering amplitudes [66]. Figure 3.10 shows the interference and ripple structures for a sphere where the index of refraction of the sphere is assumed to be that of water.

The expression for the normalized extinction cross section is

$$Q_{ext}(x,n) = \frac{2}{x^2}\sum_{i=1}^{\infty}(2i+1)Re[a_i(x,n)+b_i(x,n)] \tag{3.1}$$

where the Mie scattering amplitudes are

$$a_i(x,n) = \frac{\Psi_i(x)\Psi_i'(nx) - n\Psi_i(nx)\Psi_i'(x)}{\zeta_i(x)\Psi_i'(nx) - n\Psi_i(nx)\zeta_i'(x)} \tag{3.2}$$

$$b_i(x,n) = \frac{n\Psi_i(x)\Psi_i'(nx) - \Psi_i(nx)\Psi_i'(x)}{n\zeta_i(x)\Psi_i'(nx) - \Psi_i(nx)\zeta_i'(x)} \tag{3.3}$$

where Ψ_i and ζ_i are the Ricatti-Bessel functions and Ψ_i' and ζ_i' are the derivatives with respect to their arguments.

For $x \gg 1$ and $n-1 \ll 1$ (parameters common for optical tweezer experiments), equation 3.1 becomes approximately

$$Q_{ext}(x,n) = 2\left(1 - \frac{sin[2x(n-1)]}{x(n-1)}\right) + \frac{1-cos[2x(n-1)]}{x^2(n-1)^2} \tag{3.4}$$

whose extinction curve closely resembles that calculated with equation 3.1, without the ripple structure. At large x the periodicity is due to the $sin[2x(n-1)]$ term, such that the periodicity is determined by the size parameter and the refractive index.

The resonances in the extinction cross section of a Mie particle are also evident in measurements of optical forces. Ashkin *et al* [13] observed resonances in the radiation pressure exerted on large dielectric spheres by levitating liquid silicone

drops in a laser beam. A single drop was held at a constant height (where the beam diameter was larger than the particle for "plane wave" incident light) while the laser wavelength was tuned over several nanometers and the laser power required to levitate drops was recorded. A ripple structure similar to that of the extinction spectrum was observed in the optical power vs. wavelength plot generated. The required laser power differed by up to 25% from one extrema to the next, but never showed highly enhanced optical forces. The source of the observed resonances was determined experimentally by placing the particle in the beam waist because it was expected that if the resonances were due to van de Hulst "surface waves" then only tangentially incident light should excite them. At the beam waist, light only passes through the center of the sphere and does not interact with the edges. For this situation, the ripple-like resonances disappeared in the radiation pressure spectrum while a broad force variation remained due to interference from multiple reflections of light within the sphere [44]. These interference-based resonances are also known as whispering-gallery modes (WGMs) and are basically light modes confined within the dielectric sphere by repeated total internal reflection. The sphere is viewed as a low-loss optical cavity whose internally circulating light can affect the reflectivity such that very strong coupling can occur. In former experiments, observations of WGMs have allowed for high-resolution measurements of particle size [13] and detection of surface elements [67], but not for enhancing optical forces.

Shown in Figures 3.11 and 3.12 are calculated Lorenz-Mie extinction curves for dielectric (silica and polystyrene) spheres with varied size. The curves are calculated using the Lorenz-Mie theory solution for a sphere[21]. The material properties

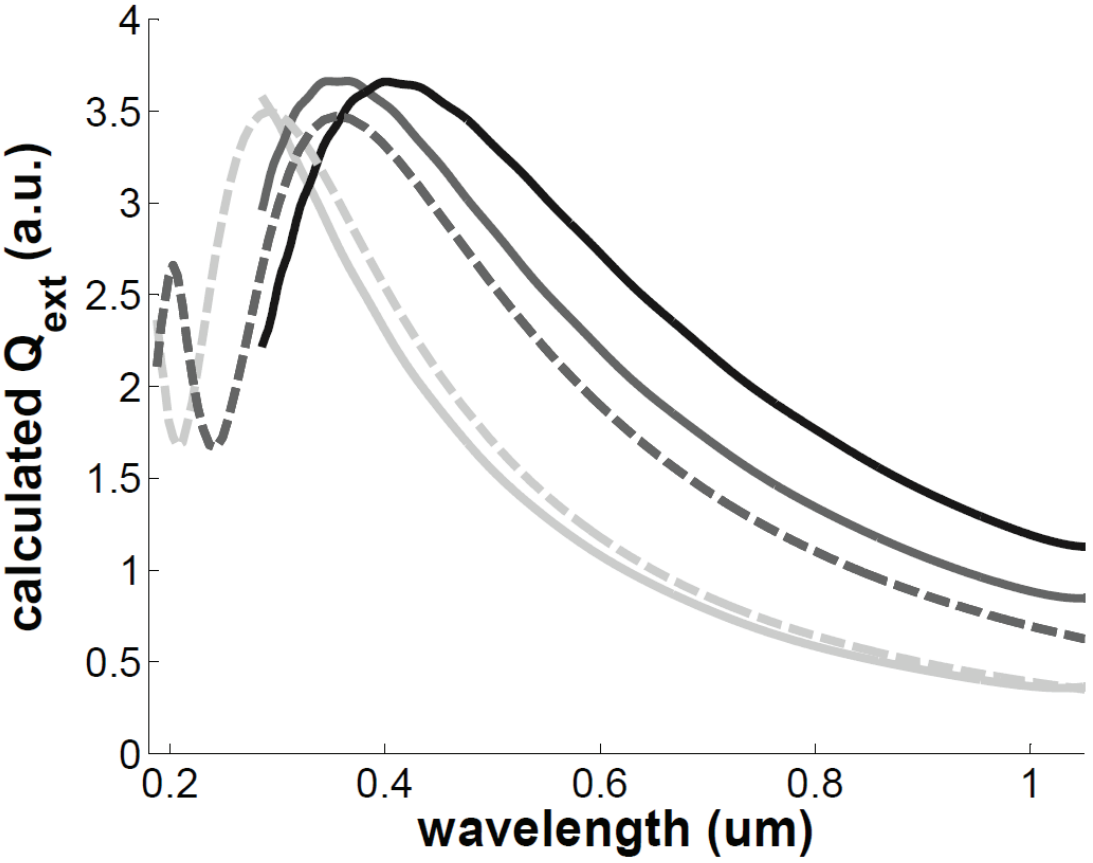

Figure 3.11: Calculated extinction spectra for a single dielectric sphere of varying small size. Light gray line is a 0.39 μm polystyrene sphere, dark gray line is a 0.59 μm polystyrene sphere, and black line is a 0.69 μm polystyrene sphere. Light gray dashed line is a 0.60 μm silica sphere and dark gray dashed line is a 0.80 μm silica sphere.

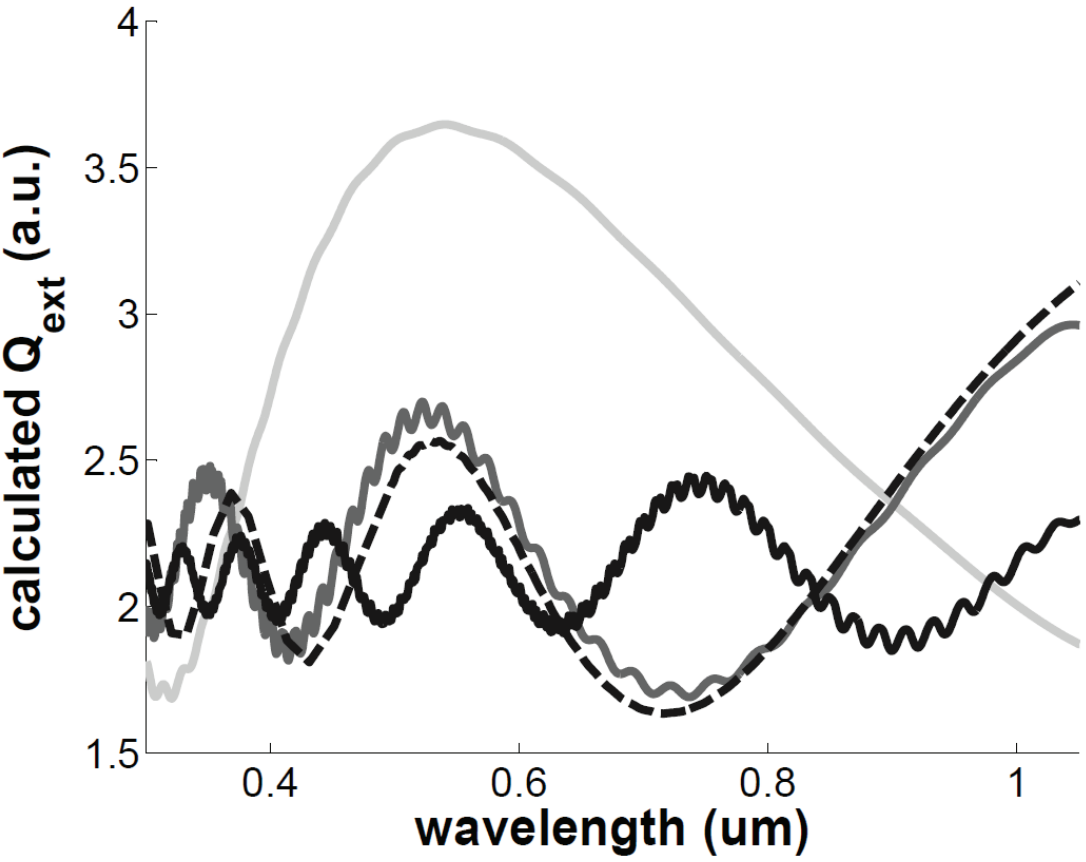

Figure 3.12: Calculated extinction spectra for a single dielectric sphere of varying large size. Light gray line is a 0.94 μm polystyrene sphere, dark gray line is a 2.4 μm polystyrene sphere, and black line is a 5.5 μm polystyrene sphere. Black dashed line is a 3.5 μm silica sphere.

of the sphere are the same as those for fused silica or polystyrene. The dispersion for fused silica is determined using Sellmeier's formula [64], although the spectra are unchanged when a constant parameter is used. The index of refraction of water is taken to be $n = 1.33041$ and independent of wavelength. The dielectric particles featured in Figures 3.11 and 3.12 are the Mie-particle subjects of this experiment. Experimental extinction spectra for these particles are included in Chapter 7. Scanning electron microscope (SEM) micrographs of the particles described in Figure 3.12 are included in Figures 3.13 to 3.16. These particles are not coated with any thin metal layer as is normally done in scanning electron microscope studies and so effects of concentrated charge are evident. The SEM images are included only to demonstrate particle size and homogeneity. So these charging effects, while considered in poor form within the SEM community, do not affect our intentions, and are rather aesthetically interesting.

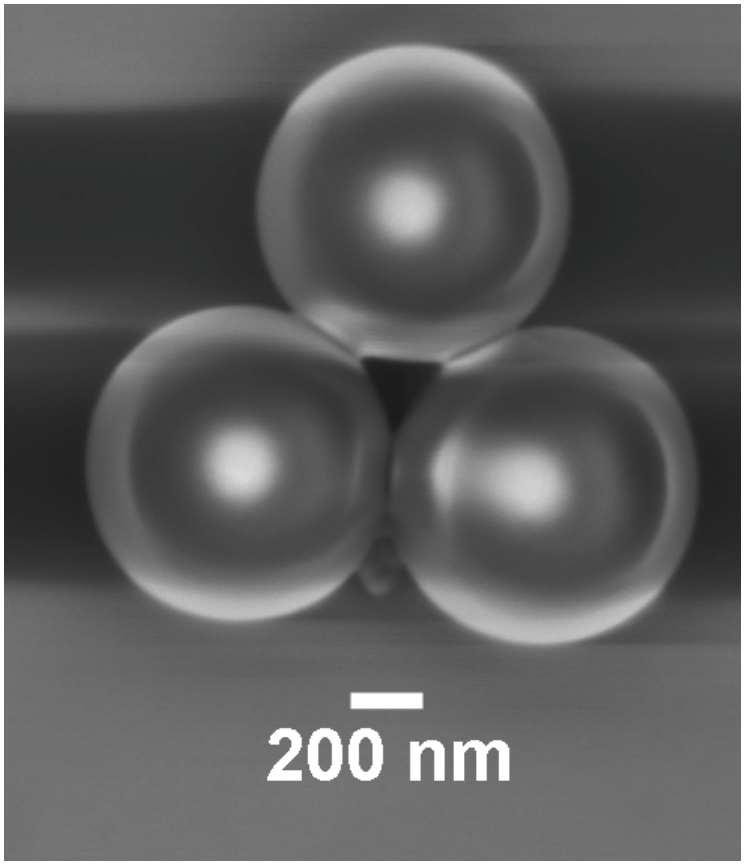

Figure 3.13: SEM micrograph of 0.94 μm polystyrene spheres

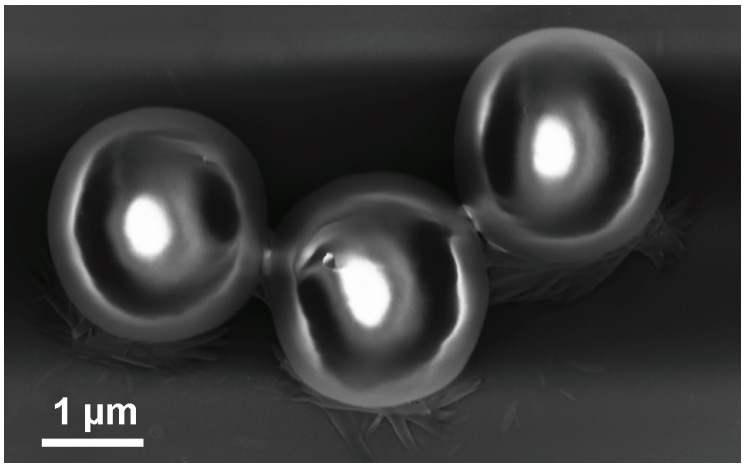

Figure 3.14: SEM micrograph of 2.4 μm polystyrene spheres

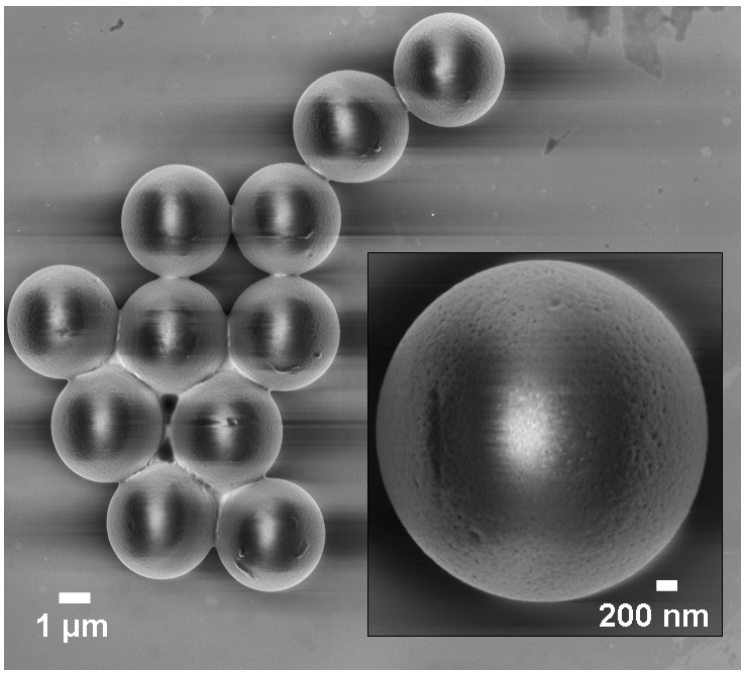

Figure 3.15: SEM micrograph of 3.5 μm silica spheres

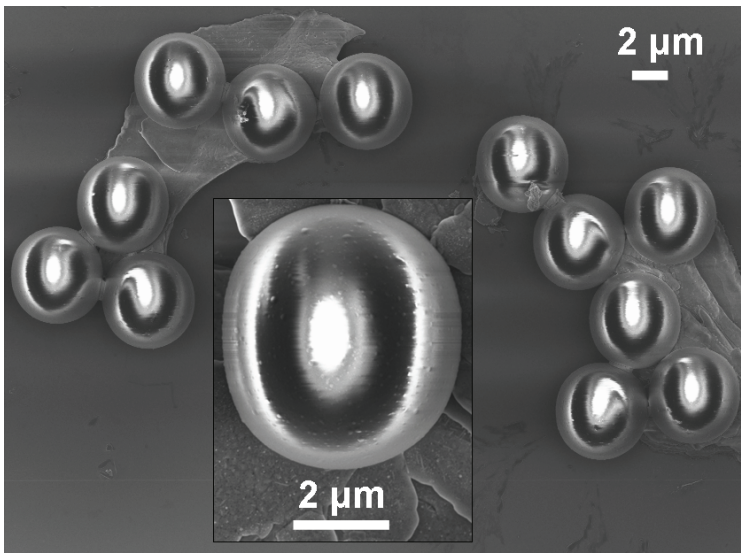

Figure 3.16: SEM micrograph of 5.5 μm polystyrene spheres

Chapter 4

Apparatus for Measurements of Trap Stiffness versus Wavelength

4.1 Apparatus I: Single wavelength laser system

The original apparatus designed for this study was comprised of several single wavelength lasers coupled into a single microscope objective for multiple beam trapping at a single sample plane. The system was designed so that the laser beam waists were aligned with each other in order to trap a single particle at various trapping wavelengths for comparison of trap stiffness. Details of the alignment technique are included in Chapter 5 of this work.

Figure 4.1 shows a schematic of Apparatus I with a top view of the experimental setup. The laser sources are a fiber-coupled continuous wave (CW) Nd:YAG (YAG) laser (1064 μm, 1.5 W, OEM laser systems, East Lansing, Michigan) and a diode laser (LD) (973 nm, 500 mW, Thorlabs, Newton, New Jersey). Polarizing beamsplitters (PBS1 and PBS2) and waveplates (W1 and W2) are used to manipulate optical power. The lasers are magnified by telescopes (L1 and L2, L3 and L4) so that they have the same diameter. A dichroic mirror (D1) couples the two beams into the same path. The beams are then steered into the trapping axis by a dichroic mirror (D2), then focused by a Zeiss Plan-Apochromat 63x oil immersion microscope objective (OL) with numerical aperture (NA) 1.4 to form the optical trap. The two beam diameters are magnified specifically in order to slightly overfill

the back aperture of the OL. A photodiode (PD) is placed past the steering dichroic in order to monitor trap power while data collection takes place on the position sensing diode (PSD). The PSD is a duolateral photodiode from On-Trak. The collimating lens (CL) is a 40x air objective with NA 0.6. A halogen lamp is mounted so that its light will pass through the CL and illuminate the sample plane. A field lens (L5) projects the image plane onto the charge-coupled device (CCD) camera (C1), which collects images of trapped objects at the sample plane. C1 also records the back reflection of the laser light from the coverslip and trapped object. A dichroic (D3) allows the visible light from the lamp to reach the camera while it steers the laser light to the PSD. A lens (L6) is positioned so that the back focal plane (BFP) of the CL is projected onto the PSD, and a beam sampler (BS) and a CCD camera (C2) allow for viewing the back focal plane on a monitor. Signals from the PSD are amplified and processed by an On-Trak OT-301 position sensing amplifier with 16 kHz bandwidth. The signal is digitized by an NI-6221 DAQ card and data is acquired using LabView. Further processing of data is done using Matlab.

The sample chamber is formed with two microscope coverslips (22x22-0, Fisherbrand, Waltham, MA) separated by a 0.5 mm silicone divider and sealed with vacuum grease. It is placed on a custom-built mount which slides easily between the microscope objectives and remains aligned to a plane normal to the direction of light propagation. The mount is fixed to a three-axis stage whose motion can be controlled by three high-resolution (20 nm step size) Picomotors (New Focus, Santa Clara, CA). Before each experiment, the sample chamber is filled with Milli-Q (purified and deionized) water and a small amount of particles, such that only one

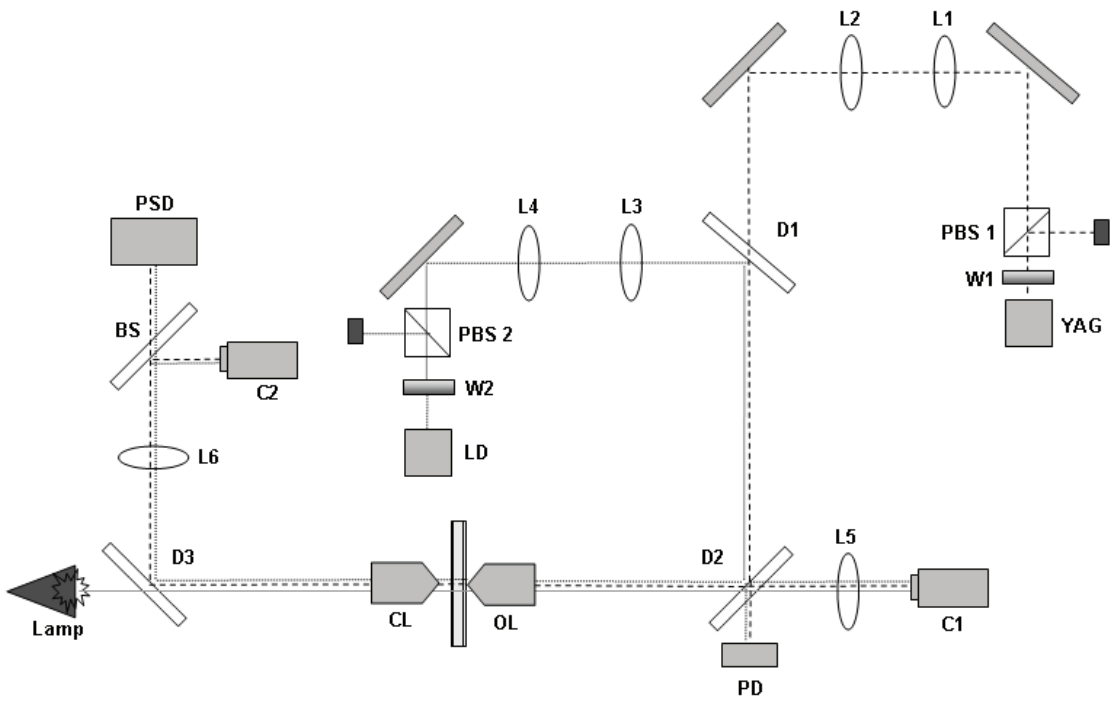

Figure 4.1: Experimental optical tweezers setup for wavelength-dependent measurements (Apparatus I). See text for detailed description.

particle will diffuse into the trap every ten minutes.

A photodiode (PD) (SM1PD1A, Thorlabs, Newton, NJ) is placed past D2 and its current is directed to a low noise current preamplifier (SR570, SRS, Sunnyvale, CA), and an oscilloscope (TDS2014, Tektronix, Beaverton, OR) for optical power tracking. The optical powers of the two lasers are set so that 80 mW of each reaches the sample plane after the power loss from the optical path and objective lens. Details of the laser power measurement technique are included in Chapter 5 of this work.

Several species of nanoshells were examined with this apparatus. Experimental

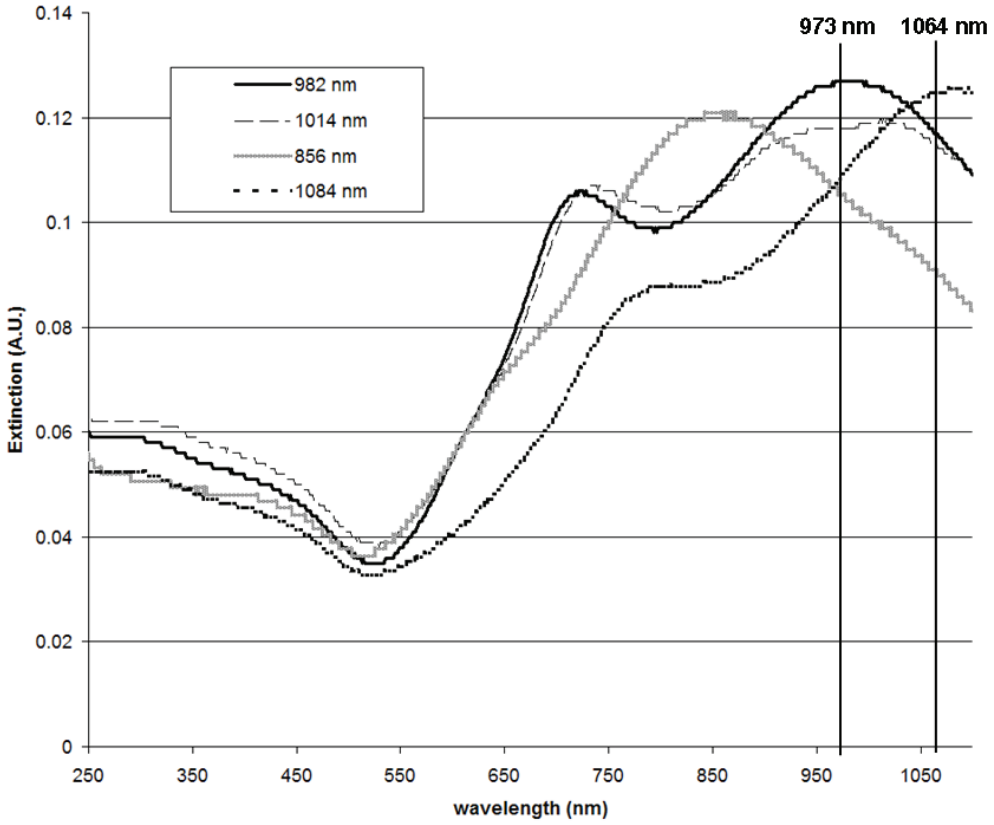

Figure 4.2: Experimental extinction spectra for the nanoshell species studied using Apparatus I. The peak locations are indicated in the legend.

extinction spectra of the nanoshells described in Figure 4.2 were measured in bulk in water with the Spectronic Genesys 5 spectrophotometer. The experimental peak resonance wavelengths are indicated in the legend. Vertical lines indicate the laser trapping wavelengths.

The data collected with this apparatus is displayed in Table 4.1. We determined that no definitive conclusions could be made based on these measurements. No real trend of behavior was evident in the data. Recall, for a system with constant viscosity, the trap stiffness is directly proportional to the corner frequency of

the power spectrum of the particle motion. Here, we assume constant viscosity and compare corner frequencies for comparisons of trap stiffness. Based on the explanations offered in Chapter 2 we expected the more blue (973 nm) laser to trap the "856 nm" nanoshells stronger than the more red (1064 nm) trap, which it does. But the more blue (973 nm) laser should trap the "1084 nm" weaker than the more red (1064 nm) laser, which it does not. (It could be possible that the increased scattering occurring for a laser near resonance are destabilizing the trap.) Furthermore, the corner frequency measured with the 973 nm trap is repeatedly about twice the corner frequency measured with the 1064 nm trap. The size and collimation of the laser beams utilized to make the measurements were therefore suspected to differ significantly, despite substantial efforts made towards ensuring their similarity. It became apparent that a tunable-wavelength trapping laser would be necessary for guaranteeing that the trap laser remained relatively unchanged for several separate trapping wavelengths.

Table 4.1: Extinction peaks, radii, and measured corner frequencies for several nanoshell species using Apparatus I.

Calculated Peak	Measured Peak	r_1	r_2	973 nm trap	1064 nm trap
756 nm	856 nm	63 nm	81 nm	267.4 Hz	173.5 Hz
938 nm	982 nm	97 nm	122 nm	495.5 Hz	237.7 Hz
932 nm	1014 nm	90 nm	107 nm	300.8 Hz	192.6 Hz
1014nm	1084 nm	96 nm	107 nm	471.0 Hz	231.1 Hz

4.2 Apparatus II: Wavelength-tunable Ti:Sapph Laser system

The second apparatus utilized for this study proved to be much more successful for taking measurements. It is comprised of optical components in a way similar to the first apparatus, but instead couples a tunable wavelength Titanium:sapphire (Ti:sapph) laser. The setup is based on a custom-built horizontal microscope and is shown in Figure 4.3. Optical components are from Thorlabs, Newport, COMAR, etc. and are mounted on two separate optical tables, each designed for vibration reduction. The beam paths remain parallel to the optical tables and their heights are minimized to reduce drift and vibration. For the trapping and detection lasers, we use either a CW TEM_{00} linearly polarized Ti:Sapph laser (900 mW at maximum wavelength, Del Mar Photonics, San Diego, CA), tunable from 730 nm to 860 nm using a birefringent crystal filter, or a CW linearly polarized diode pumped Nd:YAG laser (1064 μm, 1.5 W, OEM laser systems, East Lansing, Michigan). The system is designed such that these lasers can be used independently or concurrently. The lasers are aligned into the microscope so that their beam focuses overlap and particles may be exchanged from one trap to the other and measured in either trap. The Ti:sapph laser is fiber coupled from another optical table in order to maximize pointing stability and optimize the roundness Gaussian beam. Reflections, which cause mode-hopping and laser instabilities, are prevented from entering the Ti:sapph using an optical isolator (IO-3-800-HP, OFR, Newton, NJ). The wavelength of the Ti:sapph beam is continuously measured with a fiber spectrometer (USB2000, Ocean Optics, Dunedin, FL). The polarization of the beam is optimized

with a half-wave plate (W1) and a polarizing beamsplitter cube (PBS1). A focusing lens (FL) prepares the beam for a polarization-maintaining optical fiber (OZ optics, Ottowa, Ontario, CA) which transfers the beam from one optical breadboard (PBH1112, Thorlabs, Newton, NJ) to the other (63-530, TMC, Peabody, MA). A collimating lens (CL) (OZ optics, Ottowa, Ontario, CA) shapes the beam. A beam sampler (BS)(BSP 10-B1, Thorlabs, Newton, NJ) reflects a low percentage of light to a photodiode (PD) (SM1PD1A, Thorlabs, Newton, NJ) whose current is directed to a low noise current preamplifier (SR570, SRS, Sunnyvale, CA), and an oscilloscope (TDS2014, Tektronix, Beaverton, OR) for optical power tracking. Lenses (L1 and L2) form a telescope and amplify the beam in order to optimally overfill the back aperture of the trapping microscope objective lens. These lenses are placed so that CL is at an identical optical plane as the trapping plane, allowing for it to act as a steering mirror. A dichroic filter (D1) (XF2033, Omega Optical, Brattleboro, VT) steers the Ti:sapph beam into the oil-immersion trapping microscope objective lens (MO1) (63x, 1.4 NA, Plan Apochromat oil, 440760, Zeiss, Thornwood, NY). Another microscope objective lens (MO2) (40x, 0.6NA, 440864, LD Achroplan air, Zeiss, Thornwood, NY) collects the forward-scattered light. A Helium:Neon laser (not shown) is used to align the two microscope objectives so that they are aligned along the central axis of the microscope. After MO2, the Ti:sapph beam is reflected from a dichroic mirror (D3) (XF2033, Omega Optical, Brattleboro, VT) and a lens (L7) is placed so that the back focal plane of MO2 is projected onto a duolateral position sensing detector (PSD) (model, On-Trak Photonics, Inc., Lake Forest, CA). The linear polarization of the Nd:YAG laser is also

optimized with a half-waveplate (W2) and a polarizing beamsplitter cube (PBS2). Lenses L3 and L4 form a telescope and amplify the beam in order to optimally overfill the back aperture of MO1. Lenses L5 and L6 form a 1:1 telescope and are placed such that the mirror M1 is a steering mirror for the Nd:YAG beam. M1 is mounted on a piezo-actuated mirror mount (AG-M100N, Newport, Irvine, CA) for high resolution beam steering. A dichroic mirror (D2) (XF2016, Omega Optical, Brattleboro, VT) combines the Nd:YAG beam with the Ti:Sapph beam path. The Nd:YAG beam follows the same path as the Ti:sapph beam from there. A halogen lamp illuminates the sample placed between the microscope objective lenses and a lens (L8) acts as a field lens for projecting the trapping plane to a charge coupled device camera (CCD). The sample chamber is formed and manipulated as described above in Section 4.1. A lens (L7) is placed so that the back focal plane (BFP) of MO2 is projected onto a duolateral position sensing diode (PSD) (210LSP, On-Trak, Irvine, CA) and the forward scattered light of the trapping/detection laser by the trapped particle is incident there. Voltage signals are amplified with a voltage amplifier (OT301, On-Trak, Irvine, CA) and measured with a data acquisition card (PCI-6221, National Instruments, Austin, TX) controlled by custom-made LabView programs. The nanoshells and dielectric particles studied with this apparatus are described in detail in Chapter 3.

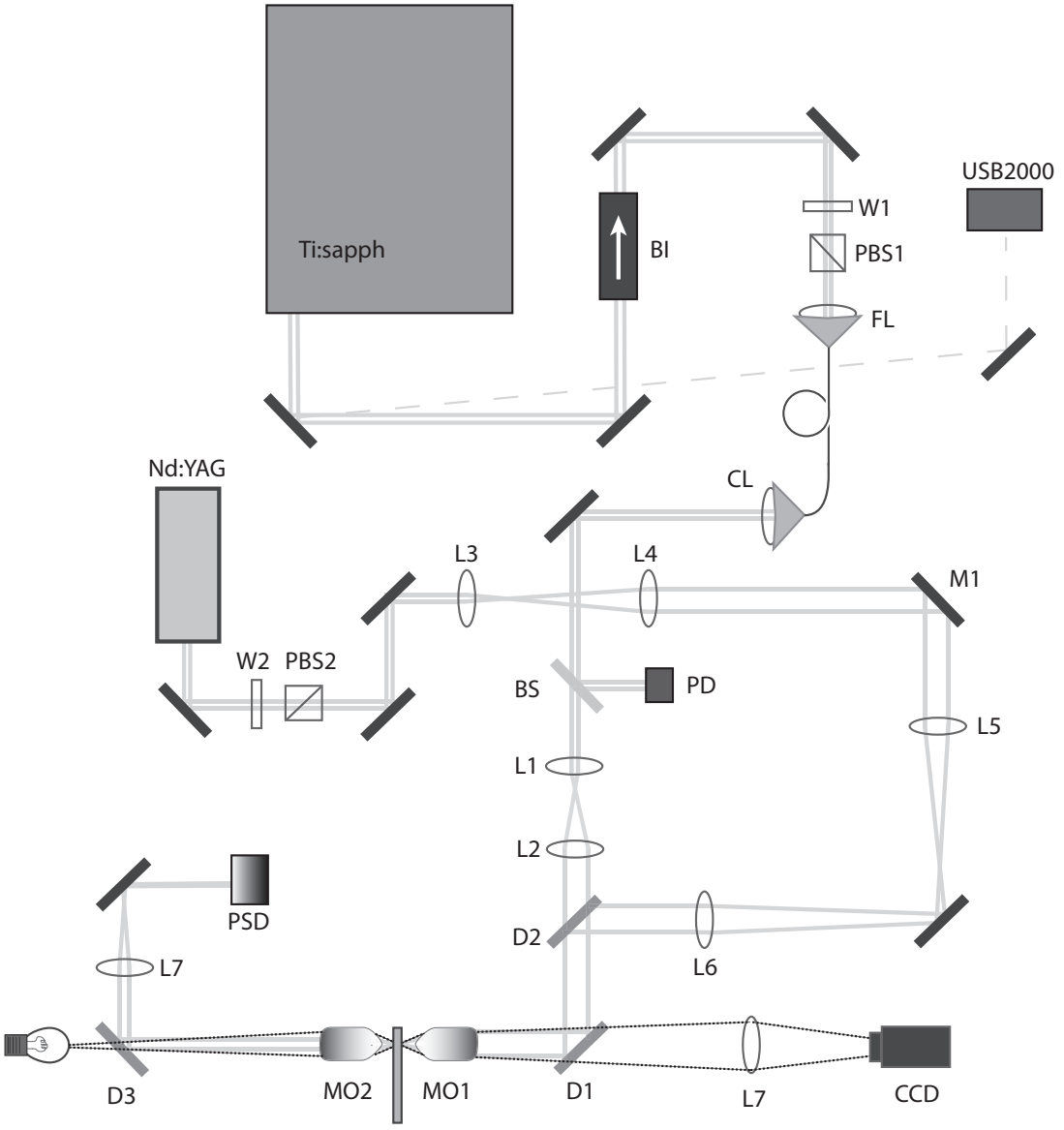

Figure 4.3: Experimental optical tweezers setup for wavelength-dependent measurements (Apparatus II). See text for detailed description.

4.3 Discussion

After the construction and testing of apparatus I, we determined that a second apparatus, apparatus II, was required for legitimate measurements of trap stiffness of a single particle as a function of wavelength. For apparatus I, the optical properties of one laser trap compared to the other differed in a number of ways such as beam size and collimation. To resolve this problem, a tunable wavelength laser was implemented into the apparatus. This allowed for trapping a particle at many different wavelengths, while relatively maintaining the size and convergence of the laser trap. A conventional commercial inverted microscope could have been used for this experiment, and is superior for experiments requiring extremely sensitive alignment (e.g., dark-field microscopy), but for our purposes, a custom-built system was more versatile and allowed for us to make changes easily as the apparatus evolved. Several techniques were developed in order to compensate for other changes to the system based on changes in trap wavelength. These are described in detail in the next chapter.

Chapter 5

Techniques for Accurate Measurements

5.1 Overview

In this work, the main experimental measurement of interest is the trap stiffness of a single particle as a function of trap wavelengths. The goal of our experiment is to measure the effect of wavelength on the trapping of both nanoshells and dielectric spheres. Therefore, much care was taken in order to ensure that varying the wavelength of the trap did not adversely affect the experiment in unwanted ways.

The trap stiffness depends on many factors including the optical power, beam diameter entering the objective lens back aperture, the refractive index of the particle and surrounding medium, the trapped particle distance from surface, and several others. Given this complexity, these factors are held constant for a single particle trapped over the entire wavelength range.

For experiments that use the corner frequency to find the trap strength, the drag coefficient γ_0 must also be determined in order to determine the trap stiffness κ. The drag coefficient is calculated based on particle size and surrounding fluid viscosity. The fluid viscosity of water changes dramatically with temperature, and the absorption coefficients of water and gold change significantly in the wavelength range used for our experiments (730 nm - 860 nm), so γ_0 must be determined at each data point.

For each individual gold nanoshell or dielectric sphere studied, the particle is trapped at one end of the wavelength spectrum, and data is collected for fifteen to twenty seconds. While keeping the particle trapped, the wavelength is tuned by 5 nm and data is then collected for the same particle. This process is repeated until data has been collected at wavelengths that span the wavelength range. In this way, we record the motion of a single particle as a function of trap wavelength, and with the following procedures, ensure that the experimental parameters across the wavelength range are constant.

5.2 Alignment of Multiple Lasers

In order to move a particle back and forth between lasers, a complete overlap of the focus of the two trapping beams was necessary. This was achieved by first trapping a microsphere (also called a "bead") with one laser and recording an image with the CCD camera. Then an identical bead was trapped with the second laser. The steering mirror for trap 2 was moved so that the the image of the trapped bead overlapped perfectly with the image of the trapped bead from the first laser. This process was repeated with smaller and smaller beads until the traps were aligned. In order to switch the bead from one trap to the other, the particle was first trapped with the Nd:YAG. Then the optical power of the Ti:Sapph was slowly ramped up until it reached its maximum, which is limited by the maximum power of the pump laser. The optical power of the Nd:YAG was then slowly decreased to 0. If sufficient alignment was achieved, then a particle would always remain in the same spatial

trapping volume throughout this process.

5.3 Optical Power Calibration at the Sample Plane

Several parameters of the system inherently vary with wavelength. One possible effect caused by changing the wavelength is the performance of the Ti:Sapph laser. As the Ti:Sapph wavelength is varied with constant laser pump power, starting from 730 nm, the maximum output power slowly increases, peaks at 790 nm, and decreases again to its minimum at 860 nm. As discussed in the previous section, it was essential to keep all parameters constant while changing wavelength, and so a scheme was developed to ensure constant laser power at the trapping plane. The photodiode (PD) in Figure 4.3 measures changes in the optical power of a pickoff reflection of the Ti:Sapph laser beam. The photodiode current is converted to voltage with a low-noise current preamplifier, which is viewed on an oscilloscope and recorded synchronously with the voltage signals from the PSD during data collection, allowing for a measure of laser power at any given time. A calibration was carried out to ensure that a measure of PD voltage corresponded accurately to a measure of optical power at the trapping plane. Knowing that the corner frequency of a trapped particle increases linearly with the trap optical power, we simultaneously measured the PD voltage and the corner frequency of a large (4.84 μm) polystyrene sphere for which optical resonance should not affect stiffness over the Ti:Sapph wavelength range (see Figure 5.1). Not surprisingly, the measured corner frequency and the measured voltage coincide in shape across the trapping wavelength range while the

maximum trap power changes, as shown in Figure 5.1, left inset. The change in the corner frequency follows the same basic path as the change in measured voltage, or essentially the change in optical power. It should follow that a constant voltage at the PD for each wavelength should result in a constant optical power level at the trapping plane. In order to verify this assumption, the optical power at the trapping plane was measured directly with an optical power meter (FieldMate, Coherent, Santa Clara, CA) while monitoring the PD voltage. The laser power was controlled by adjusting the power of the pump laser for the Ti:Sapph at each wavelength data point, such that the PD voltage remained constant. The beam after the trapping microscope objective (MO1) was collimated onto the power meter detector (placed at the output of MO1) by removing L1 from the beam path. As expected the measured optical power after MO1 remained relatively constant for constant photodiode voltage (Figure 5.1). A calibration curve was generated so that the optical power of the trap could be deduced from any measured photodiode voltage (Figure 5.1, right inset).

5.4 Pixel Size Calibration

The following five sections involve measurements or calibrations that require the knowledge of distance at the trapping plane and elsewhere. We calibrate the camera pixel size in order to have some measure of space in the x and y directions at the plane whose image is focused onto the camera. This plane coincides with the trapping plane.

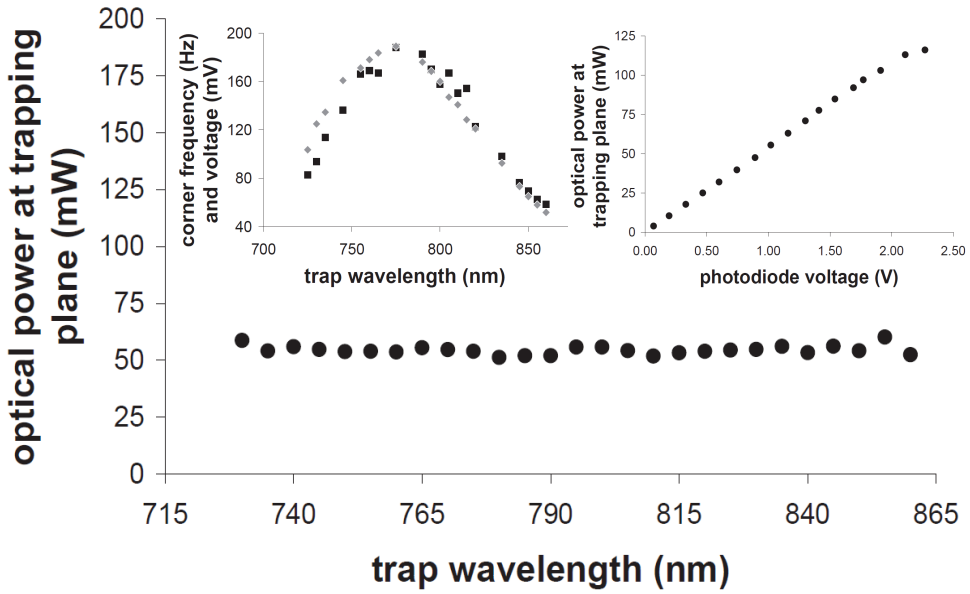

Figure 5.1: Measured optical power after the trapping microscope objective for constant voltage on the power-monitor photodiode. Inset left - Measured corner frequency of a polystyrene sphere trapped over wavelength range with maximum optical power. Black squares are the measured corner frequency of the trapped particle and grey diamonds are the measured voltages from the power tracking photodiode (PD). The power is measured after the trapping microscope objective and scaled to emphasize the similarity of curvature. Inset right - Optical power vs. photodiode voltage. The power is measured after the trapping microscope objective and used to calibrate the corresponding voltage on the photodiode.

The pixel size is measured by placing a standard ruling (Ronchi ruling, NT38-562, Edmund Optics, Barrington, NJ) in focus on the camera and recording two images of the ruling, one where the lines of the ruling are parallel to the x-axis and one where the camera has been rotated so that the lines are perpendicular to the y-axis. Such images are shown in Figure 5.2.

Image J, an image processing software package available from the National Institutes of Health, is used to measure the pixel width of the dark lines of the Ronchi ruling. The full width half maxima of the curves shown in the insets of Figure 5.2 are taken as the edges of the dark lines. The ruling has 100 pairs of dark and light lines per millimeter, allowing for the determination of pixel size. For our system, the measured pixel size in the x-direction is 103.6 $\pm$ 0.5 nm and in the y-direction is 103.0 $\pm$ 0.6 nm per pixel. From here, any displacement of a focused image at the trapping plane is measured in pixels.

5.5 Lateral Picomotor Stepsizes Calibration

Three orthogonally aligned picomotors (piezo-actuated motorized actuators, New Focus, Santa Clara, CA) control the motion of the sample stage. The axial direction in the direction of light propagation we call 'z'. The 'x' and 'y' directions are parallel and orthogonal, respectively, to the optical table in the plane perpendicular to z. The step size for the picomotors moving in the x and y directions were calibrated by measuring the distance from a focused object for a known number of steps in the x and y directions at a known stepping frequency (the step size differs

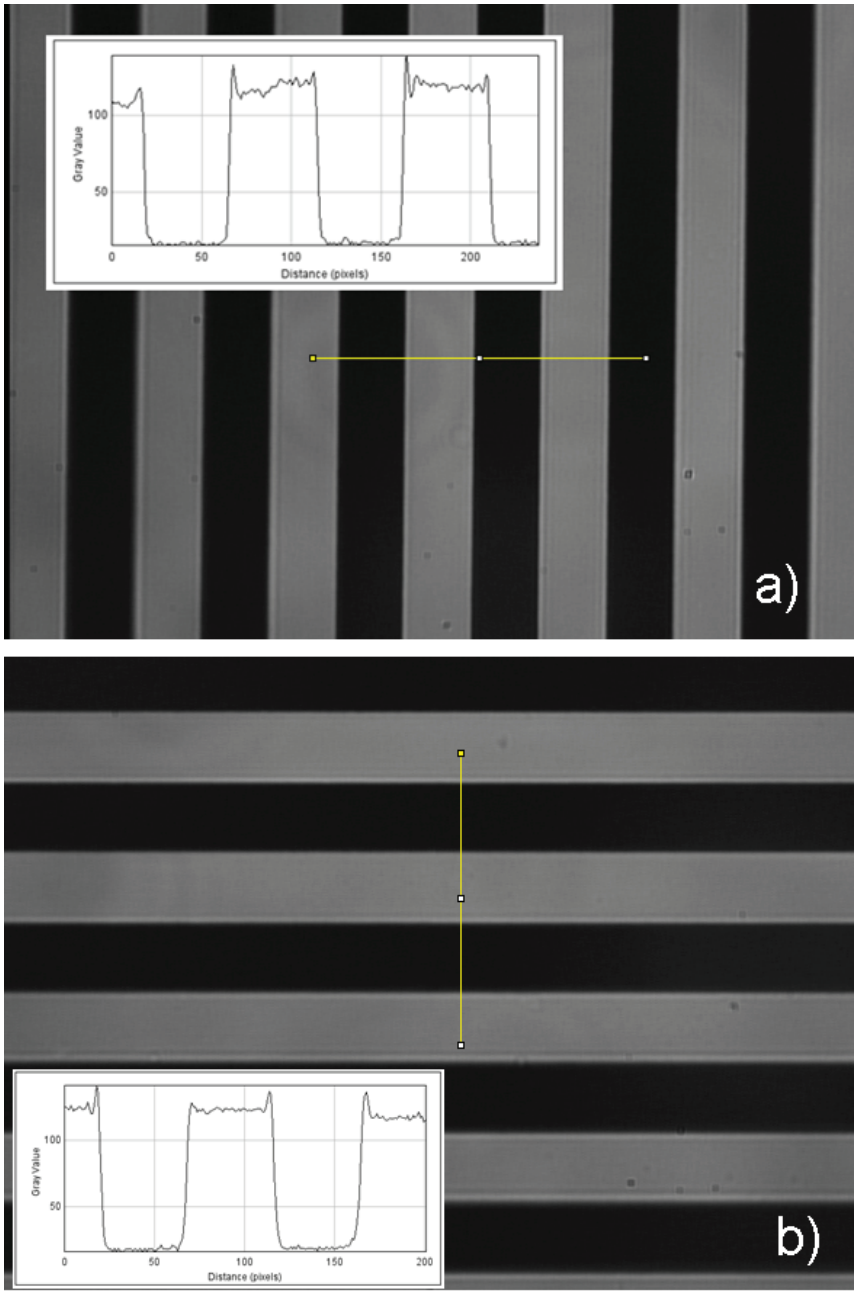

Figure 5.2: Images of a Ronchi ruling in the x (a) and y (b) directions. Insets, Image J calculations of greyscale value vs. pixel corresponding to yellow line.

for different frequencies). At 100 Hz, the step size of the x picomotor was determined to be 22.6 $\pm$ 0.4 nm per step when moving to the right on the camera, and 18.8 $\pm$ 0.3 nm per step when moving to the left on the camera. At 500 Hz the step size of the y picomotor was determined to be 17.1 $\pm$ 0.4 nm per step when moving up on the camera, and 19.7 $\pm$ 0.6 nm per step when moving down on the camera. The hysteresis is due to the change in load on the sample stage depending upon the direction of motion.

5.6 Axial Picomotor Stepsize Calibration

The picomotor responsible for axial (z) manipulation of the sample stage was also calibrated. This was achieved by trapping a polystyrene sphere with a known radius and then by slowly moving the stage (and therefore the coverslip) a noted number of steps towards the edge of the trapped sphere. The spheres used for this particular measurement stuck very easily to the coverslip, so once the bead came into contact with the glass surface, Brownian motion of the sphere would immediately stop and become unaffected by the laser trap. This position was also evident on the camera. During this axial motion of the coverslip, the position signals in the x and y directions, the sum signal, and the power spectrum of the bead were observed in real time. Based on Faxen's law [4] and the fact that the trap stiffness is dependent on Stokes' drag, the position signals and the power spectrum signal are sensitive to changes in distance between the trapped particle and the chamber surface. At the point of contact, and when the signals suddenly matched those of a stuck bead, it

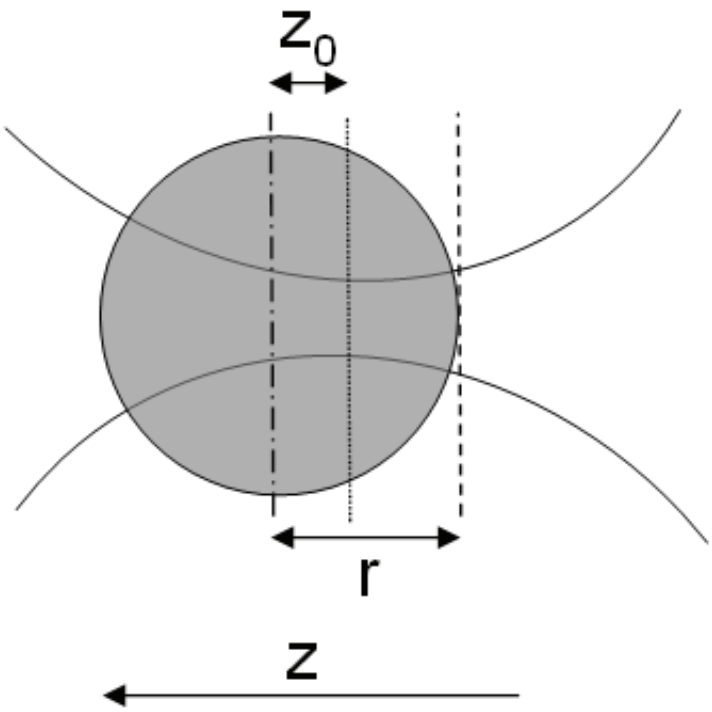

Figure 5.3: Schematic of side view of trapped bead. r is the bead radius, z is the direction of light propagation, and z_0 is the distance between the center of the bead and the trap focus.

was determined that the coverslip was touching the edge of the sphere, as shown in Figure 5.3. The sphere was then removed from the trap, and the z picomotor was moved a noted number of steps until the reflection from the coverslip was minimized in diameter, meaning the coverslip was located at the beam focus. The coverslip has now moved a known number of steps from the edge of the bead to the beam waist. The radius of the bead was known, and the distance from the beam focus to the center of the trapped sphere was determined based on techniques described in the next section. Since the scattering force of the trapping beam causes the equilibrium position of the trapped bead to be located a small distance downstream from the beam focus, the bead is slightly displaced from the focus. Hence the distance traveled by the coverslip should equal the displacement of the center of the bead from the beam focus subtracted from the radius of the bead. In this manner, the step size of the picomotor was calibrated and determined to be 8.1 nm when the picomotor moved away from the microscope objective at a frequency of 100 Hz.

5.7 Measurement of Axial Equilibrium Trapping Location

Calibration of the PSD is necessary for accurate knowledge of particle motion or displacement. At any given time, x and y voltages on the detector correspond to the x and y coordinates of an instantaneous particle location. Hence, a voltage to distance calibration must be carried out for those dimensions. This calibration is highly sensitive to the distance from the particle center to the beam focus. A correct calibration value will only be achieved if the calibration is done for a particle

located at the actual axial equilibrium position within the trapping beam. This equilibrium location will differ for each particle based on its size and material, and so the calibration must be repeated for each particle type.

The determination of the axial trapping location was carried out in the same manner as Neuman *et al* [27]. The PSD sum signal is proportional to the total incident intensity at the back focal plane of the condensor (MO2), providing a means of accurately measuring axial changes in bead location. First, the sum signal on the PSD is monitored as a bead stuck to the coverslip is moved in the direction of light propagation through the beam waist, as shown in Figure 5.4. As the bead moves through the laser focus, the phase of the scattered light changes by 180° relative to the unscattered light. This modulates the intensity distribution at the BFP of the condensor (MO2) lens. The measured intensity slowly decreases, then reaches a minimum, and increases to a maximum before decreasing and leveling off again. The intensity maximum serves as the only fiducial reference. After working with the stuck bead, an identical bead is trapped with the Ti:sapph laser and, again, the coverslip is moved from behind the focus towards the beam waist as the sum signal is monitored. Eventually, the coverslip will come into contact with the bead, the bead will stick to the coverslip, and signals identical to those collected for a stuck bead will occur. The focus and axial trapping location may both be determined from a simultaneous plot of both data sets, as shown in Figure 5.5.

The region between the major extrema (from from -3.75 μm to 0 μm) of the plot for the stuck bead is well described by the following expression for axial

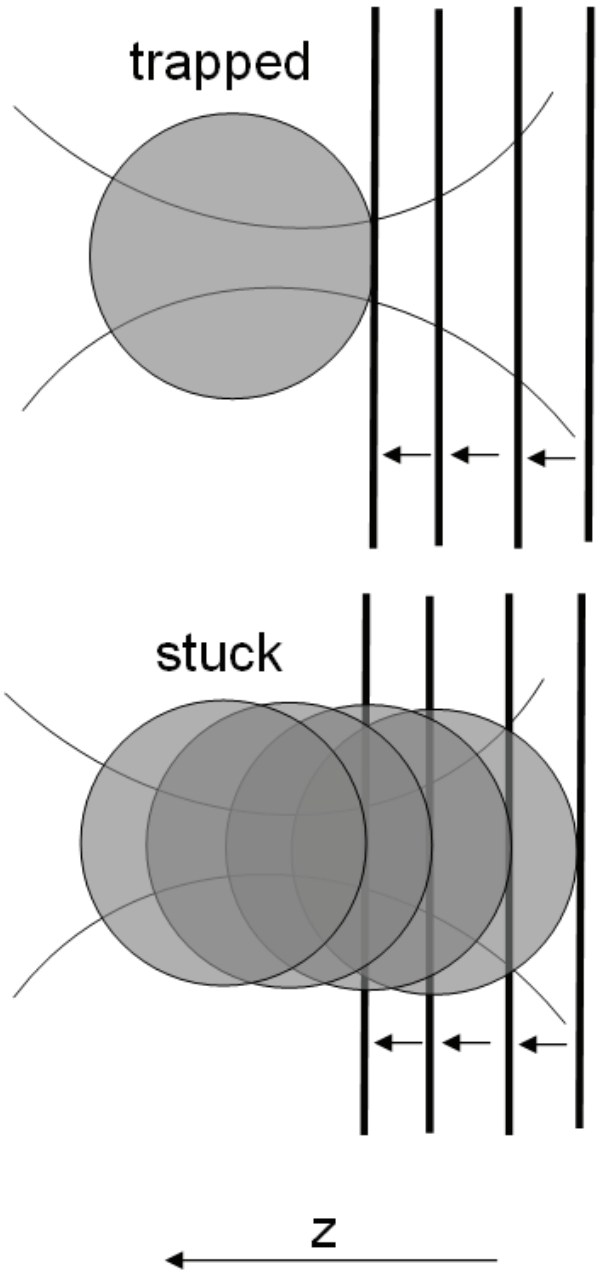

Figure 5.4: A trapped (above) and stuck (below) bead is moved through the beam focus, in small steps, in the direction of light propagation.

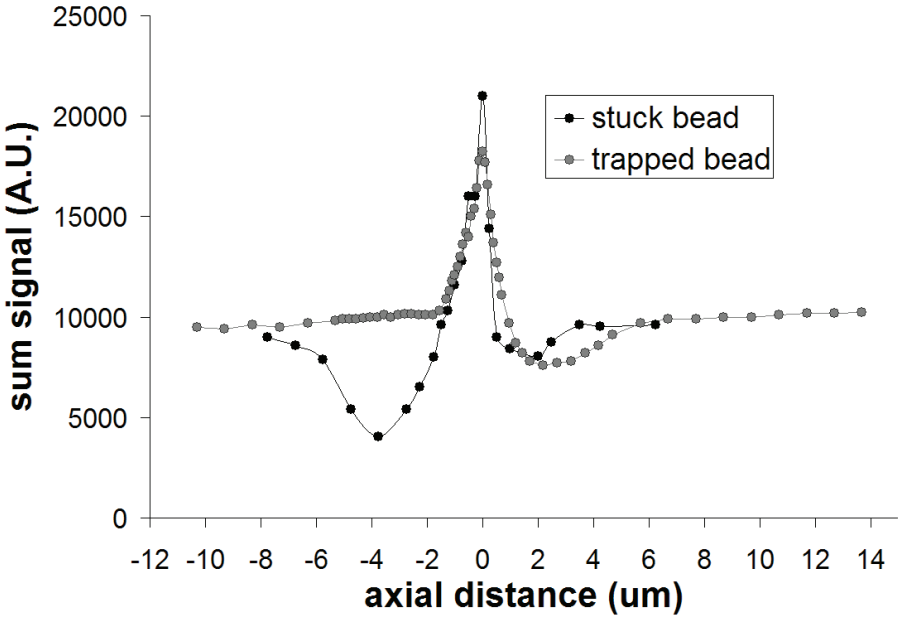

Figure 5.5: "Sum" PSD voltage for a 5.5 μm polystyrene bead stuck (black dots) and trapped (gray dots) as it is moved through the beam focus, in the direction of light propagation. The 'zero' location is arbitrarily set to where the sum signal is maximized.

sensitivity found by Pralle *et al* [68]:

$$I_z \propto \left(1 + \left(\frac{z}{z_0}\right)^2\right)^{1/2} sin[tan^{-1}(z/z_0)], \tag{5.1}$$

where z is the axial displacement from the trap center, $z_0 = \pi\ w_0/\lambda$ is the Rayleigh length, and w_0 is the beam waist diameter at wavelength λ. The focus is defined to occur at $z = 0$, which is at the point of inflection between the extrema. For the situation depicted in Figure 5.3, where $z = 0$ is reassigned to the intensity maximum reference point, the focus is located at -1.875 μm. The axial trapping location is the point of convergence in the two data sets in Figure 5.6. The two data sets converge at -1.30 μm so the axial trapping location is 0.575 μm downstream from the beam focus for this bead, the 5.5 μm polystyrene sphere described in Section 3.3. This is the experimental method for the determination of the axial equilibrium trapping location necessary for the axial picomotor stepsize calibration in the previous section. Simultaneously, this procedure allows for the determination of the axial trapping location with respect to the intensity maximum point. With this tool, we were able to place a particle stuck to a coverslip in its natural axial trapping plane for lateral detector calibrations discussed in the next section.

5.8 Lateral Direction Detector Calibration

As previously mentioned, the volt-to-meter calibration is quite sensitive to small changes in the optical detection system. An accurate calibration here is crucial for determinations of bead displacement while in the trap, and therefore for

determinations of stiffness and force. This requires moving a bead stuck to the coverslip horizontally and vertically in a plane orthogonal to the direction of light propagation through the trapping beam center and recording the voltage signals in the x and y directions. The procedure described in Section 5.7 is utilized to find the appropriate xy plane corresponding to the axial equilibrium trapping location, z_0. The bead is placed in this plane and is moved laterally through the beam focus. In practice, the coverslip is scanned laterally through the beam at small intervals, see Figure 5.6. The signal corresponding to bead motion through the exact beam center will have the highest amplitude, see Figure 5.7. Similarly, the signal corresponding to motion in the perpendicular direction will have the lowest amplitude in that direction. The process is performed twice so that the bead moves through the beam in one direction, say from right to left, and then in the opposite direction, from left to right. The percent difference of the absolute value of the slope (Volts per meter) for each direction is the error associated with this measurement. This value did not exceed 2.3% and so is not included in error estimates for stiffness determinations in Chapter 7.

5.9 Axial Shift of Focus and Spherical Aberrations

Measurements of trap stiffness are dependent on multiple factors, one very important factor being the distance from the coverslip to the trapped particle or beam focus. If this parameter is not held constant for a data set, it could affect trap stiffness in two ways. First, spherical aberrations in the Gaussian profile of

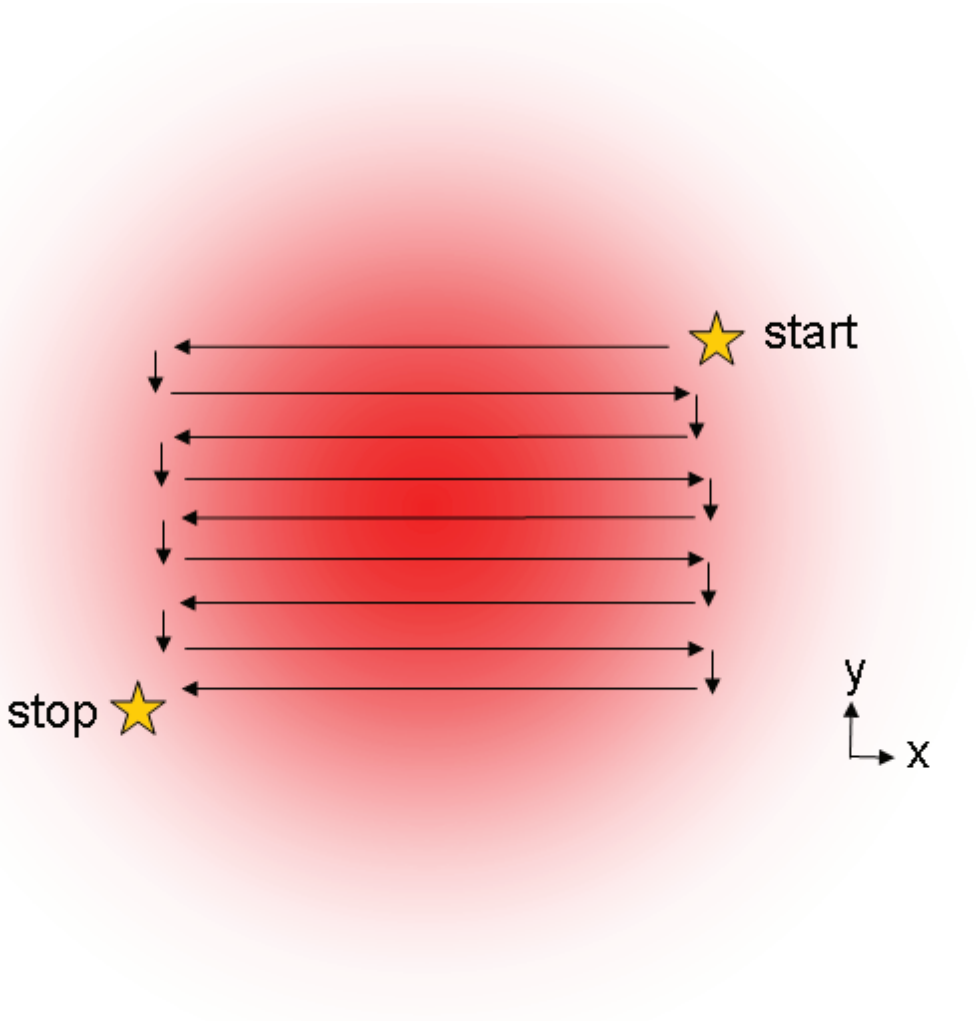

Figure 5.6: Path of stuck bead during a lateral scan in the xy plane at the equilibrium trapping location

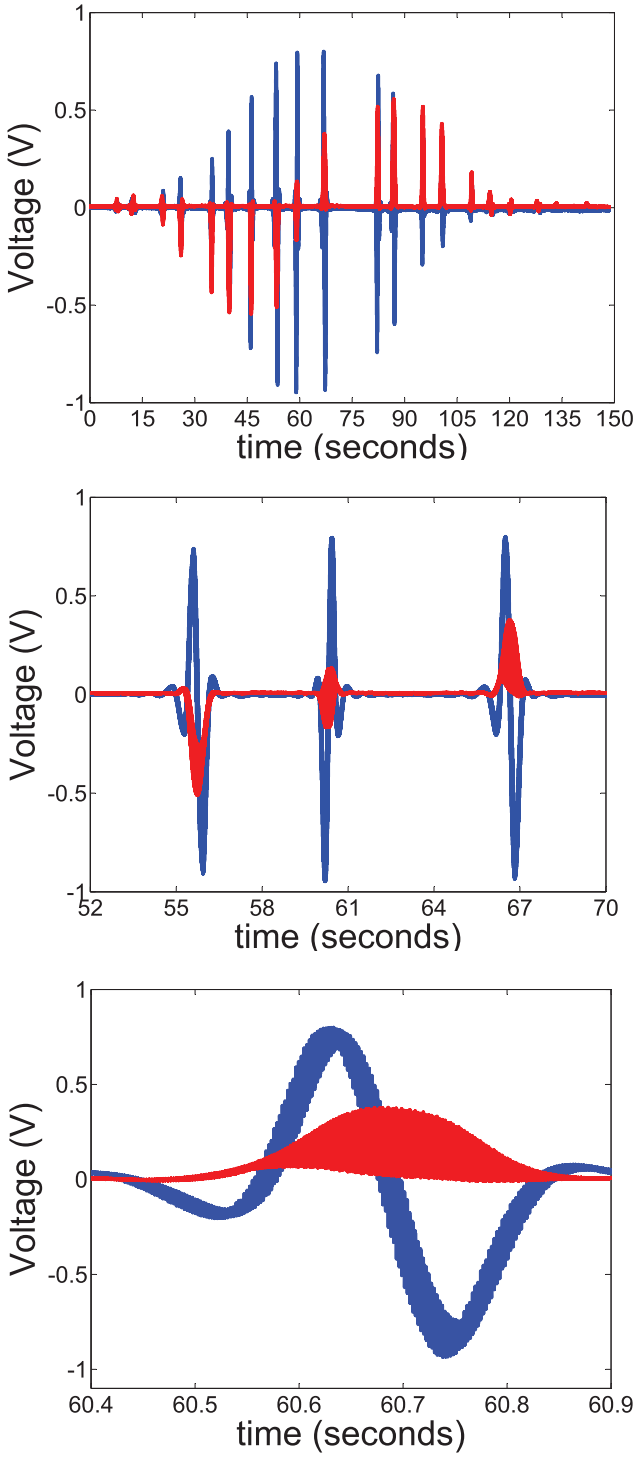

Figure 5.7: Detector signals for a bead moving in the xy plane through the beam focus, an example of which is shown in Figure 5.4. Blue is the x-direction and red is the y-direction. All three images are for the same data set, the two lower figures are for smaller time intervals. The "noise" evident in the signal is due to the picomotor step action.

the trapping laser beam can increase or decrease with changes in distance from the coverslip to the beam focus, based on the index of refraction of the immersion liquid, of the coverslip glass, and of the fluid inside the sample chamber [69]. Second, for a particle whose radius is comparable to the distance from its center to the coverglass surface, a quantity we call ξ, large changes in the viscous drag can occur. We avoid this complication by keeping ξ at least four times the bead radius. Still, we felt it prudent to measure if the distance between the coverslip and trap focus changed significantly in the axial direction over our wavelength range.

With the axial picomotor step size calibration described in Section 5.6, the axial beam focus shift was measured in the following manner. Using the Ti:Sapph laser, and with a variable neutral density optical filter, the CCD camera recorded an image of the back reflection of the trap light at 860 nm. The trap light was then scanned to the other end of the spectrum at 730 nm and the optical power incident upon the CCD camera was adjusted to be the same as at 860 nm. The axial direction picomotor was then used to move the coverslip until the diameter of the back reflection of the trap at 860 nm was realized. The number of steps was noted, and the distance traveled was calculated to be 400 nm, meaning that over the entire wavelength range, the beam focus shifts 400 nm further away from or closer to the edge of the sample chamber. The average distance from the coverslip to the trapped bead for all the experiments we performed is 5 μm. We reason that a change in this quantity of plus or minus 400 nm is negligible and should not significantly affect trap stiffness measurements.

In order to test the effects of spherical aberration from changes in ξ, we trapped

single particles and measured the corner frequency at several values of ξ. For a single trapped nanoshell, the corner frequency typically decreases by a factor of two when ξ increases by 10 μm. For a single trapped polystyrene sphere (0.94 um in diameter) the corner frequency increases by a factor of 1.6 with an increase in ξ by 9 μm. How spherical aberrations affect the trapping forces is highly dependent on both particle size and ξ, hence the discrepancy in trends for the two particles. At any rate, for a small change in ξ, small changes in corner frequencies are expected. Based on the measurements described here, such a change in ξ (400 nm) should not contribute to more than a 10% increase or decrease in the corner frequency.

5.10 Beam Size Parameter Changes with Wavelength

In order to minimize the effects of chromatic aberration, all lenses used in the experiment were achromats. Changing the wavelength from one end of the Ti:sapph spectrum to the other did not affect the fiber coupling efficiency. Still, we felt it pertinent to determine the effects of chromatic aberration over the wavelength range. The beam diameter was measured at the entrance to the trapping objective lens and at a second location 20 cm further "downstream" with the dichroic mirror D1 removed. In both cases, the beam diameter increased in size by 5% from 730nm to 860 nm, a negligible value.

We also calculated and measured the beam waist size at different wavelengths after the objective lens. Changes in the beam waist were measured by moving the sample stage in the axial direction so that the beam focus is at the inner face of

the coverslip. The reflection of the focused beam was attenuated to a constant power with a variable neutral density optical filter and was imaged on the CCD camera. Images were collected at each trapping wavelength and compared in order to determine changes in the beam waist size. With this technique, the measured beam waist size for 730 nm trap light was 824 nm and for 850 nm light was 720 nm, for a difference of 12%. Although this measurement technique gives the beam waist when the beam is focused on the coverslip and not at the actual trapping plane, we expect that the changes in the beam waist over the wavelength range will not differ greatly at the two axial focal positions.

Calculations of the beam waist were performed with PSF Lab, a software package available from the One molecule group at the University of Wisconsin, Madison [70]. The following parameters were used for this calculation. The index of refraction of the immersion oil, coverslip glass, and sample chamber fluid (water) were $n_1 = 1.518$, $n_2 = 1.5$, and $n_3 = 1.33$, respectively. The numerical aperture of the microscope objective was 1.4. Incident light was assumed to be linearly polarized in the x-direction. The microscope objective is designed for a coverslip thickness of 170 μm but a 100 μm thick coverslip is used in practice. The beam waist is located at the inner face of the coverslip (depth = 0) for an accurate comparison to the measured values above. The calculated beam waist for 730 nm light (Figure 5.8) was 861 nm and for 850 nm light (Figure 5.9) was 784 nm, for a difference of 8.9%. We believe that the 10% difference in beam waist size should not affect the optical trapping forces significantly, and even if it did, detector calibration at each trapping wavelength should eliminate this effect.

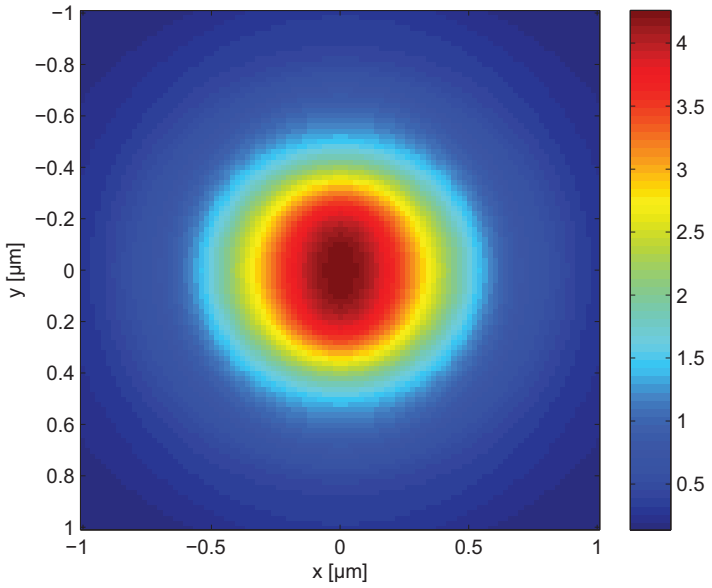

Figure 5.8: Calculated point spread function for beam waist for the experimental parameters of our system. The trapping beam wavelength is 730 nm.

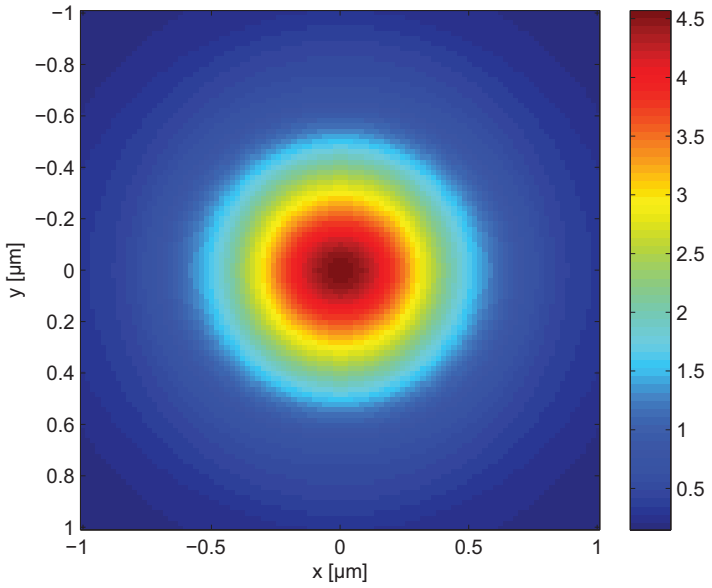

Figure 5.9: Calculated point spread function for beam waist for the experimental parameters of our system. The trapping beam wavelength is 850 nm.

Curiously, for both the measured and calculated values, the beam waist decreases in size with an increase in wavelength. This trend opposes that predicted by a general knowledge of chromatic aberration. In general, the beam should focus more tightly for smaller wavelengths. This does occur when the beam waist size is calculated with PSF Lab over a larger range (from 300 nm to 900 nm). For this particular system, the effects of the nonideal parameters such as mismatched indices of refraction and incorrect coverslip size cause unexpected light focusing in the 730 nm - 860 nm laser wavelength range. Even so, the trap changes only by ten percent within this range - a sufficiently small value allowing us to consider the trap as "constant" in size.

5.11 Single or Multiple Particle Trapping

Only one particle is trapped at any one time during data collection. Although the polystyrene and silica spheres are easily imaged, the nanoparticles are not visible in the light microscope, so a different method is required for ensuring that only one particle is in the optical trap during measurements. When comparing the voltage signals on the PSD and statistical data for a single trapped nanoparticle to multiple trapped nanoparticles, significant differences are apparent. The variance of the voltage signals increases as more and more particles diffuse into the trap. The position histogram remains Gaussian but widens and its peak lowers with the number of trapped particles [71]. Due to an optical binding effect that occurs for the metallic plasmonic particles, the power spectrum corner frequency increases when

two metallic nanoparticles are trapped in comparison to a single trapped particle, and in addition, the standard deviation of the voltage signal increases step-wise in amplitude and variance with trapped particle number [72]. We compared the signals several times for several nanoshell species and determined a minimum voltage signal variance, standard deviation, and corner frequency for these particles. We assumed that these minimal signals correspond to the trapping of a single gold nanoshell. During data analysis, we compare these characteristic signals to the data in question to ensure that only one particle was trapped for each data set. Images of larger particles (0.3 μm and higher) are quite visible in the light microscope and therefore multiple particle trapping is simple to detect. In addition, the effect of trapping multiple spheres on the detection signals is quite pronounced. Voltage signal variances increase by a factor of about two, and the corner frequency of the power spectrum will generally reduce by half when trapping two large dielectric particles as compared to one [73]. Hence, we carefully monitor the voltage and power spectrum signals during data collection, and compare the signals to those for one bead, in order to ensure that only one particle is in the trap at a time. More detail on this procedure is included in Chapter 8 of this work.

In addition to this rigorous technique for trapped-particle-number determination, we also view the backscattered light from a trapped nanoshell using a CCD camera, as shown in Figure 5.10. When a trapped nanoshell is not present, only the dim ring pattern of light is visible due to trap light reflections from the coverslip. When a nanoshell is present in the trap, it scatters enough light to the camera to form a bright spot at the center. Nanoshells moving near the trap or entering the

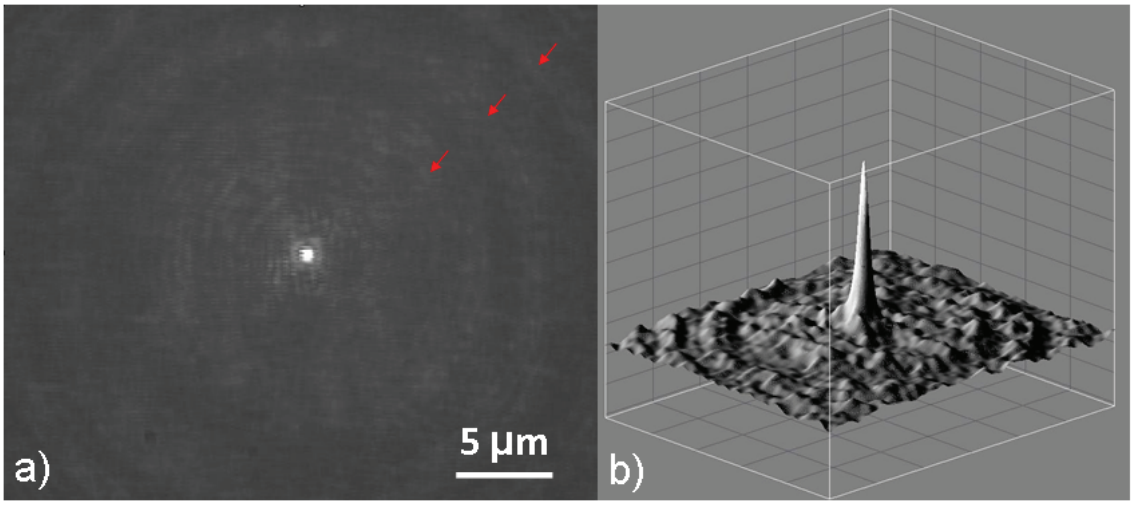

Figure 5.10: a) Backscattered light from a trapped nanoshell and b) three dimensional intensity profile of the picture in a). Arrows indicate the dim ring pattern of light reflected from the coverslip surface to the camera.

trap are visible as well, giving us a rough indicator that an additional nanoshell may have entered the trap. Figure 5.10(b) is a three dimensional surface plot of the light intensity over the two dimensional area of Figure 5.10(a).

5.12 Discussion

An optical tweezer system used for measurements of position must be carefully calibrated in order to achieve accurate results. For our system, a series of calibrations were carried out. This included determinations of optical power at the sample plane, pixel size, average stepsize for each picomotor, location of axial trapping equilibrium position, and voltage-to-distance factors for the x and y directions on the PSD.

As the wavelength of our trapping laser is changed, several other system char-

acteristics change. We take extra care to ensure that these system characteristics change in small ways in order to prevent their affecting measurements of trap stiffness.

Trapping of more than one particle will change voltage signals significantly, and affect the accuracy of measurements. So we also ensure that only one particle is trapped in the laser during data collection.

Chapter 6

Temperature and Viscosity Effects

6.1 Overview

In order to quantitatively measure the trap strength with respect to the extinction resonance, we record the position signals of a trapped nanoshell by collecting the forward scattered light on the duolateral PSD. Analysis is performed to find the corner frequency of the power spectrum from the position time trace for a single trapped nanoshell. To measure the corner frequency, we first trap a nanoshell at one end of the trapping wavelength range (either 730 nm or 860 nm), and then track the nanoshell motion in time. This is repeated in steps of $\Delta\lambda = 5$ nm until the end of the laser tuning range is reached. In this way, we achieve a measure of corner frequency as a function of wavelength. To correctly interpret the results, it is necessary to determine the trap strength of the system from the corner frequency using Equation 2.9. Here, the drag coefficient γ_0 is dependent upon viscosity η of the fluid surrounding the trapped particle, which is highly sensitive to changes in temperature. Nanoshells are designed to heat significantly when illuminated with light near their optical resonance, and so we expect considerable heating to occur for the trapped nanoshells in our experiments. It is critical to determine how this heating differs from one trapping wavelength to another if we are to correctly determine the trap stiffness. Therefore, it was necessary to determine the temperature

of the trapped nanoshell at each trapping wavelength.

6.2 History of Temperature and Viscosity Measurements in Optical Trapping

While several methods have been developed for the determination or control of temperature in an optical trap, most of them require sophisticated optical setups or complex chemical systems [74]. Methods developed by Mao *et al* [75] require an additional laser for localized heating of water or require temperature-controlled fluid to be pumped through the trapping microchamber. Bendix *et al* [76] embedded metallic nanoparticles within a lipid bilayer and incorporated a dye whose fluorescence was temperature calibrated. Another method for temperature measurement requires the construction of a specialized interferometer, which detects differences in index of refraction of the fluid in the optical trap due to temperature gradients [74]. Each technique requires extensive additional equipment and properly carried out methods for successful measurements or control. We, instead, utilized a temperature measurement technique, which required no additional equipment, based on methods developed by Peterman *et al* [77] and Abbondanzieri *et al* [78]. We also performed calculations of temperature for trapped nanoshells, which are described in detail in Section 6.4.

6.3 Shortcomings of Assuming Constant Temperature and Viscosity

The temperature of a trapped object is frequently assumed in optical tweezers experiments to be the same as that of the surrounding fluid, which is typically at room temperature or at some other controlled temperature. For optical tweezer experiments utilizing nonabsorbing particles with laser powers lower than 100 mW, the heating of water surrounding the particle is negligible [77]. However, optically trapped metallic nanoparticles have been shown to heat substantially [30, 76, 79, 80]. We utilized two criteria for determining whether or not such heating occurred for our nanoshells: a comparison of high-frequency power spectra [77] and a comparison of the trap stiffness determined with both the power spectrum method and the equipartition method [30]. In Equation 2.7, the f_c^2 term is negligible for high frequencies, causing the remaining expression to become independent of trap stiffness and therefore corner frequency, yet still dependent on temperature. Therefore, if the temperature were to remain constant over the wavelength trapping range we would expect the power spectra of a nanoshell at different wavelengths to overlap at high frequencies.

Figure 6.1 displays the fitted and raw experimental power spectra of a nanoshell trapped at several trapping wavelengths with a constant 40 mW trapping power. In the high frequency region, the spectra do not overlap, showing that the temperature is changing with trap wavelength.

Another method of verifying temperature change is by comparing the trap stiffness determined by power spectral analysis (Equation 2.9) to the trap stiffness deter-

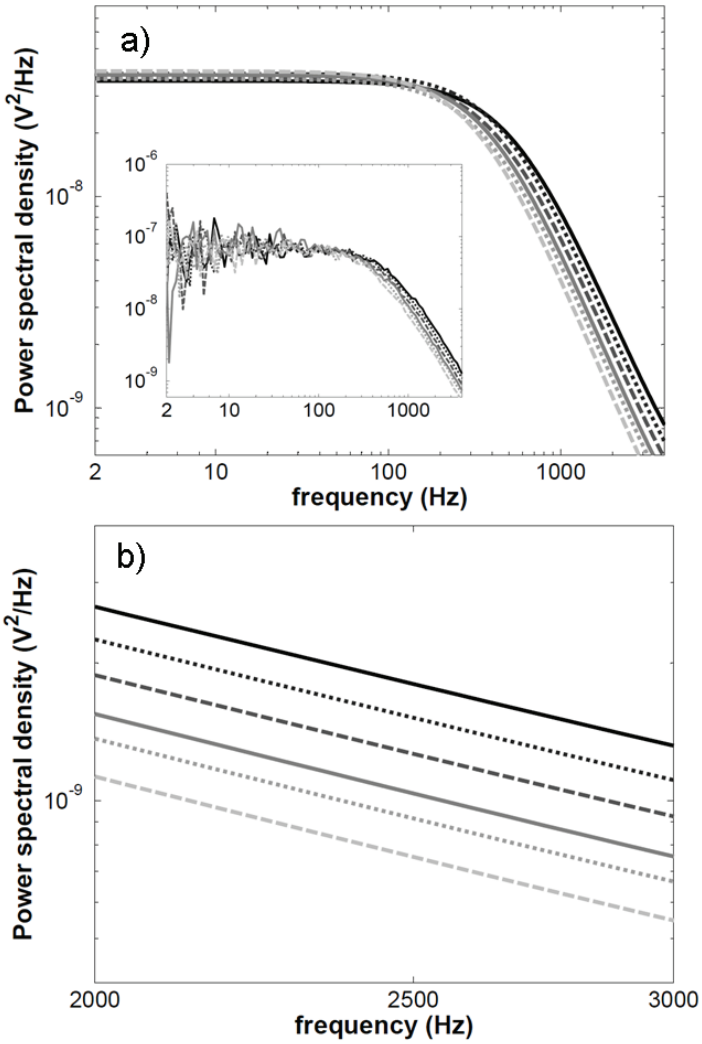

Figure 6.1: a) Lorentzian fits of power spectra for a nanoshell with scattering resonance at 940 nm. Inset shows the raw experimental power spectra. b) High frequency region of a). If temperature was constant, the power spectra would overlap at high frequencies. Trapping wavelengths are: black line - 740 nm, black dots - 760 nm, grey dashes - 780 nm, grey line - 800 nm, light grey dots - 820 nm, light grey dashes - 840 nm.

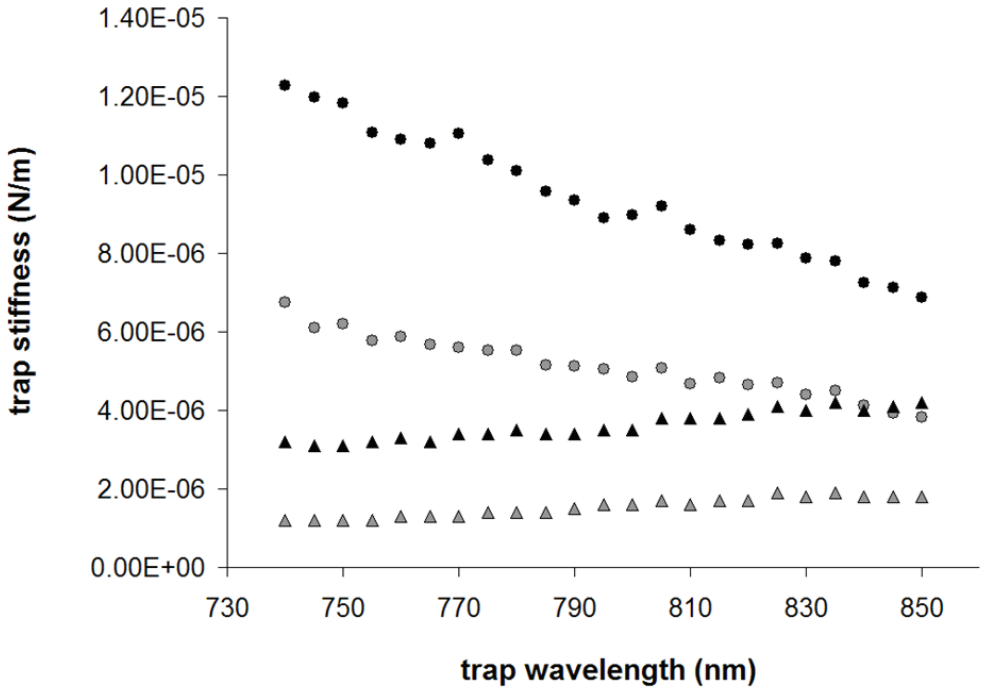

Figure 6.2: Trap stiffness if constant temperature is assumed for the nanoshell in Figure 6.1 determined with the power spectrum method (κ_{eq}) (dots) and the equipartition method (κ_{ps}) (triangles). Black is for data in the y-direction and gray is for data in the x-direction. The divergence of κ_{eq} and κ_{ps} shows that the temperature is not constant, but changes with the trap wavelength.

mined by the equipartition theorem (Equation 2.10), which states $\kappa_{eq} = k_B T/\langle x^2 \rangle$, where x is the position of the particle. Because κ_{eq} explicitly depends on temperature and κ_{ps} implicitly depends on temperature via viscosity, a comparison of the two should demonstrate temperature effects. If the temperature is incorrectly assumed to be constant over the trapping wavelength range, κ_{eq} and κ_{ps} should diverge.

Figure 6.2, where temperature is assumed to be constant at room temperature, shows exactly this. For both measurement directions, we found that the stiffnesses

determined by the two methods diverge as the trapping wavelength changes, implying that the temperature is changing over the trapping wavelength range. In order to accurately calculate the trap stiffness, a correct measurement of the temperature is essential and should result in convergence of the values of κ_{ps} and κ_{eq} over the entire trapping wavelength range.

6.4 Temperature and Viscosity Calculations

Trap stiffness depends linearly on viscosity, η, of the fluid surrounding the trapped particle, where $\kappa_{ps} = 12\pi^2 r\eta f_c$. The fluid viscosity of water is highly temperature dependent [81]. The absorption of gold nanoshells changes with wavelength, and so the surface temperature of a nanoshell should also change with wavelength, affecting the local water viscosity. Additionally, the absorption of water changes with wavelength, affecting the temperature of the water within the trapping volume. The temperature and viscosity of water 100 nm from the surface of a nanoshell was calculated based on methods developed by Seol *et al* [30] and are displayed in Figure 6.3. We consider a gold shell trapped in a Gaussian beam, absorbing light and conducting heat into the water surrounding it. For a steady state with room temperature T_∞, C equal to the conductivity of water (0.6 W/Km), and where r is the distance from the center of the sphere, the temperature around the shell is

$$T(r) = T_\infty + \frac{P_{abs}}{4\pi r C} \tag{6.1}$$

where

$$P_{abs} = \sigma_{abs} I(z). \tag{6.2}$$

The particle will be trapped at an axial equilibrium position, z_0, whose location is somewhat past the beam focus, where the intensity is:

$$I(z) = \frac{P}{\pi \omega^2(z)} \tag{6.3}$$

and the beam waist is that of a typical focused Gaussian,

$$\omega(z) = \omega_0 \left(1 + \left(\frac{z}{z_0}\right)^2\right)^{1/2}. \tag{6.4}$$

We determined the beam waist, ω_0, and the axial equilibrium location, z_0, as described in sections 5.10 and 5.7, respectively. The absorption cross section of a Rayleigh particle is:

$$\sigma_{abs} = \frac{2\pi n_m}{\lambda} Im\left(3V \frac{\epsilon_g - \epsilon_w}{\epsilon_g + 2\epsilon_w}\right) \tag{6.5}$$

where ϵ_g is the complex electric permittivity of gold, ϵ_w is the complex electric permittivity of water, λ is the trap wavelength in vacuum, and $n_m = 1.33$ is the index of refraction of water. The volume of gold, V, is that for a gold shell with the dimensions of the gold nanoshell in question. The skin depth of gold is always larger than the gold thickness of a nanoshell, so no inferred volume attenuation is included. With equation 6.1, the temperature surrounding a nanoshell is found at a certain distance r from the center of the nanoshell, for a range of trapping wavelengths.

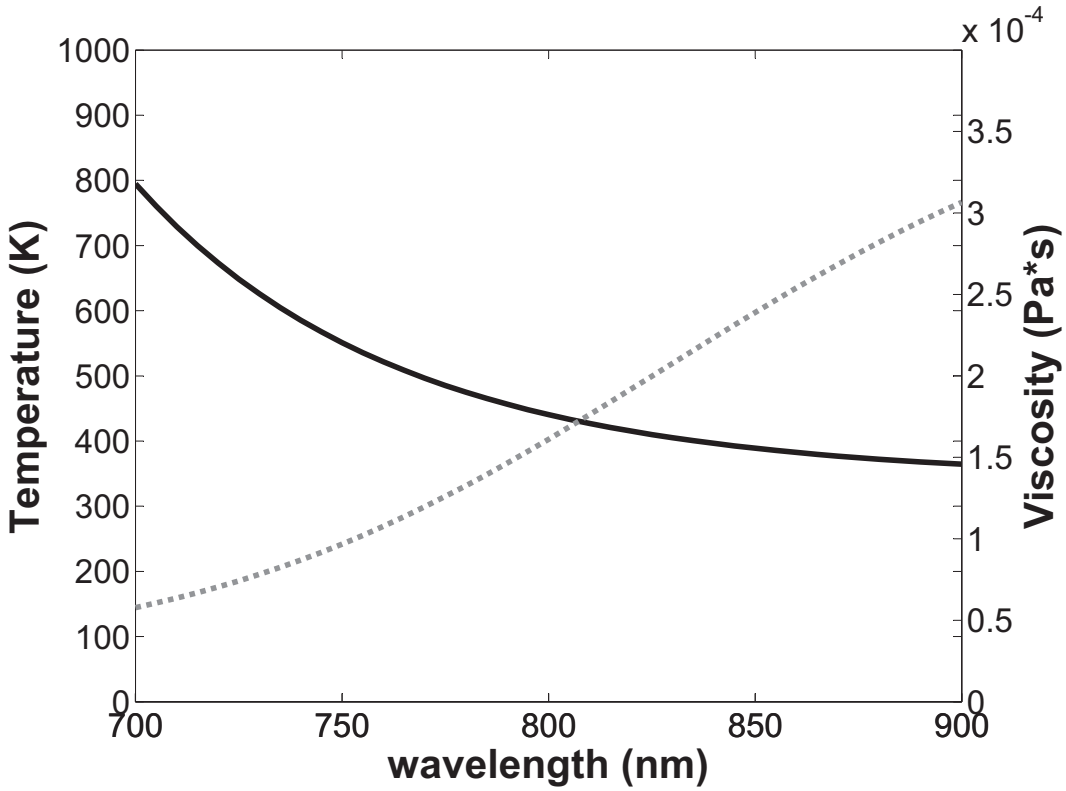

Figure 6.3: Temperature and viscosity of water surrounding a trapped nanoshell, calculated 100 nm from the surface. See text for details.

Figure 6.3 shows the results of the temperature calculation for a nanoshell with r_1 = 90 nm and r_2 = 108 nm and optical power P = 50 mW. The temperature is found for r = 100 nm from the surface of the nanoshell. The resulting temperature-dependent viscosity of the particle, η, is found using the correlation used by Laliberté [81]:

$$\eta(T) = \frac{T + 246}{(0.05594T + 5.2842)T + 137.37} \tag{6.6}$$

where η is in units of mPa×sec and T is in units of C.

The calculated temperature at this distance from the surface seems quite high,

and in fact would be high enough to cause boiling of water surrounding the nanoshell. However, while boiling was observed for clusters of nanoshells fixed on a coverslip, it never occurred for nanoshells confined to the optical trap. For boiling to occur, a small seed must exist in order to nucleate a bubble that exceeds surface tension forces, which scale inversely with the particle radius. Such a bubble will occur at a substantially increased temperature compared to that of the boiling point of bulk water, yet below the critical point of 641 K. So we can assume that the nanoshells in motion in the optical trap heat significantly, but at equilibrium, maintain a cool enough temperature such that the water surrounding them remains in the liquid state. Fixed clusters of nanoshells, similar to those utilized in tumor ablation, would exhibit a temperature high enough to boil water, at least when irradiated with light similar to that used in our experiments.

Whether or not the magnitude of the temperature is accurate in this calculation, we can infer that a general trend exists for the change in temperature of the gold nanoshell with respect to trap wavelength. The temperature increases as the trap wavelength decreases, owing to the increased absorption of gold (and also a slight increase in the absorption of water) in that direction. This, in turn, causes a decreasing viscosity as wavelength decreases. This important factor must be included in any determination of experimental trap stiffness.

Our temperature calculation neglects some cooling effects (such as convection currents) which may carry heated liquid away from the particle. Also contributing to a possibly incorrect determination of absorbed power is the absorption cross section. For the calculation here, σ_{abs} is assumed to be that of a gold Rayleigh

particle instead of that of a gold nanoshell.

It should be mentioned that the equilibration time for temperature is much faster than the motion of the trapped particle. The Brownian motion time scale is the inverse corner frequency, which for the particles trapped here is on average 500 Hz, giving a motion time scale of 0.033 seconds. Knowing the conductivity of water (C = 0.6 J/s/K/m) and the heat capacity per volume of water (c_v = 4.2 x 10^6 J/m^3/K), the equilibration time to a given radius r can be estimated from the ratio of the heat capacity to the heat conduction and so will be proportional to $r^2 c_v/C$. This value is 3 x 10^{-7} seconds for a radius of 200 nm. Clearly the particle will reach temperature equilibrium faster than it will move, meaning that cooling due to motion should not contribute. Additionally, the average distance a trapped nanoshell will move while in the optical trap is 10 nm, meaning the particle does not experience large changes in optical power absorption since the beam waist radius is on average 500 nm. Therefore, any cooling due to the particle moving out of the Gaussian focus would also not contribute.

After further reflection on the contributions of absorption, we realize the calculated absorbed power is overestimated. If we consider a calculated temperature of 800 K (at the surface) for 800 nm light for a particle with radius 100 nm, the absorbed power must be 0.38 mW. Since the beam diameter at the trap location is about 1 μm, the ratio of the geometric cross section of the nanoshell to the beam cross section is about 1/25. Hence for a 50 mW incident beam, about 2 mW is intercepted by the trapped particle. Then the ratio of power absorbed by the nanoshell to intercepted power is 19%. Fresnel reflection due to the index mismatch will result

in most of the light being reflected. Bulk gold at 800 nm will reflect about 97.5% of the light, so only about 2.5% of the intercepted light is available to be absorbed. For the 2 mW intercepted by the nanoshell, this corresponds to about 0.05 mW to be absorbed. The attenuation length of gold at 800 nm is about 80 μm^{-1}, meaning the absorption cross section is quite high, so most of this power may be absorbed. This absorbed power (0.05 mW) is about a factor of 10 less than the estimated absorbed power to heat the water by 500 K (0.38 mW), so the temperature would instead rise by only about 50 K. This temperature rise is much more realistic and consistent with our observations: we never observed boiling for a trapped nanoshell.

Due to the imperfections in our calculation of heating, we found it important to perform measurements of nanoshell temperature. The measurement process is described in the next section.

6.5 Temperature Measurements

As described earlier, a close inspection of the high-frequency region of the power spectra of a trapped particle will reveal the effects of a wavelength-dependent change in temperature (Figure 6.1). If the temperature were to remain constant for a single particle trapped at several wavelengths, then the spectra should overlap for high frequencies. We see, however, that significant spacing is present for the high-frequency part of the power spectra of a nanoshell trapped over the wavelength range, indicating a considerable change in temperature as the trapping wavelength is changed.

To measure the temperature change, we utilize a technique that required no additional equipment, based on the temperature-dependent viscosity in Equation 6.6, and on methods developed by Peterman *et al* [77] and Abbondanzieri *et al* [78]. At high frequencies (where $f > 100 \times f_c$), the corner frequency becomes negligible, and Equation 2.7 becomes independent of trap stiffness:

$$\lim_{f_c<500Hz} P_k(f) = \frac{k_B T}{3\pi^3 \eta(T) d f^2} \tag{6.7}$$

where d is the particle diameter. However, it remains dependent on viscosity and temperature. With a calibrated detector giving a conversion from volts to meters, the only remaining unknown for Equation 6.7 is temperature. So for a single trapped particle, power spectra were measured at each trapping wavelength in the wavelength range, and each was fit with a Lorentzian. Temperature was then deduced using Equation 6.7 to find P_k(f) in the high-frequency region with data collected for a calibrated (volts to meters) detector. Detector calibrations were performed as described in Chapter 5. In order to eliminate the inherent change in trap size when the wavelength is changed, the detector was calibrated at each trapping wavelength for each nanoshell species.

We verified the accuracy of the temperature measurement by comparing trap stiffness determined by the power spectrum method and the equipartition method. With these two methods, the measured temperature of the nanoshell described in Figure 6.2 is shown in the inset of Figure 6.4. The corrected trap stiffnesses, κ_{ps} and κ_{eq}, are shown in Figure 6.4. The stiffnesses converge closely when the measured

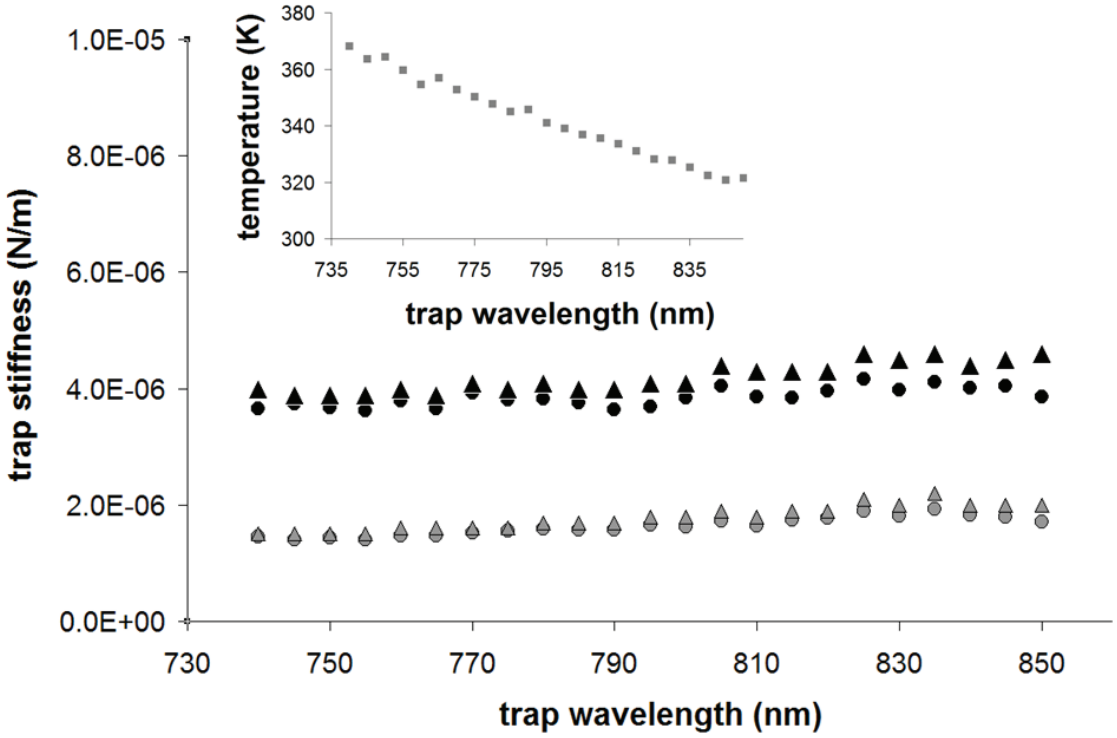

Figure 6.4: Trap stiffness, including the measured temperature (inset), for a nanoshell of the species ("940"nm) featured in Figure 6.2 determined with the power spectrum method (κ_{eq}) (dots) and the equipartition method (κ_{ps}) (triangles). Black is for data in the y-direction and grey is for data in the x-direction. The convergence of κ_{eq} and κ_{ps} shows that the temperature measurement is accurate. The trapping power is 40 mW at the trapping plane.

temperature at each trapping wavelength is included in the temperature-dependent viscosity. We reason that a comparison of power spectrum method to equipartition method shows the accuracy of the temperature measurements and is sufficient for an estimate of error. The percent difference between the two stiffness values at each wavelength ranges from 0.2 to 7%. For the other measurements of stiffness versus wavelength included and discussed in Chapter 7, the percent difference ranges from 0.2 to 20%. The percent difference in values is partially due to qualities of the detector. Both the equipartition and power spectrum method require accurate detector calibration for perfect determinations of stiffness. In particular, the equipartition technique is based on the variance, which increases with drift and noise thereby decreasing the overall stiffness measurement, and which will decrease if unintended natural low-pass filtering occurs on the detector thereby increasing the overall stiffness. Unintended filtering would also affect the temperature measurement described here, as the basis for the method lies in the high-frequency region of the power spectrum. Since we are interested more in the relative change in temperature over our wavelength trapping range, and less in absolute values, we consider the close convergence of the stiffness in Figure 6.4 to be sufficient. Repeated experiments demonstrate similar temperature values, similar changes in temperature over the range, and similar convergence of stiffness determined by the equipartition and power spectrum methods for polystyrene and silica particles and for gold nanoshells.

For the nanoshell shown in Figure 6.4, trapped at 40 mW, the measured temperature ranged from 321.48 K when trapping with light at 850 nm to 368.15 K when trapped with light at 740 nm, with an average temperature change per light wave-

length of 0.42 K/nm. As expected, and as shown with the temperature calculation in Section 6.3, the temperature increases with decreasing wavelength because the absorption coefficient of the gold nanoshell increases into the blue in this wavelength range. The measurement is repeated for another nanoshell of the same species, and the results are shown in Figure 6.5.

For the nanoshell in Figure 6.5, another nanoshell from the "940 nm" scattering resonance group, the measured change in temperature was 55.4 K (from 317.4 K to 372.7 K) for the gold nanoshell, trapped with trapping wavelengths from 850 nm to 740 nm, giving an average rise in temperature of 0.50 K per nm (inset of Figure 6.5(b)).

We observed similar changes for nanoshells with differing geometries and extinction spectra. Overall, increases in temperature ranged (for this wavelength range) from 50 K (for particles trapped at 40 mW) to 70 K (for particles trapped at 80 mW). This increase in heating is due to the absorption and conversion of energy into heat by the gold on the outer surface of the nanoshell and by the water surrounding the gold. The gold nanoshells have an increasing absorption profile towards the blue in this region of their absorption spectra. Such a drastic change in temperature is quite significant: we measured the change in temperature vs. optical power for the nanoshell described here. For a factor of 2.6 increase in optical power with constant trapping wavelength (790 nm), the temperature increased by only 3.1 K. This result (134 K/W) is similar to that determined by Seol *et al* for gold nanoparticles of a comparable diameter [30]. To achieve the large changes in temperature that we observe (which are induced only by changing the trap wavelength)

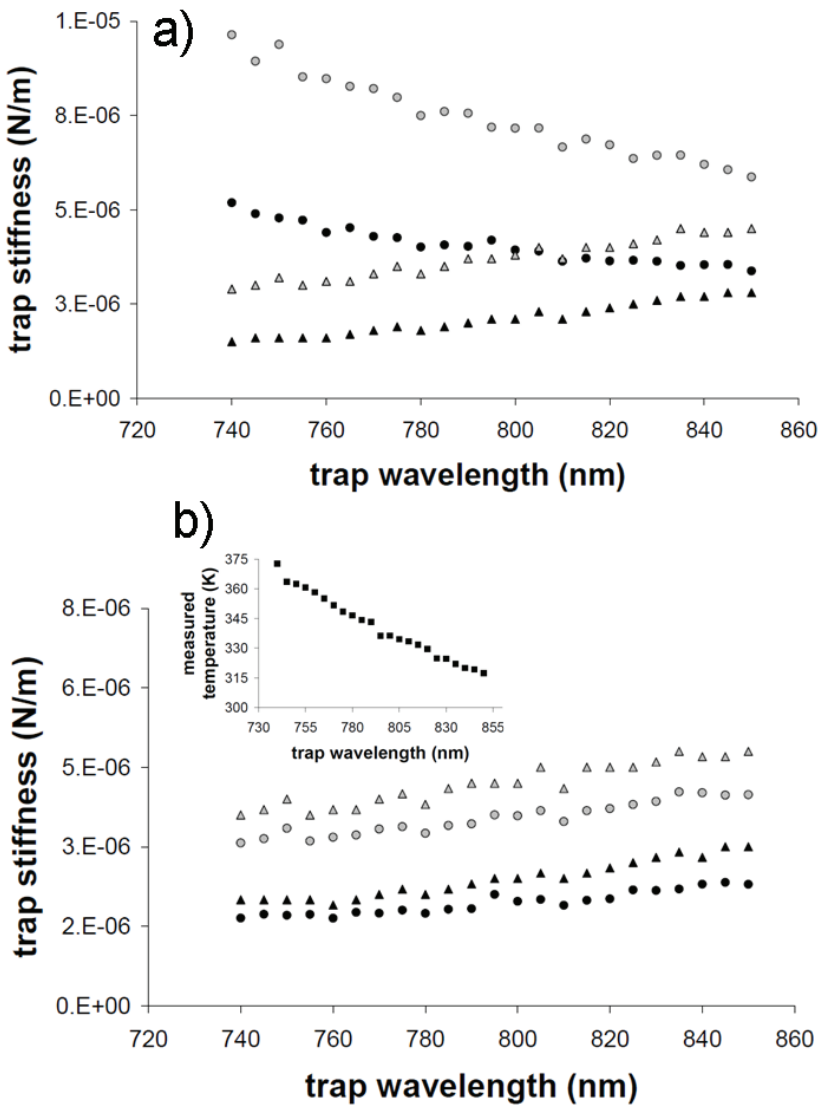

Figure 6.5: Trap stiffness as a function of temperature for an additional nanoshell with a "940" nm scattering resonance. (a) If the temperature is assumed to be a constant then κ_{eq} (circles) and κ_{ps} (triangles) diverge. (b) When the measured temperature is used to correct the values then they converge as expected. Black is for data in the y-direction and gray is for data in the x-direction. The inset of (b) shows the measured temperature for the nanoshell. In (b), the convergence of κ_{eq} and κ_{ps} shows that the temperature measurement is accurate. The trapping power is 54 mW at the trapping plane.

one would require a very large change in optical power.

Significant, however less dramatic, changes in temperature versus trapping wavelength were also observed for trapped silica and polystyrene beads. The 0.59 μm polystyrene sphere described in Section 5.8 exhibited a temperature change of 21.5 K when trapped with 40 mW of optical power, with trapping wavelengths from 850 nm to 745 nm. We believe this temperature rise is due mostly to the heating of the surrounding water from optical absorption, simply because the temperature changes observed were quite comparable for both silica and polystyrene particles of various sizes. Silica and polystyrene beads ranging in diameter (and measured at similar optical powers) exhibited similar heating with an overall average temperature increase of 26.8 K in this wavelength range, with an overall average heating of 0.25 K/nm. While the heating is not as severe as that for an absorbing particle like a gold nanoshell, the change in temperature remains quite significant.

Estimations of heating of a focused laser in an empty trap (in water) and for a trapped polystyrene particle were carried out in the manner shown by Peterman *et al* [77]. The absorption spectrum for water is taken from Ref [82] and is for water at a constant 37 degrees C. The heating from equilibrium room temperature of the water in the laser focus is 0.1 K/nm while the contribution from polystyrene in the trap is 0.007 K/nm. It appears from the calculation that the change in temperature is mostly due to the heating of the water by the laser beam, as discussed by Peterman *et al*. The overall heating of about 0.11 K/nm is somewhat consistent with our measured value of 0.25 K/nm. Differences are in part due to the water absorption coefficient dependence on temperature. This coefficient is assumed constant in the

calculation of heating contributions from water as the available data is for a constant temperature. The numerical aperture of the focused laser beam in the estimation of heating is smaller than the numerical aperture of the microscope objective used for our experiments, so this could also contribute to the underestimation of measured heating.

Temperature changes versus power have been previously measured for beads and were found to be 5.29 K/W for a 700 nm diameter silica bead in water [78], up to 8.1 K/W for a 444 nm silica bead in water, and up to 55.3 K/W for a 502 nm polystyrene bead in glycerol [77]. Again, we note that for the large temperature changes seen here for a constant optical power and a changing trap wavelength, similar temperature increases due ONLY to changing optical power would require that those changes be very large.

6.6 Discussion

The temperature calculation method discussed above for a nanoshell in an optical trap predicts significant heating, especially as the wavelength tends towards the blue. Measurements of temperature for this system also show an increased heating as the trap wavelength decreases. A comparison of trap stiffness determined by two methods shows convergence, and validates the accuracy of the temperature measurement technique. Clearly, temperature change (and therefore viscosity change) follows changing trap wavelength in optical tweezers experiments for absorbing and nonabsorbing particles trapped in water, and must be included in system calibra-

tions before accurate wavelength-dependent measurements can be realized. Other methods could be employed for determining temperature, including measurements with particles embedded in lipid membranes [76] and measurements of trapped particles subject to a well-known periodic motion of the sample chamber [77]. Viscosity could also be determined experimentally by utilizing a simultaneous analysis of CCD camera images of a trapped particle with position signals from a position detector [83]. It is important to note that repeating such measurements would be necessary for each trapping wavelength used in the data collection. Other experiments such as the measurement of trap stiffness versus ξ (the distance from coverslip to trapped particle), trap stiffness versus laser power, and others where temperature may be a changing experimental parameter also may require a measurement of heating in order to accomplish highly accurate results.

Chapter 7

Results of Resonance versus Wavelength Studies

7.1 Rayleigh Particles

As discussed in section 2.3, it is predicted that a Rayleigh particle should experience a significant change in the optical force confining it to the optical trap when the trapping wavelength is scanned over a wide range. If the wavelength is tuned from the red to the blue, towards the extinction resonance, the trap strength should increase to some maximum at a wavelength somewhat red-shifted from the resonance, and then as the wavelength is tuned further, the trap strength should fall sharply at the resonance. Continuing further into the blue side of the resonances, optical forces should be repulsive and thereafter point away from the most intense region of the laser beam. We would expect this behavior from the nanoshells trapped with the Ti:Sapphire laser whose resonances fall within or near the Ti:Sapphire wavelength range. As previously explained, a change in temperature will manifest as a change in viscosity, which will affect the trap stiffness. So both temperature and resonance can affect the stiffness. To decouple these effects, we measured the temperature and included its effects on the viscosity and stiffness for the nanoshell data presented here.

Several nanoshell species were investigated with our apparatus, and were presented in detail in Chapter 4. The first species, whose spectrum is centered at 637

nm, has the narrowest resonance peak and should therefore behave the most like a dipole. The resonance is located on the blue side of our laser wavelength range, so we expect to see an increase in trap stiffness as the trap wavelength is tuned from the red to the blue. For these nanoshells, the measured trap stiffness shown in Figure 7.1 (a) and (b) shows neither an increasing nor decreasing trend but remains relatively flat over our wavelength trapping range. Error bars for Figures 7.1 through 7.8 are the variance from the mean of the stiffnesses measured at the same wavelength for different particles of the same type. The error for the extracted spring constant associated with the fit of the Lorentzian curve to the experimental data is quite small compared to the variance described above. This error is the (plus and minus) distance to the corner frequencies of the (plus and minus) Lorentzian curves corresponding to the standard deviation of the Gaussian distribution. The average corner frequency error is 0.05% for the data presented here and never exceeds 1%, which is less than the size of the data points, and so is considered negligible in comparison to the experimental variance of the repeated data sets described above. Error bars are not included for Figures 7.9 through 7.11 due to a small number (2) of data sets for averaging. We measured the temperature for a nanoshell trapped as a function of time with no other varying parameters in order to be aware of any long-term heating or cooling effects for the system. The temperature was found to remain quite constant for over 20 minutes as shown in Figure 7.1(c), so we know that during any one data collection session (which normally lasts about 15 to 20 seconds), the temperature should remain constant in time. As expected, the temperature of the nanoshell increases with optical trapping power, as demonstrated

in the inset of Figure 7.1(c). Although the trapped nanoshell behavior corresponds to what is expected for a change in optical power, it does not for a change in trap wavelength. This nanoshell species in particular should exhibit the predicted enhanced trapping as its extinction resonance most closely resembles that of a dipole. However, no enhanced trapping is seen. This is possibly due to several factors. Most likely, the lack of enhancement occurs because the nanoshell resonance is quite broad compared to the trap wavelength range. Additionally, the nanoshell is perhaps not quite a Rayleigh particle for the wavelength range, and maybe the dynamics of the system are dominated by the silica core of the particle.

The second nanoshell species investigated has a resonance at 768 nm. This resonance peak is located within the laser wavelength range, so we expect to see an increase in the trap stiffness as the trap wavelength is tuned from red to blue, then a sharp drop in stiffness somewhat red-shifted from the resonance. Figure 7.2 shows the trap stiffness of single trapped nanoshells from this group. For this species, we again see no significant change in stiffness with trap wavelength. This nanoshell species has a broader resonance than species A, and so perhaps would exhibit less enhanced trapping, but based on our predictions, should nonetheless have a significant change in trap stiffness with wavelength. Again, we expect that the lack of enhancement is due to the broad resonance width compared to the trap wavelength range and because the particle is too large to be considered within the Rayleigh regime.

The resonance of the third nanoshell species is centered at 940 nm, so that the laser wavelength range is on the blue side of resonance. Here, we predicted that the

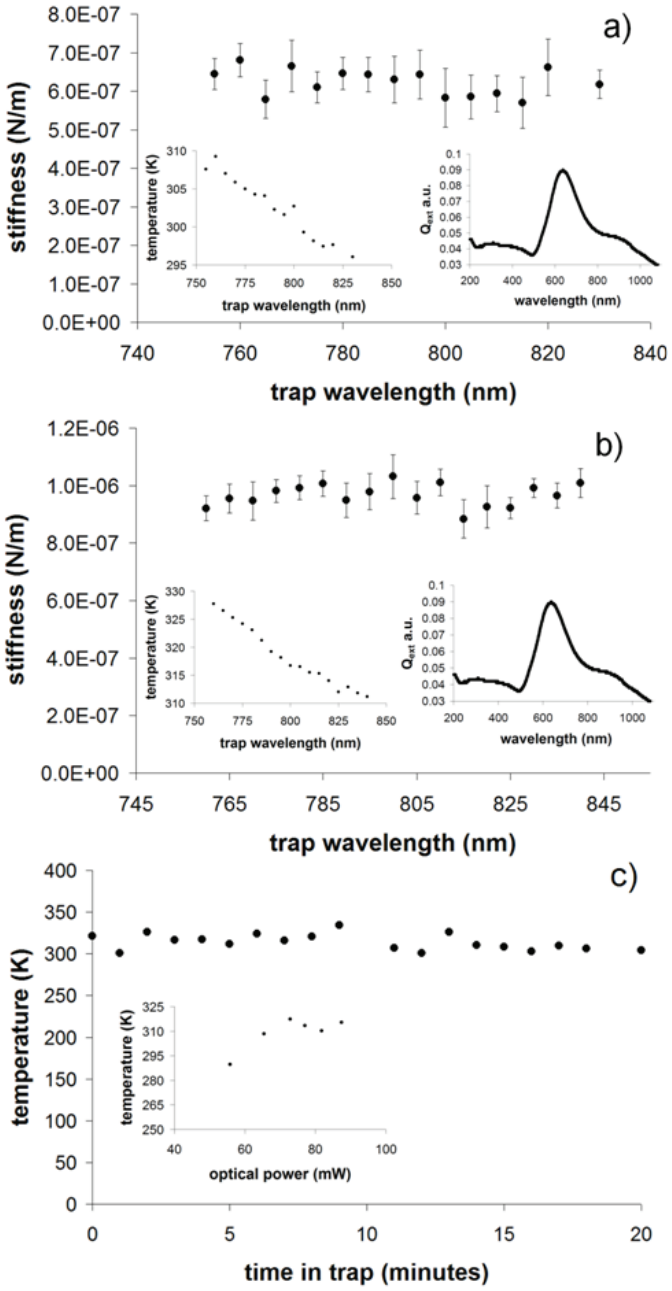

Figure 7.1: Experimental trap stiffness of single trapped nanoshells (a) and (b) with measured extinction resonance centered at 636 nm (right insets, (a) and (b). The stiffness has been corrected for changing viscosity due to the measured temperatures (left insets, (a) and (b). Changes in temperature were tested over time (c) and for increasing optical power (inset, (c)).

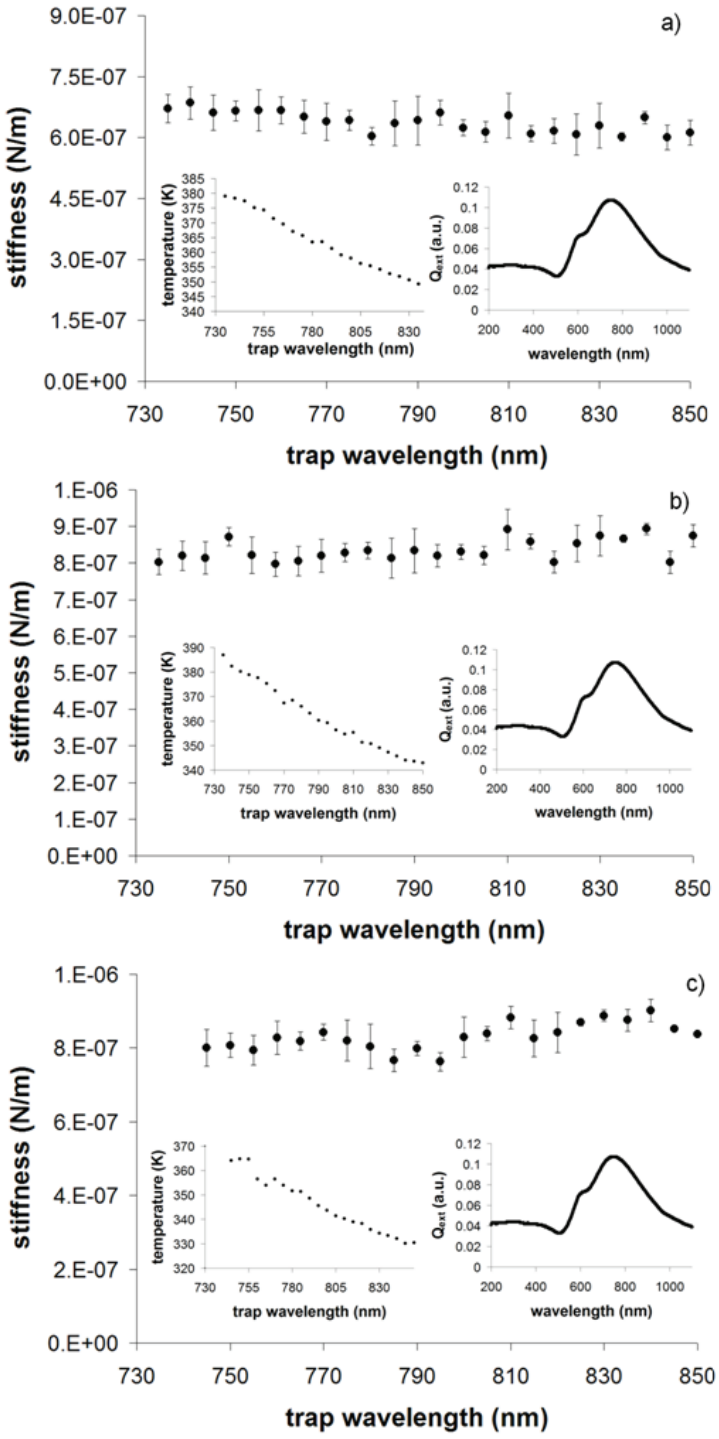

Figure 7.2: Experimental trap stiffness of single trapped nanoshells (a), (b), and (c) with measured extinction resonance centered at 768 nm (right insets,(a), (b), and (c). The stiffness has been corrected for changing viscosity due to the measured temperatures (left insets, (a), (b), and (c)).

trapping of a Rayleigh particle would not occur since we are always blue-detuned from the resonance. In Figure 7.3, each of the nanoshells demonstrates a decrease in trap stiffness from red to blue. For this species of nanoshells only, we see a decrease in trap stiffness over our wavelength range. This effect is somewhat in tune with the Rayleigh trapping theory described in Chapter 2. On the blue side of resonance, trapping should not occur for a Rayleigh particle. But perhaps for a particle that is Rayleigh-like, yet large enough to exhibit some Mie effects, trapping may be possible on the blue side of resonance. Then, based on the predictions for a Rayleigh particle, the gradient force should decrease as the trap wavelength becomes more blue. In that case, the trap stiffness would decrease as the trap wavelength becomes more blue, which occurs for the "940 nm" nanoshell species. Because trapping occurs for this species on the blue side of resonance, we can conclude that the particle is not completely Rayleigh-like, but the decreasing stiffness towards the blue leads us to believe that it does behave somewhat like a Rayleigh particle.

For the data shown here, we see a repeated trend in nanoshell heating from the red to the blue. This is due to a coincidental increase in the absorption efficiency of each nanoshell species from the red to the blue for our wavelength range. The versatility of nanoshells allow for their resonances to be tuned within the visible to infrared wavelengths, and our nanoshells happen to absorb maximally at about 600 nm. Halas *et al* utilize nanoshells whose absorption and scattering resonances overlap, so the absorption peak is aligned with the measured extinction peak. Therefore, for them, heating is maximized at the extinction resonance while for us it is maximized at a wavelength blue-shifted from the extinction resonance.

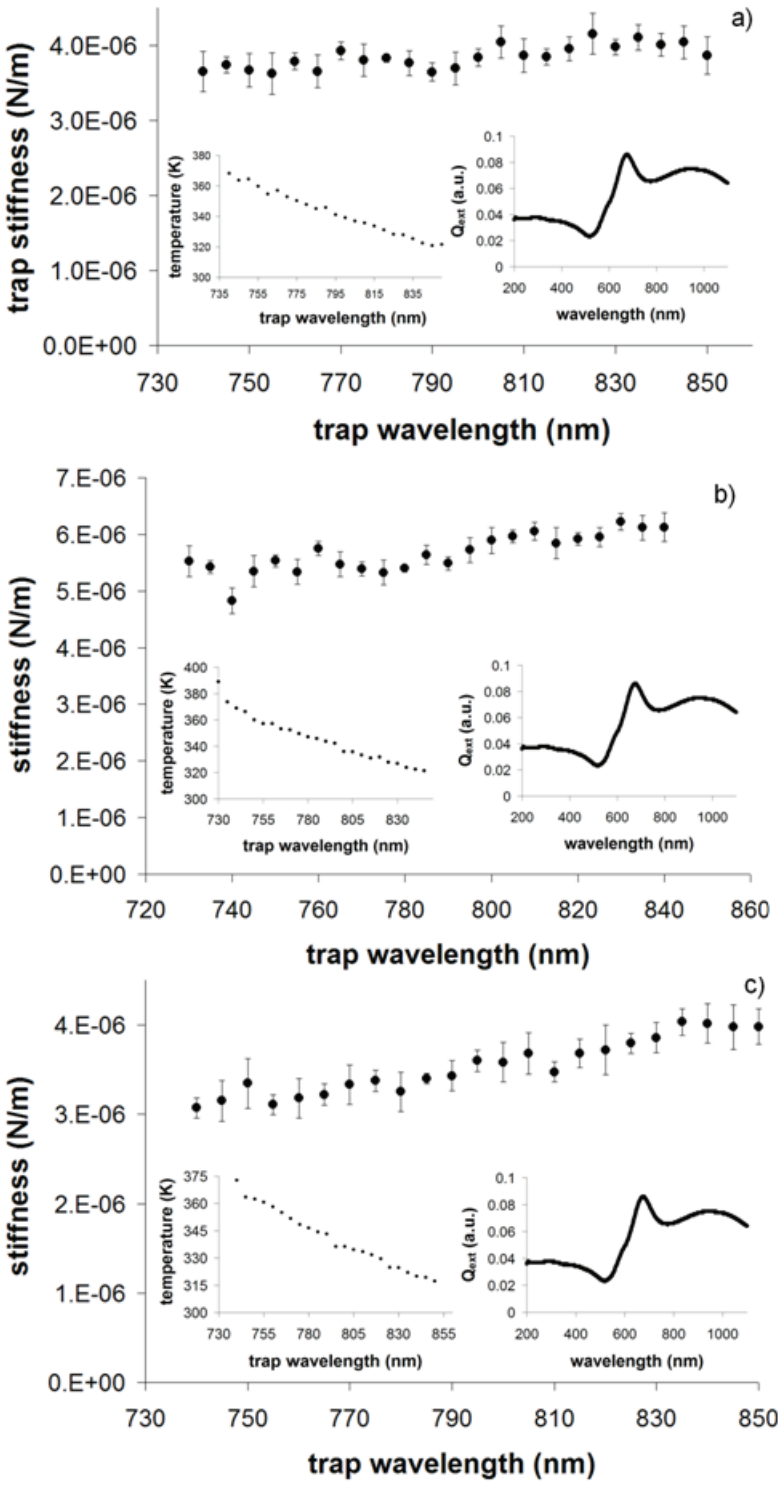

Figure 7.3: Experimental trap stiffness of single trapped nanoshells ((a),(b), and (c)) with measured scattering resonance centered at 940 nm (right insets,(a),(b), and (c). The stiffness has been corrected for changing viscosity due to the measured temperatures (left insets, (a), (b), and (c).

7.2 Mie Particles

Both polystyrene and silica spheres were trapped in order to study the effects of trapping Mie particles over a wavelength range. Based on calculations carried out by Stilgoe [11], we predict that a significant change in trapping forces should be realized when trapping polystyrene or silica particles in the 300 nm to 1 μm diameter range with this range of trapping wavelengths. I show only one data set per particle size here because the manufactured polystyrene and silica spheres are much more homogeneous than the nanoshells. The trap stiffness of the 0.39 μm polystyrene bead in Figure 7.4 remains relatively constant in the trapping range. The somewhat larger 0.59 μm polystyrene bead has a slightly increasing trap stiffness as the wavelength becomes more blue, as shown in Figure 7.5. The trap stiffness of the 0.69 μm polystyrene bead in Figure 7.7 shows a slight decrease in the trap stiffness as the trap wavelength is tuned more towards the blue. Two silica bead sizes were also investigated: 0.6 μm and 0.8 μm. Their trap stiffnesses (Figures 7.6 and 7.8, respectively) similarly decrease as the trap wavelength becomes more blue. None of the beads investigated showed the anticipated large change in trap stiffness with trap wavelength. These five data sets were recorded on a calibrated detector, so the changing measured temperature and corresponding viscosity are considered in the trap stiffness. Again, no significant force enhancement is seen for these particles trapped in our wavelength range. Our predictions for enhancement for these particles are based on plots generated by Stilgoe *et al.* Their results are fashioned for a particular system with a specific numerical aperture, which does not

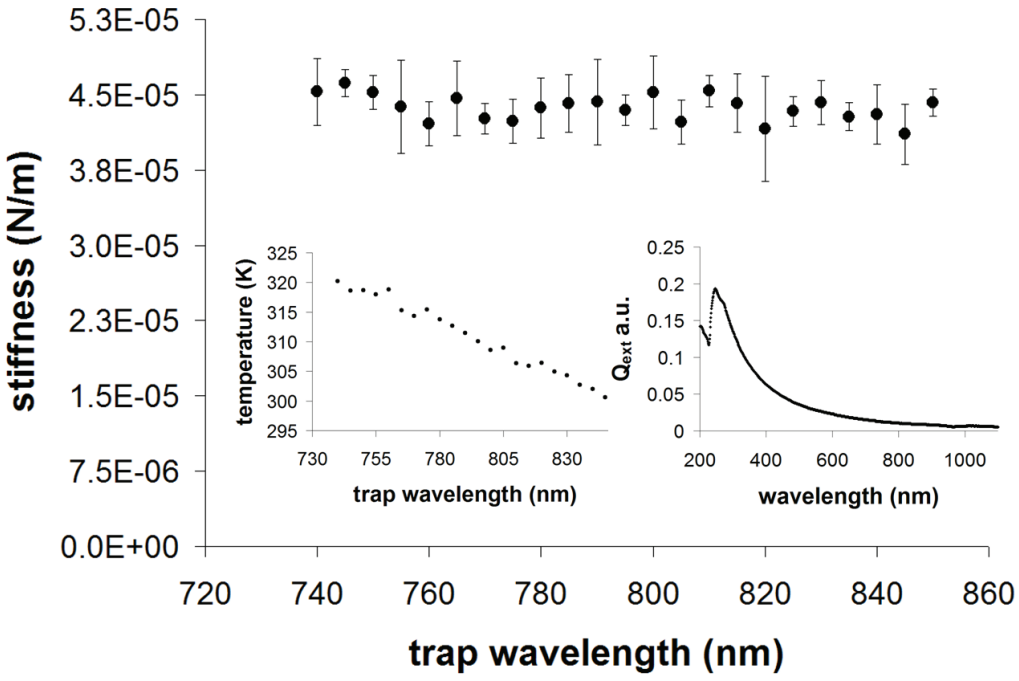

Figure 7.4: Experimental trap stiffness of a single trapped 0.39 μm polystyrene bead with measured scattering resonance shown in the right inset. The stiffness has been corrected for changing viscosity due to the measured temperatures, left inset.

match ours. Small changes in numerical aperture cause large changes in trap stiffness versus trap wavelength results. So it is likely that for our wavelength range with our numerical aperture, particles which would exhibit the most extreme enhancement are in a different size regime than the ones we investigated.

The aforementioned importance in knowing system temperature was discovered after many measurements had already been made with this apparatus, and up to that point detector calibration was not necessary. So several additional bead sizes were investigated, but with an uncalibrated detector. Therefore, the temperature could not be determined for these data sets, and was assumed to be a constant

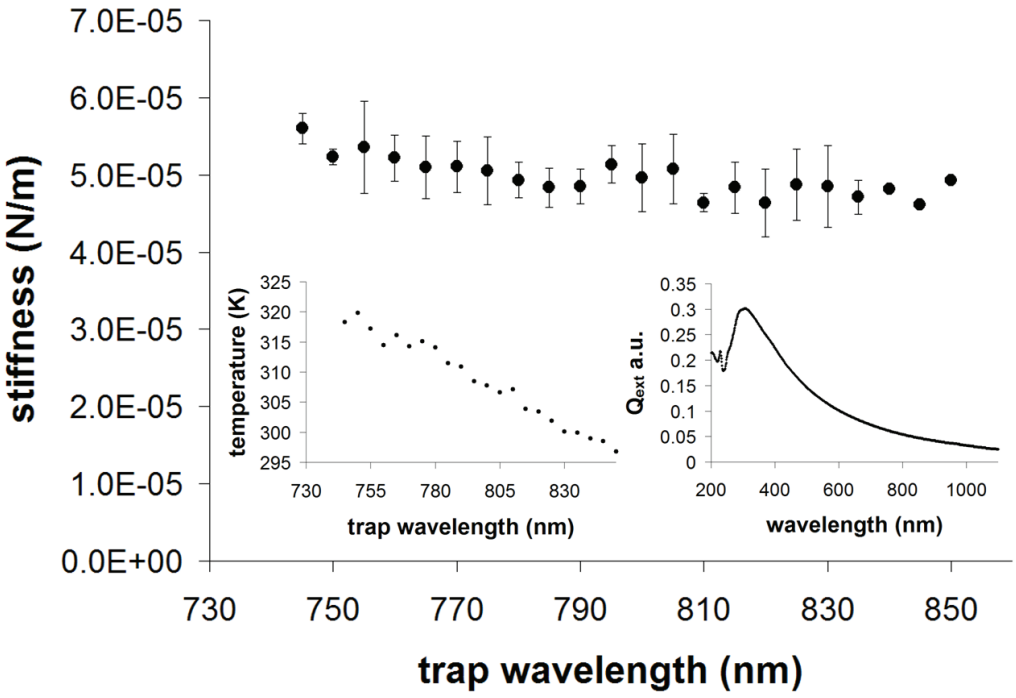

Figure 7.5: Experimental trap stiffness of a single trapped 0.59 μm polystyrene bead with measured scattering resonance shown in the right inset. The stiffness has been corrected for changing viscosity due to the measured temperatures, left inset.

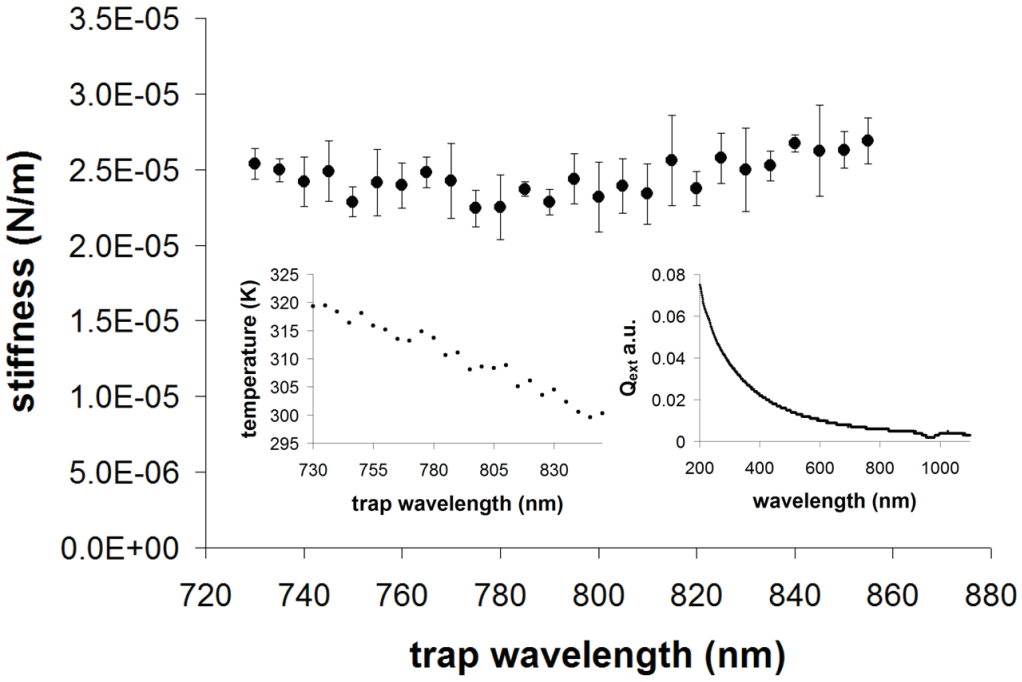

Figure 7.6: Experimental trap stiffness of a single trapped 0.60 μm silica bead with measured scattering resonance shown in the right inset. The stiffness has been corrected for changing viscosity due to the measured temperatures, left inset.

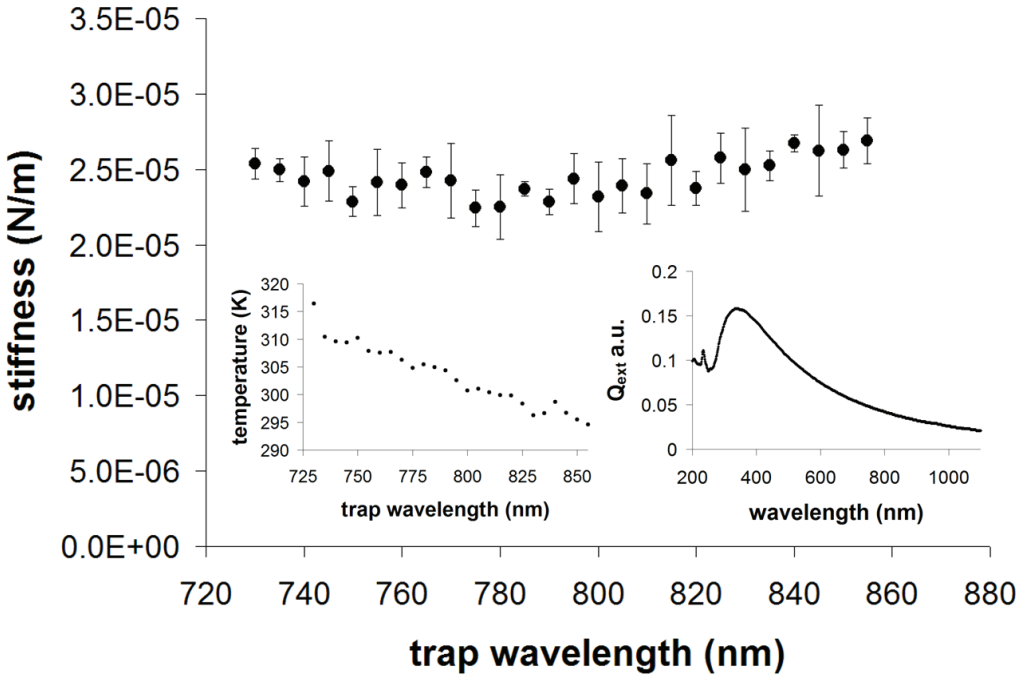

Figure 7.7: Experimental trap stiffness of a single trapped 0.69 μm polystyrene bead with measured scattering resonance shown in the right inset. The stiffness has been corrected for changing viscosity due to the measured temperatures, left inset.

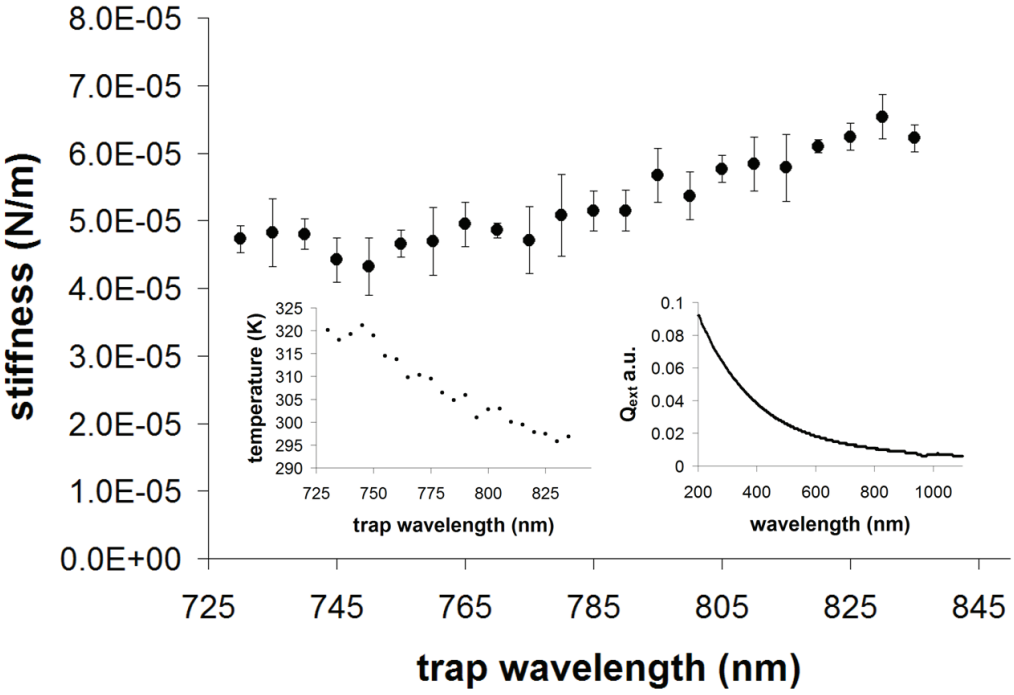

Figure 7.8: Experimental trap stiffness of a single trapped 0.80 μm silica bead with measured scattering resonance shown in the right inset. The stiffness has been corrected for changing viscosity due to the measured temperatures, left inset.

at room temperature for the the trap stiffness data shown in Figures 7.9 through 7.12. The stiffness increases significantly towards the red for the 0.94 μm particle in Figure 7.9. For the similarly sized polystyrene particles shown in Figures 7.4 to 7.7, the temperature increases significantly and consistently with decreasing wavelength, and so most likely increases significantly for the 0.94 μm particle as well. If the changing temperature were considered in the trap stiffness here, it would cause a decrease in the apparent stiffness towards the blue causing the overall curve to flatten out like those previously presented. This may not be true for larger particles. The trap beam waist is on the order of 1 μm. For the remaining three particles shown here, the particle diameter is significantly larger than the beam waist, meaning the most intense region of the beam is confined within the polystyrene or silica, which absorb, and therefore heat, less than water. So for these three particle sizes, the assumption of a constant temperature may be close to accurate, meaning the trap stiffnesses shown here are also not far from accurate. Other different behaviors are observed for these included "large" beads. A large dip is seen in the plot for the 2.4 μm polystyrene sphere in Figure 7.10, and this is not seen for any other particle studied. The largest particle investigated in this study, 5.5 μm, did seem to exhibit wavelength effects; the stiffness changes by a factor of two, but with a high frequency, most likely due to the whispering gallery mode resonances discussed in Chapter 3. If the detector had been calibrated and temperature effects could have been included for this data, based on the effects seen for smaller particles, the data would probably feel a tilt down towards the blue. For the 0.94 μm particle, this would cause the slope to become larger and the "resonance" effect to become more

pronounced. For the 2.4 μm particle, the data would perhaps tilt towards the blue, yet still exhibit the large dip in the central region. For the 5.5 μm particle, again the data set would feel a tilt towards the blue but the large peaks and valleys would remain. We believe these large changes in stiffness over trap wavelength are resonance effects, but cannot definitively conclude as such since the measurements were not performed with a calibrated detector in order to determine any temperature dependencies.

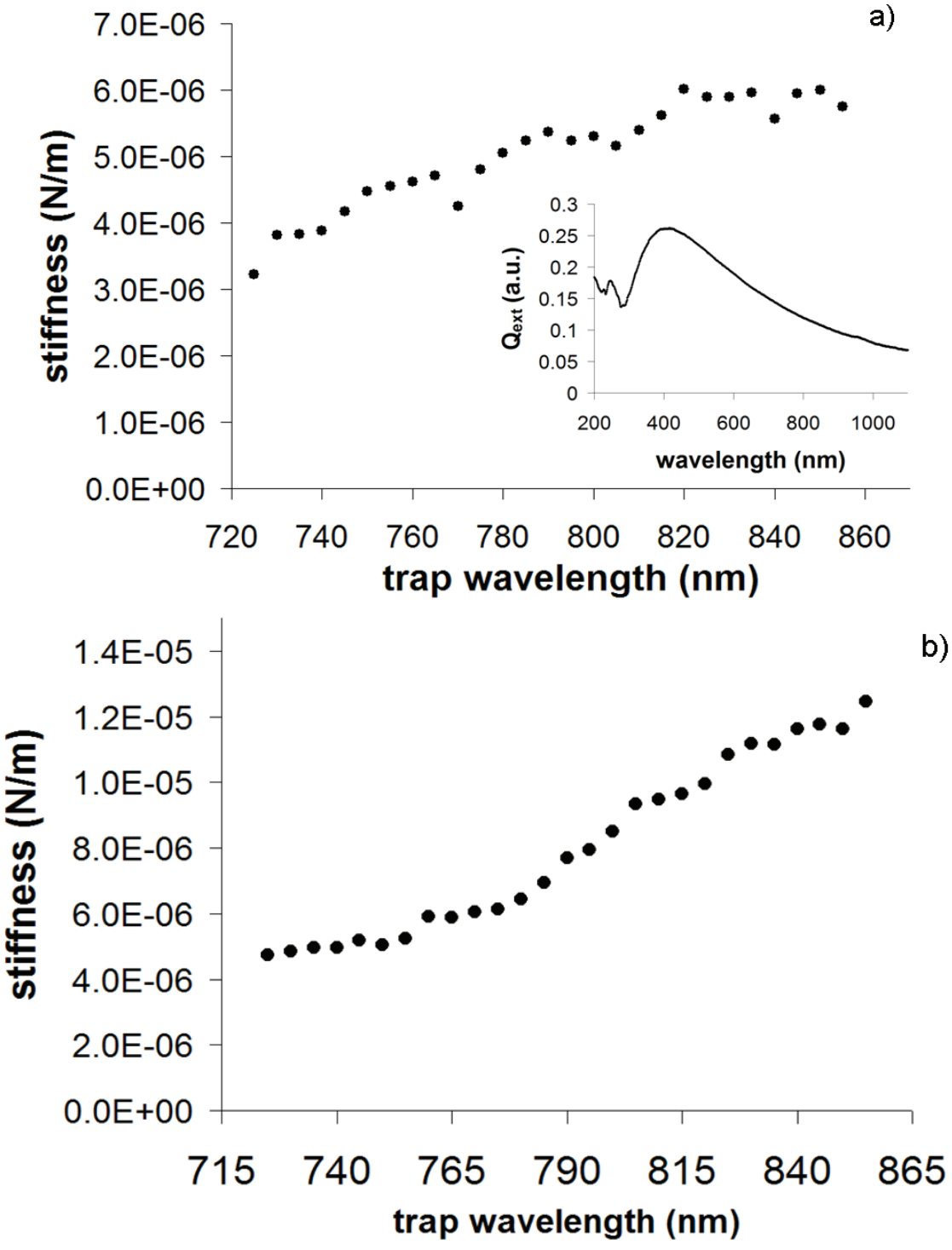

Figure 7.9: Experimental trap stiffness of single trapped 0.94 μm polystyrene beads (a) and (b) with measured scattering resonance shown in inset of (a). The temperature and viscosity are assumed to be constant with wavelength.

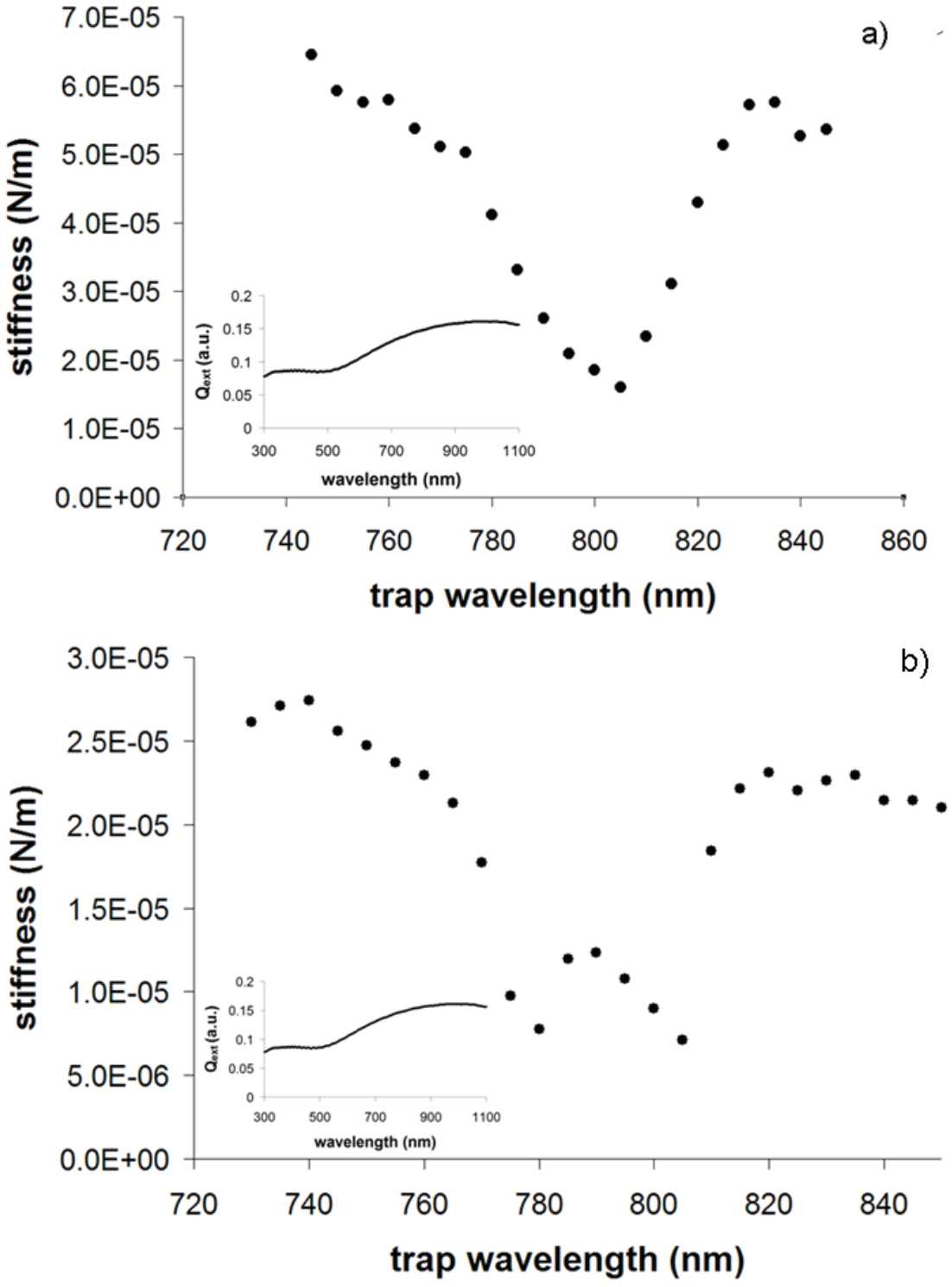

Figure 7.10: Experimental trap stiffness of single trapped 2.4 μm polystyrene beads with measured scattering resonance shown in the left inset. The temperature and viscosity are assumed to be constant with wavelength.

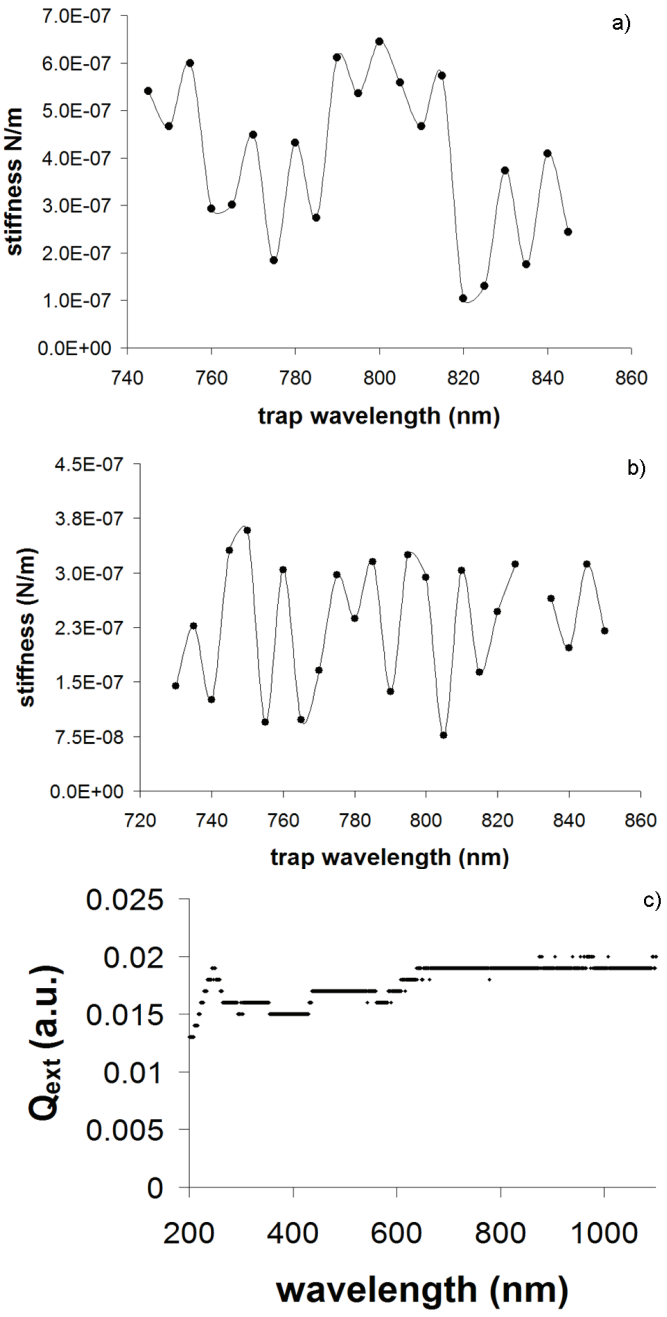

Figure 7.11: Experimental trap stiffness of single trapped 5.5 μm polystyrene beads (a) and (b) with measured scattering resonance shown in (c). The temperature and viscosity are assumed to be constant with wavelength.

Chapter 8

Multiple Nanoshell Trapping

8.1 Experimental Signals and Nanoshell number

While we made a considerable effort to restrict our measurements to single trapped nanoshells, we inevitably trapped and took measurements of multiply-trapped nanoshells as well. Figure 8.1 shows the position versus time trace for increasing numbers of trapped nanoshells. To show this effect, the nanoshell concentration we normally used was greatly increased in order to demonstrate the jump in signal as particles enter the trap. As shown, with increasing trapped particle number, the position signal increased. Spikes in the signal are apparent as the second (at 29 seconds) and third (at 34 seconds) nanoshell enter. This is because while entering the trap, they are moving over a large distance compared to the already trapped nanoshell(s), whose motion remains confined within the small trap domain. The nanoshells trapped in this time trace were of the "940 nm" species (resonance centered at 940 nm) described in Chapters 4 and 7, and were trapped with 40 mW of $\lambda = 805$ nm light. Figure 8.2 shows the x and y position for the scattered light on the PSD for the entire time trace in Figure 8.1. The amplitude of scattered light, corresponding to the position of the particle, is largest when the most particles are trapped, due to an increased scattering cross section, and perhaps also to a change in the particle amplitude in motion due to a temperature increase. This is also

apparent in Figure 8.3, which displays corresponding histograms for the same data shown in Figures 8.1 and 8.2. Note that in Figure 8.2 the displacement is greater in one direction as compared to the other. This is because for Rayleigh-like particles, trapping forces are dependent on whether or not they are parallel or perpendicular to the polarization direction of the trapping laser light [84]. Figure 8.4 displays power spectra for one, two, and three nanoshells in the optical trap, corresponding to the data in Figures 8.1 - 8.3. The corner frequency and power spectral amplitude both increase for two nanoshells in the trap as compared to one. Although studies have shown that for dielectric particles, the trap stiffness should decrease as more and more particles enter the trap [73], our results are instead consistent with previous experiments performed with gold nanoparticles (GNPs) [72], where the corner frequency increases as the size of the trapped GNP increases, and similarly, the corner frequency increases when two GNPs are trapped as compared to one. It has been shown that groups of plasmonic nanoparticles will undergo optical binding when trapped and form a stable configuration [85]. We see the corner frequency increases for two particles and then decreases for three particles. This may suggest that optical binding is occurring when two nanoshells are in the trap, causing the two particles to behave as one single larger particle. However when a third nanoshell enters the trap, the corner frequency drops as it would for a system of dielectric particles. This suggests that the optical binding is stronger for two nanoshells than for three nanoshells. The change in corner frequencies from two to three nanoshells could also be explained by a raise in temperature of the system. The temperature increases with the number of particles (see next section), which

causes a decrease in viscosity. The trap stiffness is directly proportional to viscosity, so it would decrease as we see happening when going from two to three particles in the trap. This does not occur however, when going from one to two particles in the trap. In this thesis, I focused on temperature and resonance effects for single nanoshells in an optical trap, but it would be interesting to study these effects from trapping multiple nanoshells in the future.

8.2 Temperature Measurements of Trapped Nanoshells

Our method of temperature measurement was repeated for trapping the single, double, and triple nanoshells shown in Figure 8.1. The measured temperature was 320.1 K for the single nanoshell, 372.2 K for the double nanoshells, and 403.22 K for the triple nanoshells in the optical trap. While boiling was observed for clusters of nanoshells fixed on a coverslip, it never occurred for nanoshells confined to the optical trap, and in the case of the research conducted for this work, a maximum of only four nanoshells was observed to ever be confined to the trap at one time. For boiling to occur, a seed must exist in order to nucleate a bubble which must exceed surface tension forces which scale inversely with the particle radius. This will occur at a substantially increased temperature compared to that of the boiling point of bulk water, yet below the critical point of 641 K. So we can assume that the nanoshells in motion in the optical trap heat significantly, but at equilibrium, maintain a cool enough temperature such that the water surrounding them remains in the liquid state. Fixed clusters of nanoshells, similar to those utilized in tumor

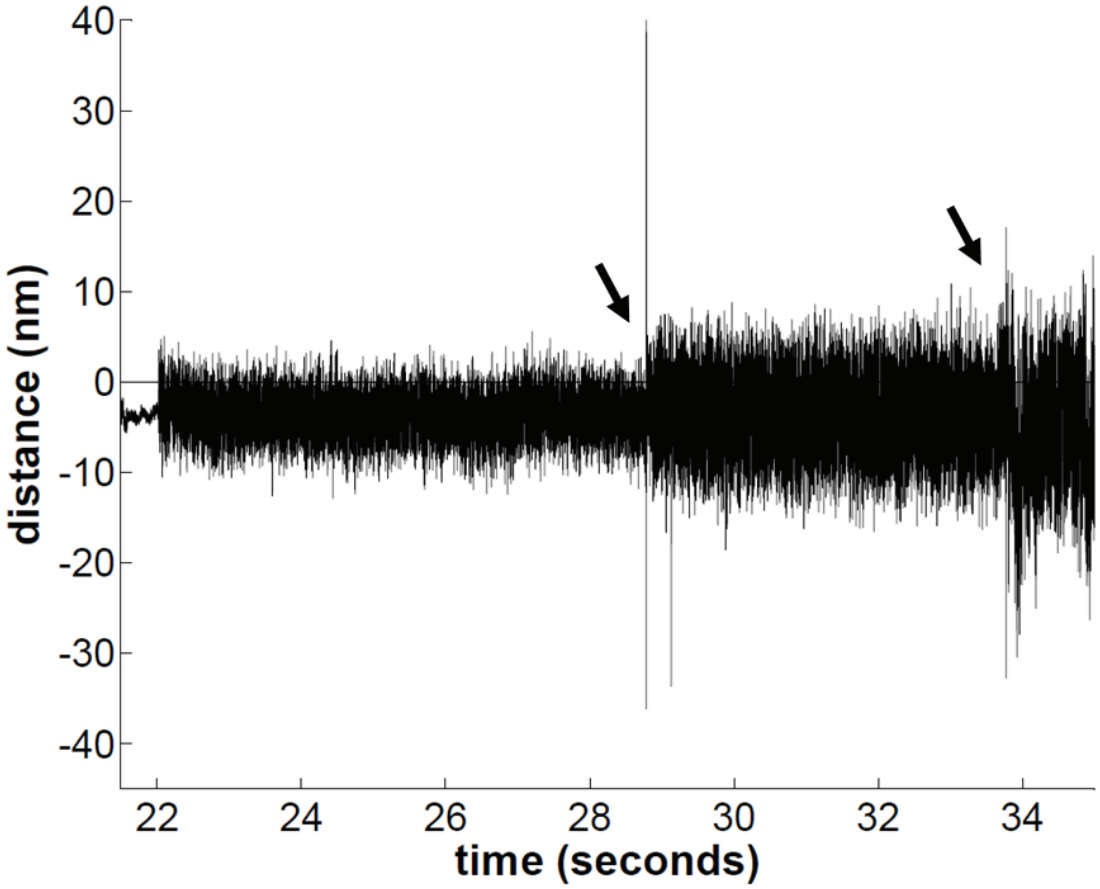

Figure 8.1: Position versus time plot: First the trap is empty, then a nanoshell enters the trap at 22 seconds. Next, a second nanoshell enters the trap at 29 seconds, causing an increased position amplitude. Finally, a third nanoshell enters the trap at 34 seconds, again increasing the position amplitude. Arrows indicate when additional shells enter the trap.

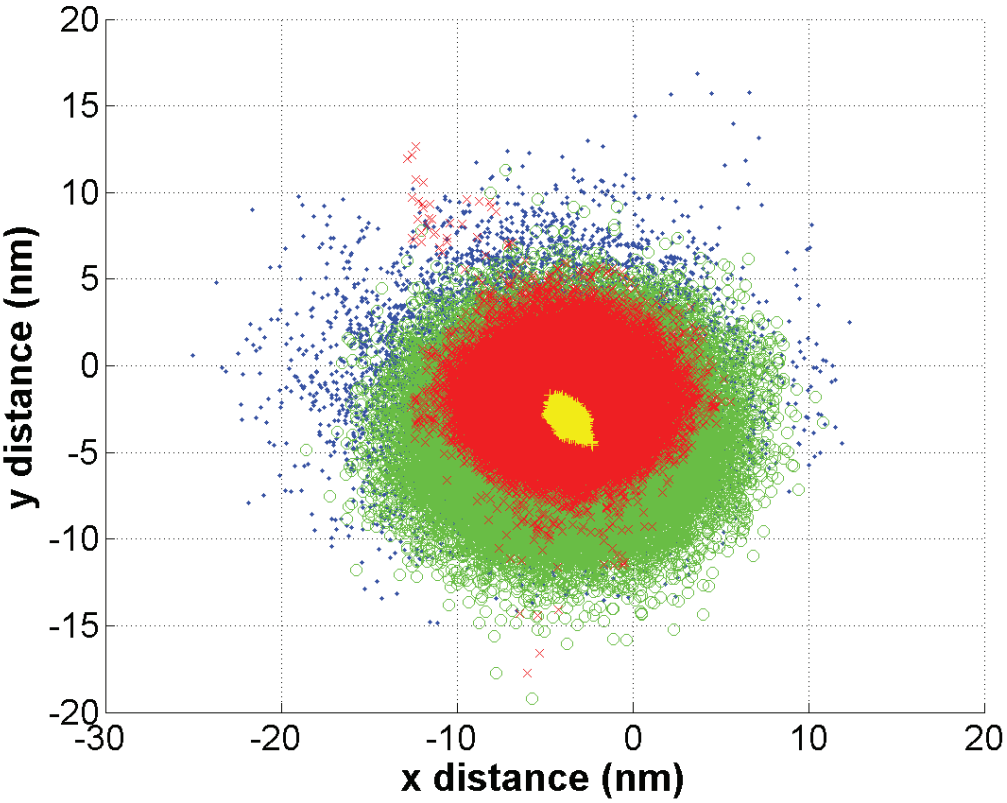

Figure 8.2: x position versus y position plot for the full time trace in Figure 8.1. Yellow plusses - empty trap, red crosses - one nanoshell in the optical trap, green circles - two nanoshells in the optical trap, blue dots - three nanoshells in the optical trap.

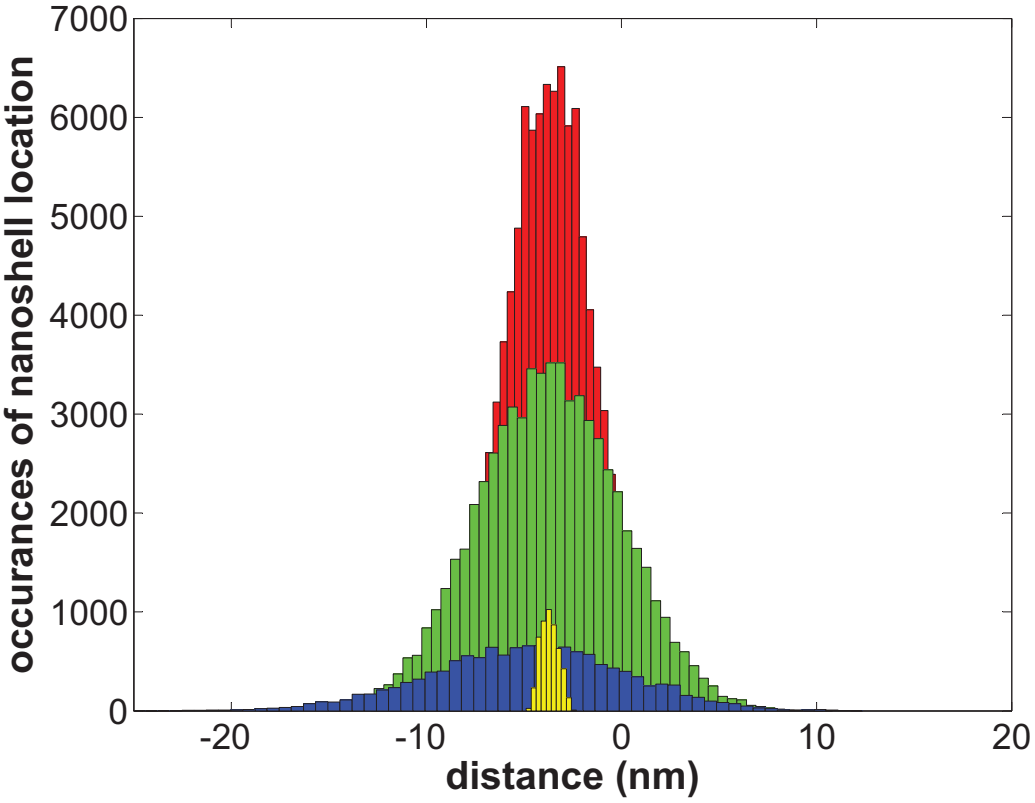

Figure 8.3: Histogram plot for each individual time trace shown in Figure 8.1. Yellow - empty trap, red - one nanoshell in the optical trap; Full width half max (FWHM) = 5.35 nm, green - two nanoshells in the optical trap; FWHM = 6.61 nm, blue - three nanoshells in the optical trap; FWHM = 8.60 nm. Y-axis is the number of counts per location on the detector. Bin width is 0.5 nm.

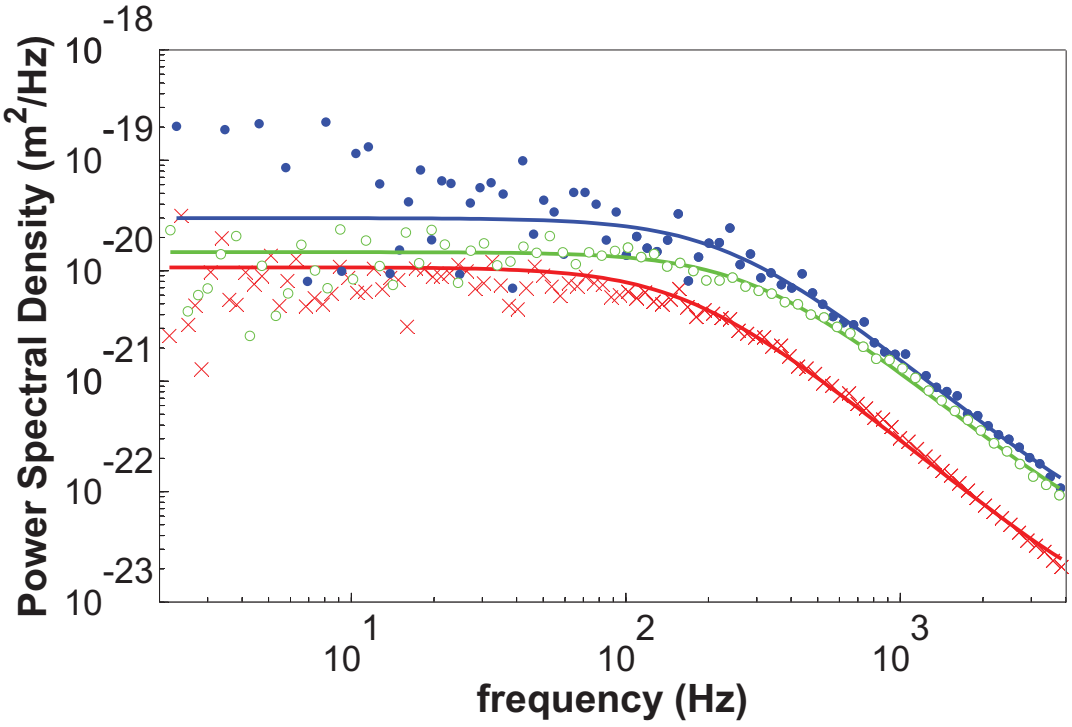

Figure 8.4: Power spectra for trapped nanoshells shown in Figure 8.1. Red crosses - one nanoshell in the optical trap, f_c= 196.6 ± 4.6 Hz, green circles - two nanoshells in the optical trap, f_c= 400.5 ± 5.1 Hz, blue dots - three nanoshells in the optical trap, f_c= 312.8 ± 8.1 Hz

ablation, would exhibit a temperature high enough to boil water, at least when irradiated with light similar to that used in our experiments. To our knowledge, this and the data presented above is the first measurement of the temperature of an individual nanoshell in a laser beam or multiple nanoshells in a laser beam.

8.3 Discussion

In most optical tweezer experiments which utilize dielectric particles, knowledge of multiple particle trapping is most important not for its own sake, but rather for ensuring the trapping of only one particle at a time. However, in the case of plasmonic particles such as gold nanoshells, multiple particle trapping asks an entirely new set of scientific questions. How does the number of particles in the trap change the optical forces involved? How is the system heating affected by particle number? Can these effects be applied for some interesting result? In the case of gold nanoshells, how would the increased heating benefit in tumor ablation studies? We begin to answer these questions with the data presented here, but more research is necessary for complete answers to these interesting questions.

Chapter 9

Conclusions

Within an optical tweezers system, the absorption and scattering of light should affect the optical forces responsible for trapping the object. Specifically, optical trapping forces are dependent upon the difference between the trap wavelength and the extinction resonances of a trapped particle. This leads to a wavelength-dependent trapping force, which should allow for the optimization of optical tweezers systems, simply by choosing the best trapping wavelength for a given experiment. While several studies have examined the physics of the trapping forces in optical tweezers systems, the effects of the trapping wavelength and optical properties of the trapped particle have not been studied extensively with a focus on optical forces. In this thesis, these effects were tested using optical wavelengths and particle types and sizes readily available to the scientific community.

Although optical forces due to a near-resonant laser beam have been studied extensively for atoms, the situation for larger particles has only been studied numerically [9] and, until recently, remained experimentally unverified. A Rayleigh particle is expected to behave much like an atom in an optical trap. The small size of the particle compared to the large uniform electric field results in a dipole response. In such a case, the optical forces are dominated by the complex polarizability of the particle, which is inherently linked to the extinction (scattering plus absorption)

resonance of the particle. The total trapping force is a sum of the gradient and scattering forces. The gradient force, which is mostly responsible for trapping, will increase as the trapping wavelength approaches the resonance from the longer wavelengths, come to a maximum close to the resonance wavelength, and drop sharply at the scattering resonance [10].

For larger particles whose size is on the order of the wavelength, predictions require rigorous numerical calculations (based on solving Maxwell's equations for specific conditions) and cannot be viewed with such a simple picture, yet the forces are still resonance-dependent. For some trapping schemes with polystyrene particles, wavelength dependence has been calculated, and maximal trapping forces are predicted to exist when the ratio of particle radius to trap wavelength is in the range of one half to three-quarters [11]. Particles whose diameter are much larger than the trap wavelength are not expected to exhibit resonant behavior when considering optical forces, because the trap size is very small compared to any large sphere [12]. Hence, enhanced optical forces near a resonance are only expected for Rayleigh particles and for particles whose size is comparable to the trap wavelength.

In order to test the effects of trapping wavelength on optical forces, I achieved optical trapping, visualization, detection, temperature measurement, and trap stiffness measurements of gold nanoshells and dielectric microparticles. For this, a reliable apparatus with wavelength tunability was constructed, tested, and implemented for carrying out these measurements, along with a specific set of techniques required for accuracy of the measurements. These techniques included the calibration of the PSD, of the system optical power, and of the instruments responsible

for guided motion (picomotors). Also included was a set of methods developed in order to prevent the change in optical properties due to a change in light wavelength from affecting the measurement outcomes. Direct measurements of temperature of a single trapped particle were achieved in order to correct for heating and its effects on the determinations of trap stiffness. Additionally, since the trapping of more than one particle will change voltage signals significantly and affect the accuracy of measurements, I also took care to ensure that only one particle is trapped in the laser during data collection.

With a working apparatus, optical trap stiffness was measured for trapped particles as a function of wavelength. Although we do not observe the three to fifty times enhancement predicted for optical trapping of a Rayleigh particle when trapping near the red side, we do see evidence that when trapping on the blue side, the stiffness decreases as the trap wavelength decreases. The predictions of the three to fifty times enhancement were based on numerical data generated for a wavelength range spread over 1500 nm. While our lasing range of 130 nm is much larger than that of a typical tweezers system, it is still a limiting factor in these experiments. The predictions of resonance-based enhancement were also based on the optical trapping of a 10 nm particle, which is orders of magnitude smaller than the light wavelengths in the range of calculations. Our nanoshells are considered Rayleigh particles [68], but are only one order of magnitude smaller than the light wavelengths used for trapping. Therefore, based on their behavior in an optical trap, we conjecture that nanoshells do not behave in every way like Rayleigh particles for our wavelength range. Nanoshells for which the trapping range is located on the red side or within

the center of the extinction peak exhibit a more or less constant trap strength. While they exhibit a decreasing trap strength as the trapping wavelength decreases, on the blue side of the resonance, surprisingly they are still stably trapped. For the Mie particles, we see resonance effects for very large beads whose diameter is on the order of 2 to 5 μm, but not for smaller beads (0.3 to 0.8 μm) for which the most enhancement is expected. This is most likely due to the fact that our apparatus and materials differ significantly enough from the ones used in the calculations predicting this enhancement.

Throughout this study, many questions other than the original (stiffness vs. wavelength?) were raised. Like so many others, this experiment tackled a few specific issues while it introduced several new interesting questions. These are included in the next and final chapter of this thesis.

Chapter 10

Suggestions for Future Experiments

In the present work I constructed a custom, but versatile system and developed set of methods allowing for measurement of optical properties of single nano- or microparticles as a function of wavelength. I avoided the more commonly used commercial inverted microscope in order to allow for an evolving system, so that it could be adaptable throughout its optimization. This instrument measured the motion of a trapped particle with back focal plane interferometry, but the system could be easily altered to incorporate other light sources and detector types for a variety of single-particle measurements. The types of experiments that could be carried out with this apparatus including studies of index of refraction of particles, of wavelength-dependent heating or other effects in biological systems, and wavelength-dependent effects in particles composed entirely of metal. With this apparatus, as long as the particle can be trapped, its optical properties (or perhaps other properties) may be studied. The bulk properties of a material can differ greatly from those on the nano-scale. The apparatus will provide a means for the measurement of those smaller-scale properties for single particles surrounded by a uniform fluid, preventing the need for a motion-locking substrate.

It may be possible that a laser with a broader wavelength range could be implemented into the system, allowing for more descriptive single particle measure-

ments. In this case, more care should be taken to prevent changes in the trap size and changes in chromatic aberrations from affecting the experimental outcome. With a more widely tunable laser, the resonances of gold nanoshells and dielectric spheres will be comparably more narrow, allowing for much more comprehensive studies. Results from such an experiment will provide a deeper understanding of fundamental phenomena in optical trapping science.

While the apparatus presented here proved to operate in an successful manner, some alterations could be applied to enhance its performance for specific experiments.

In order to prevent some necessarily repeated calibrations, in future experiments the researcher may consider a single wavelength detection laser. For our apparatus, as the trapping and therefore detection wavelength is tuned, a repeated measurement of the position detector is necessary during the PSD lateral signal calibration process for each wavelength used for detection. A low-power single wavelength detection laser whose signal is isolated on the PSD would be a less time-consuming option for experiments requiring detector calibration.

Another part of the apparatus which could be improved is the stage control system. Picomotors do not have an extremely consistent step size, cause significant vibration with each step, and have a high degree of hysteresis. Several of the calibrations and methods covered in Chapter 5 are quite sensitive and require a reliable mode of well-known distance and motion control. Another, more updated piezo-actuated system would offer a more reliable and much smaller step size with less hysteresis. This would facilitate the calibration process and decrease the number of

times the calibration should be repeated.

This experiment was intentionally designed for adaptation. For future wavelength-dependent optical trapping studies with a specific focus, a commercial microscope could possibly be a better option as the apparatus scaffolding. Many optical techniques such as dark field imaging, differential interference contrast (DIC) imaging, and interferometry require highly accurate placement of optical components. A commercial microscope system can be purchased with the appropriate settings in place so that these types of techniques are readily carried out. Otherwise, the optical tweezers system could be crowded with bulky high-resolution translation stages.

For an experiment that would continue the research presented here, a worthwhile addition to the apparatus might be a single particle spectrophotometer. In our experiments, the particle trapped in the optical tweezers was assumed to possess the same absorption and scattering profile as the bulk sample from whence it came. It is possible that this was not always true. Hence, the ability to measure the extinction (absorption plus scattering) of the trapped particle would be a great advantage. Single-particle optical-tweezer spectrometers have been introduced into the literature [86, 87] but have not yet been coupled to an optical tweezers system capable of simultaneous position detection.

Many questions were raised throughout the experiment described in this thesis. Our results do not always agree with our predictions. Gold nanoshells exhibit Rayleigh particle qualities for our measurements of their light scattering and absorption, but do not have this Rayleigh-like behavior in an optical trap. Certain Mie particles should trap much stronger at certain wavelengths, according to cal-

culations using Lorenz-Mie scattering theory. In our attempts to demonstrate this experimentally, we did not observe a particle for which this is true in our wavelength range. More experiments, with a more widely-tunable laser (or set thereof) with a higher variety of particle sizes would contribute towards a better understanding of each optical trapping system.

We also encountered new mysteries in our observations with plasmonic particle trapping. The relationship between plasmonic fields and optical binding effects are not completely understood, and could be studied in multiple vs. single trapped particle experiments. System heating could also be investigated for a better understanding of tumor ablation studies.

The optical tweezers system for wavelength-dependent studies introduced in this thesis functioned very well for the experiments carried out in the force enhancement studies included here. Its adaptability is perhaps its best quality, allowing for a variety of future investigations. The experiment described in this work also can contribute to future scientific explorations by means of the interesting questions it has raised. Perhaps the most successful scientific experiment is one that solves the original problems while posing a brand new series of questions.

Appendix A

Source Code for Data Collection

A.1 Visual Basic Program

A.1.1 Bulk particle extinction resonance measurement

The following code is used for communication with the Spectronic spectrophotometer.

```
Option Explicit

Dim Output As String
Dim Buffer As String
Dim Thang As String
Dim ValueStr As String
Dim TotalLen As Integer
Dim OLoc As Integer
Dim ELoc As Integer
Dim NumStr As String
Dim Length As Integer
Dim Length2 As Integer
Dim Length3 As Integer
Dim vbCrLoc As Integer
Dim Res As Integer
Dim BWL As Integer
Dim EWL As Integer
Dim FileBuffer As String
Dim vbCrLoc1 As Integer
Dim vbCrLoc2 As Integer
Dim DataPoint1 As String
Dim DataPoint2 As String
Dim Out As Variant
Dim Message As String
```

```
Dim NewFileBuffer As String
Dim txtResOK As String
Dim txtBWLOK As String
Dim txtEWLOK As String


Private Sub cmdBScan_Click()
      cmdBScan.Enabled = False
      cmdSaveAs.Enabled = False
      cmdClear.Enabled = False
      cmdCellU.Enabled = False
      cmdCellD.Enabled = False
      cmdSend.Enabled = False
      cmdQuit.Enabled = False
      cmdScan.Enabled = False
      lblDisplay.Caption = ''''
      lblDisplay.Caption = ''SCANNING BASELINE. PLEASE WAIT.''
      MSComm1.Output = ''BASELINE 1 200 1100'' & vbCr
End Sub

Private Sub cmdCellD_Click()
      MSComm1.Output = ''CELL-'' & vbCr
End Sub

Private Sub cmdCellU_Click()
      MSComm1.Output = ''CELL+'' & vbCr
End Sub

Private Sub cmdClear_Click()
      txtData.Text = ''''
      Buffer = ''''
End Sub

Private Sub cmdSaveAs_Click()
      FileBuffer = txtData.Text
      NewFileBuffer = Replace(FileBuffer, '''',
         vbTab, 1, -1, vbBinaryCompare)
      NewFileBuffer = Replace(NewFileBuffer, vbCr,
         vbCrLf, 1, -1, vbBinaryCompare)
      NewFileBuffer = Replace(NewFileBuffer, ''OK'',
         '''', 1, -1, vbTextCompare)
      Out = CVar(NewFileBuffer)
   CommonDialog1.FileName = ''''
   CommonDialog1.Filter = ''Excel (*.xls)|*.xls''
   CommonDialog1.FilterIndex = 2
```

```
    CommonDialog1.ShowSave
    If CommonDialog1.FileName = '''' Then Exit Sub
    On Error GoTo FileError
    Open CommonDialog1.FileName For Output As #1
    On Error GoTo 0
    Print #1, Out
    Close #1
    Exit Sub
FileError:
    Call MsgBox(Error(Err.Number), 48, ''File Not Found!'')
End Sub

Private Sub cmdScan_Click()
      cmdBScan.Enabled = False
      cmdSaveAs.Enabled = False
      cmdClear.Enabled = False
      cmdCellU.Enabled = False
      cmdCellD.Enabled = False
      cmdSend.Enabled = False
      cmdQuit.Enabled = False
      cmdScan.Enabled = False
      If txtRes.Text = '''' Then
            Res = 1
      Else
            Res = CInt(txtRes.Text)
      End If
      If txtBWL.Text = '''' Then
           BWL = 200
      Else
            BWL = CInt(txtBWL.Text)
      End If
      If txtEWL.Text = '''' Then
            EWL = 1100
      Else
            EWL = CInt(txtEWL.Text)
      End If
      If (Res <> 1) And (Res <> 2) And (Res <> 3)
         And (Res <> 4) And (Res <> 5) And (Res <> 6) Then
              MsgBox ''Resolution must be 1, 2, 3, 4, 5, or 6''
         cmdBScan.Enabled = True
         cmdSaveAs.Enabled = True
         cmdClear.Enabled = True
         cmdCellU.Enabled = True
         cmdCellD.Enabled = True
         cmdSend.Enabled = True
```

```
            cmdQuit.Enabled = True
            cmdScan.Enabled = True
            Exit Sub
        End If
        If (BWL < 200) Or (BWL > 1099) Then
            MsgBox ''Beginning Wavelength must be
                at least 200 nm or at most 1099 nm''
            cmdBScan.Enabled = True
            cmdSaveAs.Enabled = True
            cmdClear.Enabled = True
            cmdCellU.Enabled = True
            cmdCellD.Enabled = True
            cmdSend.Enabled = True
            cmdQuit.Enabled = True
            cmdScan.Enabled = True
            Exit Sub
        End If
        If (EWL < 201) Or (EWL > 1100) Then
            MsgBox ''End Wavelength must be
                at least 201 nm or at most 1100 nm''
            cmdBScan.Enabled = True
            cmdSaveAs.Enabled = True
            cmdClear.Enabled = True
            cmdCellU.Enabled = True
            cmdCellD.Enabled = True
            cmdSend.Enabled = True
            cmdQuit.Enabled = True
            cmdScan.Enabled = True
            Exit Sub
        End If
        txtResOK = CStr(Res)
        txtBWLOK = CStr(BWL)
        txtEWLOK = CStr(EWL)
        lblDisplay.Caption = ''''
        lblDisplay.Caption = ''SCANNING SPECTRUM. PLEASE WAIT.''
        MSComm1.Output = ''SCAN '' & txtResOK & ''''
            & txtBWLOK & '''' & txtEWLOK & vbCr
End Sub

Private Sub cmdSend_Click()
    MSComm1.Output = txtSend.Text & vbCr
End Sub

Private Sub cmdQuit_Click()
    If MSComm1.PortOpen = True Then MSComm1.PortOpen = False
```

```
    End If
End Sub

Private Sub Form_Load()
    Buffer = ''
    If MSComm1.PortOpen = True Then
        MsgBox ''Port is already open''
        Exit Sub
    Else
        With MSComm1
            .CommPort = 1
            .Handshaking = comRTS
            .RThreshold = 1
            .InputLen = 0
            .Settings = ''9600,N,8,1''
            .PortOpen = True
        End With
    End If
End Sub

Private Sub Form_Unload(Cancel As Integer)
    If MSComm1.PortOpen = True Then
        MSComm1.PortOpen = False
        End
    Else
        End
    End If
End Sub

Private Sub MSComm1_OnComm()
    'errors
    Select Case MSComm1.CommEvent
        Case comEventBreak
            MsgBox ''comEventBreak''
        Case comEventCDTO
            MsgBox ''comEventCDTO''
        Case comEventCTSTO
            MsgBox ''comEventCTSTO''
        Case comEventDSRTO
            MsgBox ''comEventDSRTO''
        Case comEventFrame
            MsgBox ''comEventFrame''
        Case comEventOverrun
            MsgBox ''comEventOverrun''
        Case comEventRxOver
```

```
            MsgBox ''comEventRxOver''
        Case comEventRxParity
            MsgBox ''comEventRxParity''
        Case comEventTxFull
            MsgBox ''comEventTxFull''
        Case comEventDCB
            MsgBox ''comEventDCB''
    'events
        Case comEvCD
        Case comEvCTS
        Case comEvDSR
        Case comEvRing
        Case comEvReceive
                Buffer = Buffer & MSComm1.Input
                Message = Right(Buffer, 3)
                If InStr(Message, ''OK'') = 1 Then
                    Call DoneCollecting
                Else
                    Call ReadInput
                End If
        Case comEvSend
        Case comEvEOF
    End Select
End Sub

Private Sub DoneCollecting()
    cmdBScan.Enabled = True
    cmdSaveAs.Enabled = True
    cmdClear.Enabled = True
    cmdCellU.Enabled = True
    cmdCellD.Enabled = True
    cmdSend.Enabled = True
    cmdQuit.Enabled = True
    cmdScan.Enabled = True
    lblDisplay.Caption = ''
    lblDisplay.Caption = ''DONE.''
End Sub

Private Sub ReadInput()
    txtData.Text = Buffer
End Sub
```

Bibliography

[1] A. Ashkin, "Acceleration and Trapping of Particles by Radiation Pressure," Phys. Rev. Lett. **24**, 156 (1970).

[2] A. Ashkin, J. M. Dziedzic, J. E. Bjorkholm, and S. Chu, "Observation of a single-beam gradient force optical trap for dielectric particles," Opt. Lett. **11**, 288 (1986).

[3] A. Ashkin and J. M. Dziedzic, "Optical Levitation by Radiation Pressure," Appl. Phys. Lett. **19**, 283 (1971).

[4] Karel Svoboda and Steven M. Block, "Optical trapping of metallic Rayleigh particles," Opt. Lett. **19**, 930 (1994).

[5] C. Bustamante, J. C. Macosko, and G. H. L Wuite, "Grabbing the Cat by the Tail: Manipulating Molecules One by One," Nat. Rev. Mol. Cell Biol. **1**, 130 (2000).

[6] F. C. MacKintosh and C. F. Schmidt, "Microrheology," Curr. Opin. Colloid Interface Sci. **4**, 300 (1999).

[7] P. L. Biancaniello and J. C. Crocker, "Line optical tweezers instrument for measuring nanoscale interactions and kinetics," Rev. Sci. Instr. **77**, 113702 (2006).

[8] K. Visscher, S. P. Gross, and S. M. Block, "Construction of multiple-beam optical traps with nanometer-resolution position sensing," IEEE J. Sel. Top. in Quant. Elec. **2**, 1066 (1996).

[9] A. B. Stilgoe, T. A. Niemenen, G. Knöner, N. R. Heckenberg, and H. Rubinsztein-Dunlop, "The effect of Mie resonances on trapping in optical tweezers," Opt. Expr. **16**, 15039 (2008).

[10] R. R. Agayan, F. Gittes, R. Kopelman, and C. F. Schmidt, "Optical trapping near resonance absorption," Appl. Opt. **41**, 2318 (2002).

[11] A. B. Stilgoe, T. A. Nieminen, G. Knöner, N. R. Heckenberg, and H. Rubinsztein-Dunlop, "The effect of Mie resonances on trapping in optical tweezers," Opt. Expr. **16**, 10539 (2008).

[12] A. Ashkin, "Forces of a single-beam gradient laser trap on a dielectric sphere in the ray optics regime," Biophys. J. **61**, 569 (1992).

[13] A. Ashkin and J. M. Dziedzic, "Observation of optical resonances of dielectric spheres by light scattering," Appl. Opt. **20**, 1803 (1981).

[14] M. J. Kendrick, D. H. McIntyre, and O. Ostroverkhova, "Wavelength dependence of optical tweezer trapping forces on dye-doped polystyrene microspheres," J. Opt. Soc. Am. B. **26**, 2189 (2009).

[15] L. Mitchem and J. P. Reid, "Optical manipulation and characterisation of aerosol particles using a single-beam gradient force optical trap," Chem. Soc. Rev. **37**, 756 (2008).

[16] R. Kubo, M. Toda, and N. Hashitsume, *Statistical Physics* (Springer, Heidelberg, 1985), Vol. 2.

[17] Kirstine Berg-Sørenson and Henrik Flyvbjerg, "Power spectrum analysis for optical tweezers," Rev. Sci. Instr. **75**, 594 (2004).

[18] Todd M. Squires and Stephen R. Quake, "Microfluidics: Fluid physics at the nanoliter scale," Rev. Mod. Phys. **77**, 977 (2005).

[19] Michael P. Norton and Denis G. Karczub, *Fundamentals of Noise and Vibration Analysis for Engineers* (Cambridge University Press, Cambridge, 2003).

[20] Alexandr Jonáš and Pavel Zemánek, "Light at work: The use of optical forces for particle manipulation, sorting, and analysis," Electrophoresis **29**, 4813 (2008).

[21] Craig G. Bohren and Donald R. Huffman, *Absorption and Scattering of Light by Small Particles* (Wiley-VCH, Weinheim, 2007).

[22] P. C. Chaumet and M. Nieto-Vesperinas, "Time-averaged total force on a dipolar sphere in an electromagnetic field," Opt. Lett. **25**, 1065 (2000).

[23] A. Ashkin and J. P. Gordon, "Stability of radiation-pressure particle traps: an optical Earnshaw theorem," Opt. Lett. **8**, 511 (1983).

[24] A. Yariv, *Quantum Electronics* (John Wiley and Sons, Inc., New York, 1967).

[25] J. D. Jackson, *Classical Electrodynamics* (John Wiley and Sons, Inc., New York, 1962).

[26] C. Cohen-Tannoudji, J. Dupont-Roc, G. Grynberg, *Atom-Photon Interactions* (Wiley-VCH, Germany, 1998).

[27] K. Neuman and S. Block, "Optical Trapping," Rev. Sci. Instr. **75**, 2787 (2004).

[28] J. D. Ingle and S. R. Crouch, *Spectrochemical Analysis*, (Prentice Hall, 1988).

[29] J. R. Arias-Gonzálex and M. Nieto-Vesperinas, "Optical forces on small particles: attractive and repulsive nature and plasmon-resonance conditions," J. Opt. Soc. Am. A **20**, 1201 (2003).

[30] Yeonee Seol, Amanda E. Carpenter, and Thomas T. Perkins, "Gold nanoparticles: enhanced optical trapping and sensitivity coupled with significant heating," Opt. Lett. **31**, 2429 (2006).

[31] A. J. Devaney and E. Wolf, "Multipole expansions and plane-wave representations of electromagnetic-field," J. Math. Phys. **15**, 234 (1974).

[32] J. Barton, D. Alexander, and S. Schaub, "Theoretical determination of net radiation force and torque for a spherical particle illuminated by a focused laser beam," J. Appl. Phys. **66**, 4594 (1989).

[33] O. Farsund and B. Felderhof, "Force, torque, and absorbed energy for a body of arbitrary shape and constitution in an electromagnetic radiation field," Physica A **227**, 108 (1996).

[34] J. Barton and D. Alexander, "Fifth-order corrected electromagnetic field components for a fundamental Gaussian beam," J. Appl. Phys. **66**, 2800 (1989).

[35] J. Lock, "Calculation of the radiation trapping force for laser tweezers by use of generalized Lorenz-Mie theory. II. On-axis trapping force," Appl. Opt. **43**, 2545 (2004).

[36] J. Lock, "Calculation of the radiation trapping force for laser tweezers by use of generalized Lorenz-Mie theory. I. Localized model description of an on-axis tightly focused laser beam with spherical aberration," Appl. Opt. **43**, 2532 (2004).

[37] A. Mazolli, P. Neto, and H. Nussenzveig, "Theory of trapping forces in optical tweezers," Proc. R. Soc. London, Ser. A **459**, 3021 (2003).

[38] K. Ren, G. Grehan, and G. Gouesbet, "Prediction of reverse radiation pressure by generalized Lorena-Mie theory," Appl. Opt. **35**, 2702 (1996).

[39] T. A. Niemenen, H. Rubinsztein-Dunlop, and N. R. Heckenberg, "Multipole expansion of strongly focussed laser beams," J. Quant. Spec. Rad. Trans. **79-80**, 1005 (2003).

[40] P. C. Waterman, "Symmetry, Unitarity, and Geometry in Electromagnetic Scattering," Phys. Rev. D. **3**, 825 (1971).

[41] M. I. Mishchenko, "Light scattering by randomly oriented axially symmetric particles," J. Opt. Soc. Am. A **8**, 871 (1991).

[42] T. A. Niemenen, H. Rubinsztein-Dunlop, and N. R. Heckenberg, "Calculation of the T-matrix: general considerations and application of the point-matching method," J. Quant. Spec. Rad. Trans. **79-80**, 1019 (2003).

[43] T. A. Niemenen, V. L. Y. Loke, A. B. Stilgoe, G. Knöner, A. M. Brańczyk, N. R. Heckenberg, and H. Rubinsztein-Dunlop, "Optical tweezers computational toolbox," J. Opt. A **9**, S196 (2007).

[44] A. Ashkin and J. M. Dziedzic, "Observations of Resonances in the Radiation Pressure on Dielectric Spheres," Phys. Rev. Lett. **38**, 1351 (1977).

[45] A.E. Neeves and M.H.Birnboim, "Composite structures for the enhancement of nonlinear-optical susceptibility," J. Opt. Soc. Am. B **6**, 787 (1989).

[46] S.J. Oldenburg, R.D. Averitt, S.L. Westcott, and N.J. Halas, "Nanoengineering of optical resonances," Chem. Phys. Lett. **288**, 288 (1998).

[47] D. Patrick O'Neal, Leon R. Hirsch, Naomi J. Halas, J. Donald Payne, and Jennifer L. West, "Photo-thermal tumor ablation in mice using near infrared-absorbing nanoparticles", Canc. Lett. **209**, 171 (2004).

[48] Christopher Loo, Alex Lin, Leon Hirsch, Min-Ho Lee, Jennifer Barton, Naomi Halas, Jennifer West, and Rebekah Drezek, "Nanoshell-Enabled Photonics-Based Imaging and Therapy of Cancer," Tech. in Canc. Res. and Treat. **3**, 33 (2004).

[49] M. Perner, P. Bost, U. Lemmer, G. von Plessen, and J. Feldman, "Optically Induced Damping of the Surface Plasmon Resonance in Gold Colloids," Phys. Rev. Lett. **78**, 2192 (1997).

[50] J.-Y. Bigot, J.-C. Merle, O. Cregut, and A. Daunois, "Electron Dynamics in Copper Metallic Nanoparticles Probed with Femtosecond Optical Pulses," Phys. Rev. Lett. **75**, 4702 (1995).

[51] U. Kreibig, M. Vollmer, U. Gonser, M. B. Panish, R. M. Osgood Jr., H. Sakaki, and H. K. V. Lotsch, *Optical Properties of Metal Clusters*, (Springer Verlag, Berlin, 1995).

[52] Arthur L. Aden and Milton Kerker, "Scattering of Electromagnetic Waves from Two Concentric Spheres," J. Appl. Phys. **22**, 1242 (1951).

[53] Naomi J. Halas, "The optical properties of nanoshells," Optics and Photonics News **13**, 26 (2002).

[54] W. Stöber, A. Fink, and E. Bohn, "Controlled growth of monodisperse silica spheres in the micron size range," **26**, 62 (1968).

[55] Colleen L. Nehlm, Nathaniel K. Grady, Glenn P. Goodrich, Felicia Tam, Naomi J. Halas, and Jason H. Hafner, "Scattering Spectra of Single Gold Nanoshells," Nano Lett. **4**, 2355 (2004).

[56] Anatoly V. Zayats, Igor I. Smolyaninov, and Alexei A. Maradudin, "Nano-optics of surface plasmon polaritons," **408**, 131 (2005).

[57] W. L. Barnes, A. Dereux, and T. W. Ebbesen, "Surface plasmon subwavelength optics," Nature **424**, 824 (2003).

[58] S. A. Maier, *Plasmonics: Fundamentals and Applications*, (Springer Science and Business Media L.L.C, New York, 2007).

[59] N. Grady, *Influence of dielectric function properties on the optical response of plasmon resonant metallic nanoparticles*, (Masters Thesis, Rice University, Houston, 2004).

[60] E. Prodan and P. Nordlander, "Plasmon hybridization in spherical nanoparticles," J. Chem. Phys. **120**, 5444 (2004).

[61] E. Prodan, C. Radloff, N .J. Halas, and P. Nordlander,"A Hybridization Model for the Plasmon Response of Complex Nanostructures," Science **302**, 419 (2003).

[62] Bruce E. Brinson, J. Britt Lassiter, Carly S. Levin, Rizia Bardhan, Nikolay Mirin, and Naomi J. Halas, "Nanoshells Made Easy: Improving Au Layer Growth on Nanoparticle Surfaces," Langmuir **24**, 14166 (2008).

[63] P. B. Johnson and R. W. Christy, "Optical constants of the noble metals," Phys. Rev. B **6**, 4370 (1972).

[64] Warren J. Smith, *Modern Optical Engineering*, (McGraw-Hill Inc., Boston, 1990).

[65] H. C. van de Hulst, *Light Scattering by Small Particles*, (Dover Publications, Mineola, 1981).

[66] Petr Chýlek and Jiyu Zhan, "Interference structure of the Mie extinction cross section," J. Opt. Soc. Am. A **6**, 1846 (1989).

[67] Julie Lutti, Wolfgang Langbein, and Paola Borri, "High Q optical resonances of polystyrene microspheres in water controlled optical tweezers," Appl. Phys. Lett. **91**, 91 (2007).

[68] A. Pralle, M. Prummer, E. -L. Florin, E. H. K. Stelzer, and J. K. H. Hörber, "Three-Dimensional High-Resolution Particle Tracking for Optical Tweezers by Forward Scattered Light", Microsc. Res. Tech. **44**, 378 (1999).

[69] S. N. S. Reihani and L. B. Oddershede, "Optimizing immersion media refractive index improves optical trapping by compensating spherical aberrations," Opt. Lett. **32**, 1998 (2007).

[70] The One Molecule Group, University of Wisconsin, Madison. http://onemolecule.chem.uwm.edu/index.php/software/13-public-software/43-psf-lab

[71] L. Bosanac, T. Aabo, P. M. Bendix, and L. B. Oddershede, "Efficient Optical Trapping and Visualization of Silver Nanoparticles," Nano Lett. **8**, 1486 (2008).

[72] F. Hajizadeh and S. N. S. Reihani, "Optimized optical trapping of gold nanoparticles," Opt. Expr. **18**, 551 (2010).

[73] M. Li and J. Arlt, "Trapping multiple particles in single optical tweezers," Opt. Comm. **281**, 135 (2008).

[74] P. M. Celliers and J. Conia, "Measurement of localized heating in the focus of an optical trap," Appl. Opt. **39**, 3396 (2000).

[75] H. Mao, J. R. Arias-Gonzales, S. B. Smith, I. Tinoco Jr., and C. Bustamante, "Temperature control methods in a laser tweezers system," Biophys. J. **89**, 1308 (2005).

[76] Poul M. Bendix, S. Nader Reihani, and Lene B. Oddershede, "Direct Measurements of Heating by Electromagnetically Trapped Nanoparticles on Supported Lipid Bilayers", ACS Nano **4**, 2256 (2010).

[77] E. J. G. Peterman, F. Gittes, and C. F. Schmidt, "Laser-Induced Heating in Optical Traps," Biophys. J. **84**, 1308 (2003).

[78] E. A. Abbondanzieri, J. W. Shaevitz, and S. M. Block, "Picocalorimetry of transcription by RNA polymerase," Biophys. J. **89**, L61 (2005).

[79] H. Rubinsztein-Dunlop, T. A. Niemenen, M. E. J. Friese, and N. R. Heckenberg, "Optical trapping of absorbing particles," Adv. Quant. Chem. **30**, 469 (1998).

[80] Nadine Harris, Michael J. Ford, and Michael B. Cortie, "Optimization of Plasmonic Heating by Gold Nanospheres and Nanoshells", J. Phys. Chem. B **110**, 10701 (2006).

[81] M. Laliberté, "Model for calculating the viscosity of aqueous solutions," J. Chem. Eng. Data **52**, 321 (2007).

[82] The Biomedical Optics Research Laboratory, University College, London $http://medphys.ucl.ac.uk/research/borl/research/NIR_topics/spectra/spectra.htm$

[83] G. Pesce, A. Sasso, and S. Fusco, "Viscosity measurements on micron-size scale using optical tweezers," Rev. Sci. Instr. **76**, 115105 (2005).

[84] Alexander Rohrbach, "Stiffness of Optical Traps: Quantitative Agreement between Experiment and Electromagnetic Theory", Phys. Rev. Lett. **95**, 168102-1 (2005).

[85] R. Quidant, A. S. Zelenina, and M. Nieto-Vesperinas, "Optical manipulation of plasmonic nanoparticles", Appl. Phys. A: Mater. Sci. Process. **89**, 233 (2007).

[86] J. Prikulis, F. Svedberg, M. Käll, J. Enger, K. Ramser, M. Goksör, and D. Hanstorp, "Optical Spectroscopy of Single Trapped Metal Nanoparticles in Solution," Nano Lett. **4**, 115 (2004).

[87] P. Li, K. Shi, and Z. Liu, "Manipulation and spectroscopy of a single particle by use of white-light optical tweezers," Opt. Lett. **30**, 156 (2005).